# TR-612: Wind Loads on Dynamic Message Cabinets and Behavior of Supporting Trusses

## Final Report
## May 2013

Submitted by

**George Constantinescu and M. Asghar Bhatti**
Department of Civil & Environmental Engineering
and
IIHR-Hydroscience and Engineering Hydraulics Laboratory
The University of Iowa
Iowa City, IA

**Terry Wipf and Brent Phares**
Department of Civil, Construction, and Environmental Engineering
and
The Bridge Engineering Center at the Institute for Transportation.
Iowa State University
Ames, IA

**Authors:**
Univ. Iowa: G. Constantinescu, M. A. Bhatti, Z. Cheng, T. Tokyay, N. Nissen
Iowa State Univ.: T. Wipf, B. Phares, B. Chang, H. Zou

**Sponsored by**
The Iowa Highway Research Board
Iowa Department of Transportation
and
The Federal Highway Administration

**Disclaimer Notice**

The contents of this report reflect the views of the authors, who are responsible for the facts and the accuracy of the information presented herein. The opinions, findings, and conclusions expressed in this publication are those of the authors and not necessarily of the sponsors. The sponsors assume no liability for the contents or use of the information contained in this document. This report does not constitute a standard, specification, or regulation.

The sponsors do not endorse products or manufacturers. Trademarks or manufacturer's names appear in this report only because they are considered essential to the objectives of the document.

**Statement of Non-Discrimination**

Federal and state laws prohibit employment and/or public accommodation discrimination on the basis of age, color, creed, disability, gender identity, national origin, pregnancy, race, religion sex, sexual orientation or veteran's status. If you believe you have been discriminated against, please contact the Iowa Civil Rights Commission at 800-457-4416 or Iowa Department of Transportation's affirmative action officer. If you need accommodations because of a disability to access the Iowa Department of Transportation's services, contact the agency's affirmative action officer at 800-262-0003.

The University of Iowa does not discriminate on the basis of race, color, age, religion, national origin, sexual orientation, gender identity, sex, marital status, disability, or status as a U.S. veteran. Inquiries can be directed to the Director of Equal Opportunity and Diversity at the University of Iowa, (319) 335-0705.

**Acknowledgements**

The authors would like to thank the Iowa Highway Research Board and the Federal Highway Administration for supporting this study. The authors would also like to thank all the members of the Technical Advisory Committee for their advice and guidance and Mr. Mark Dunn for overseeing this project.

| | | |
|---|---|---|
| **1. Report No.**<br>**TR-612** | **2. Government Accession No.**<br>Optional | **3. Recipient Catalog No.**<br>Optional |
| **4 Title and Subtitle**<br>Wind loads on dynamic message cabinets and behavior of supporting trusses | | **5 Report Date**<br>August 31, 2013 |
| | | **6 Performing Organization Code**<br>N/A |
| 7. **Author(s)** Constantinescu G., Bhatti, A., Phares, B. and Wipf, T. | | 8 Performing Organization Report No. |
| **9 Performing Organization Name and Address**<br>Dept. Civil and Environmental Engineering, The University of Iowa, Iowa City, IA, 52242 and Dept. Civil, Construction and Environmental Engineering and The Bridge Engineering Center at the Institute for Transportation, Iowa State University, Ames, Iowa. | | **10 Work Unit No. (TRAIS)**<br>Not Required |
| | | **11 Contract or Grant No.**<br>SPR Part II Funds |
| **12 Sponsoring Organization Name and Address**<br>Iowa Department of Transportation<br>800 Lincoln Way<br>Ames, Iowa 50010<br><br>Federal Highway Administration | | **13 Type of Report and Period Covered**<br>Final Report |
| | | **14 Sponsoring Agency Code**<br>**TR-612** |
| **15 Supplementary Notes**<br>None | | |

**16 Abstract**

Large Dynamic Message Signs (DMSs) have been increasingly used on freeways, expressways and major arterials to better manage the traffic flow by providing accurate and timely information to drivers. Overhead truss structures are typically employed to support those DMSs allowing them to provide wider display to more lanes. In recent years, there is increasing evidence that the truss structures supporting these large and heavy signs are subjected to much more complex loadings than are typically accounted for in the codified design procedures. Consequently, some of these structures have required frequent inspections, retrofitting, and even premature replacement. Two manufacturing processes are primarily utilized on truss structures - welding and bolting. Recently, cracks at welding toes were reported for the structures employed in some states.

Extremely large loads (e.g., due to high winds) could cause brittle fractures, and cyclic vibration (e.g., due to diurnal variation in temperature or due to oscillations in the wind force induced by vortex shedding behind the DMS) may lead to fatigue damage, as these are two major failures for the metallic material. Wind and strain resulting from temperature changes are the main loads that affect the structures during their lifetime. The American Association of State Highway and Transportation Officials (AASHTO) Specification defines the limit loads in dead load, wind load, ice load, and fatigue design for natural wind gust and truck-induced gust.

The objectives of this study are to investigate wind and thermal effects in the bridge type overhead DMS truss structures and improve the current design specifications (e.g., for thermal design). In order to accomplish the objective, it is necessary to study structural behavior and detailed strain-stress of the truss structures caused by wind load on the DMS cabinet and thermal load on the truss supporting the DMS cabinet.

The study is divided into two parts. The Computational Fluid Dynamics (CFD) component and part of the structural analysis component of the study were conducted at the University of Iowa while the field study and related structural analysis computations were conducted at the Iowa State University. The CFD simulations were used to determine the air-induced forces (wind loads) on the DMS cabinets and the finite element analysis was used to determine the response of the supporting trusses to these pressure forces. The field observation portion consisted of short-term monitoring of several DMS Cabinet/Trusses and long-term monitoring of one DMS Cabinet/Truss. The short-term monitoring was a single (or two) day event in which several message sign panel/trusses were tested. The long-term monitoring field study extended over several months. Analysis of the data focused on trying to identify important behaviors under both ambient and truck induced winds and the effect of daily temperature changes.

Results of the CFD investigation, field experiments and structural analysis of the wind induced forces on the DMS cabinets and their effect on the supporting trusses showed that the passage of trucks cannot be responsible for the problems observed to develop at trusses supporting DMS cabinets. Rather the data pointed toward the important effect of the thermal load induced by cyclic (diurnal) variations of the temperature. Thermal influence is not discussed in the specification, either in limit load or fatigue design. Although the frequency of the thermal load is low, results showed that when temperature range is large the restress range would be significant to the structure, especially near welding areas where stress concentrations may occur. Moreover stress amplitude and range are the primary parameters for brittle fracture and fatigue life estimation. Long-term field monitoring of one of the overhead truss structures in Iowa was used as the research baseline to estimate the effects of diurnal temperature changes to fatigue damage. The evaluation of the collected data is an important approach for understanding the structural behavior and for the advancement of future code provisions. Finite element modeling was developed to estimate the strain and stress magnitudes, which were compared with the field monitoring data. Fatigue life of the truss structures was also estimated based on AASHTO specifications and the numerical modeling. The main conclusion of the study is that thermal induced fatigue damage of the truss structures supporting DMS cabinets is likely a significant contributing cause for the cracks observed to develop at such structures. Other probable causes for fatigue damage not investigated in this study are the cyclic oscillations of the total wind load associated with the vortex shedding behind the DMS cabinet at high wind conditions and fabrication tolerances and induced stresses due to fitting of tube to tube connections

| | | | |
|---|---|---|---|
| **17 Key Words**<br>Dynamic message cabinets, wind loads, temperature effects, traffic signs, supporting trusses | | **18 Distribution Statement**<br>No restrictions. This document is available to the public through the National Technical Information Service, Springfield, Virginia 22161 | |
| **19 Security Classification (of this report)**<br>Unclassified | **20 Security Classification (of this page)**<br>Unclassified | **21 No. of pages**<br>108 | **22 Price**<br>N/A |

**Form DOT F 1700.7 (8-72)**

This page left intentionally blank

This page left intentionally blank

TABLE OF CONTENTS

## Executive Summary

Large Dynamic Message Signs (DMSs) have been increasingly used on freeways, expressways and major arterials to better manage the traffic flow by providing accurate and timely information to drivers. Overhead truss structures are typically employed to support those DMSs allowing them to provide wider display to more lanes. In recent years, there is increasing evidence that the truss structures supporting these large and heavy signs are subjected to much more complex loadings than are typically accounted for in the codified design procedures. Consequently, some of these structures have required frequent inspections, retrofitting, and even premature replacement. Two manufacturing processes are primarily utilized on truss structures - welding and bolting. Recently, cracks at welding toes were reported for the structures employed in some states.

Extremely large loads (e.g., due to high winds) could cause brittle fractures, and cyclic vibration (e.g., due to diurnal variation in temperature or due to oscillations in the wind force induced by vortex shedding behind the DMS) may lead to fatigue damage, as these are two major failures for the metallic material. Wind and strain resulting from temperature changes are the main loads that affect the structures during their lifetime. The American Association of State Highway and Transportation Officials (AASHTO) Specification defines the limit loads in dead load, wind load, ice load, and fatigue design for natural wind gust and truck-induced gust.

The objectives of this study are to investigate wind and thermal effects in the bridge type overhead DMS truss structures and improve the current design specifications (e.g., for thermal design). In order to accomplish the objective, it is necessary to study structural behavior and detailed strain-stress of the truss structures caused by wind load on the DMS cabinet and thermal load on the truss supporting the DMS cabinet.

The study is divided into two parts. The Computational Fluid Dynamics (CFD) component and part of the structural analysis component of the study were conducted at the University of Iowa while the field study and related structural analysis computations were conducted at the Iowa State University. The CFD simulations were used to determine the air-induced forces (wind loads) on the DMS cabinets and the finite element analysis was used to determine the response of the supporting trusses to these pressure forces. The field observation portion consisted of short-term monitoring of several DMS Cabinet/Trusses and long-term monitoring of one DMS Cabinet/Truss. The short-term monitoring was a single (or two) day event in which several message sign panel/trusses were tested. The long-term monitoring field study extended over several months. Analysis of the data focused on trying to identify important behaviors under both ambient and truck induced winds and the effect of daily temperature changes.

Results of the CFD investigation, field experiments and structural analysis of the wind induced forces on the DMS cabinets and their effect on the supporting trusses showed that the passage of trucks cannot be responsible for the problems observed to develop at trusses supporting DMS cabinets. Rather the data pointed toward the important effect of the thermal load induced by cyclic (diurnal) variations of the temperature. Thermal influence is not discussed in the specification, either in limit load or fatigue design. Although the frequency of the thermal load is

low, results showed that when temperature range is large the stress range would be significant to the structure, especially near welding areas where stress concentrations may occur. Moreover stress amplitude and range are the primary parameters for brittle fracture and fatigue life estimation. Long-term field monitoring of one of the overhead truss structures in Iowa was used as the research baseline to estimate the effects of diurnal temperature changes to fatigue damage. The evaluation of the collected data is an important approach for understanding the structural behavior and for the advancement of future code provisions. Finite element modeling was developed to estimate the strain and stress magnitudes, which were compared with the field monitoring data. Fatigue life of the truss structures was also estimated based on AASHTO specifications and the numerical modeling. The main conclusion of the study is that thermal induced fatigue damage of the truss structures supporting DMS cabinets is likely a significant contributing cause for the cracks observed to develop at such structures. Other probable causes for fatigue damage not investigated in this study are the cyclic oscillations of the total wind load associated with the vortex shedding behind the DMS cabinet at high wind conditions and fabrication tolerances and induced stresses due to fitting of tube to tube connections.

# 1. Introduction

## 1.1. Problem statement

The safety of the facilities used on highways is very important, both for drivers and traffic. Large Dynamic Message Signs (DMSs) have been increasingly used on freeways, expressways and major arterials to better manage traffic flow by providing accurate and timely information to drivers. Having a detailed understanding of the wind forces on large highway signs is crucial for the safe and economical design of the supporting truss structures. In recent years, there is increasing evidence that the truss structures supporting these large and heavy signs are subjected to much more complex loadings than are typically accounted for in the codified design procedures. Consequently, some of these structures have required frequent inspections, retrofitting, and even premature replacement.

Overhead structures are typically employed to support those DMS cabinets so that they can provide a wider display. In order to secure these heavy and large cabinets, structures are designed using four chord trusses, which are also susceptible to complicated loads. Extreme weather conditions such as strong gusts or large temperature ranges may generate unexpected high stress on the structures, especially where stress concentration occurs due to geometric discontinuities. Cyclic loading like truck-induced gusts could also lead to fatigue failure for metallic materials. Previous research (Stam et al., 2011) found that typical welded connections did not meet the requirements of the fatigue design specifications. Therefore, frequent inspections of those structures are required for the purpose of safety and reliability. Thus, to reliably predict the behavior of these structures, and to design them properly, detailed knowledge of the forces on and behavior of these structures is obviously necessary.

The current design practice for overhead truss structures is in accordance with the American Association of State Highway and Transportation Officials (AASHTO) Standard Specifications for Structural Supports for Highway Signs, Luminaires and Traffic Signals (AASHTO, 2010). The specifications include updated provisions and criteria for extreme wind loads and new provisions and criteria on fatigue design. In particular, the AASHTO specification addresses the effects of wind load, dead load, live load, ice load, and fatigue design for natural wind gust and truck-induced gust. An important observation is that thermal influence is not considered in the specification.

Large DMS cabinets, designed using the standard provisions may have an adequate factor of safety against strength failure but their response to aeroelastic phenomena and thermal oscillations is largely unknown. For example, flutter may cause torsional vibrations that usually receive little consideration in design. Buffeting may cause large structural motions and over time can induce fatigue damage. Diurnal variations in the temperature can induce large stresses in the truss members supporting the DMS cabinet and cause fatigue failure. An additional phenomenon that is often overlooked during design is the effect of unsteady oscillations on the cabinets and on their support trusses. These oscillations develop even under steady wind conditions due to the unsteady vortex shedding which takes place in the air wake of the flow past the cabinets. A resonance condition, causing large amplitude relatively steady vibrations of the

support trusses can occur if the frequency of shedding coincides with a natural vibration frequency of the DMS cabinet. Vortex-shedding can occur at relatively low wind speeds and thus, even if the structure has enough strength, such large oscillations may contribute to premature fatigue failure.

Most of the current guidelines for wind design of highway structures are based on wind tunnel studies with some limited field investigation. The wind tunnel studies provide valuable insight but, besides being expensive, they have obvious limitations because of the differences between the laboratory and field conditions. In the past there was essentially no other alternative. However recent advances in the computational fluid dynamics (CFD) have made tools available that allow realistic fully three-dimensional simulations of actual field conditions at a fraction of the cost of wind tunnel studies.

The main objectives of this study are to investigate the wind and thermal effects on truss structures supporting DMS cabinets and to gain a better understanding of the behavior causing cracking to occur. The effect of additional loads on DMS cabinets due to frequent passage of trucks underneath the DMS cabinet was also studied in the present study. To accomplish these objectives, it was necessary to study the structural behavior and response of the truss structures caused by wind and thermal loads. The wind loads were either measured from the field study or obtained from CFD simulations. Finite element modeling was conducted to estimate the stress and strain magnitudes, which were then compared with the field monitoring data. Fatigue life of the study structure was also estimated based on AASHTO specifications and the finite element modeling.

### 1.2. Background

Typical overhead truss structures in Iowa have been made of aluminum alloy with fillet-welded tube-to-tube connections. Aluminum, favored for its light weight and corrosive resistance, however, has much lower fatigue resistance than structural steel. Welding heat reduces the strength of the material based on factors such as welding speed and cooling rate. Moreover, welding of typical aluminum alloy used at overhead truss structures in Iowa removes heat treatment near the welds and thus reduces aluminum properties locally. Geometric discontinuities at tube-to-tube connections also generate significant stress concentrations. The welded connections therefore have high risks of cracks. According to the Action Plan of DMS Trusses from Iowa DOT (Brakke, 2007), 36 trusses were erected from 1993 to 2006 and in 2007 cracks were found in 14 of 19 (74%) inspected DMS trusses. Figure 1 shows typical crack locations on a truss structure. It was found that most cracks occurred at the diagonal members while a few of them occurred on vertical members.

In addition, an evaluation conducted by Purdue University (Bowen Laboratory, 2011) for one of cracked truss structures indicated that the cracks seemed to be brittle fractures caused by extreme loads. A detailed examination of the cracks is shown in Fig. 2. Figure 2a shows that failure occurred at the welding material, which then progressed through the entire weld throat. The diagonal and chord members were also found not to be completely merged. The crack in Fig. 2b occurred near the welding toe and propagated into the base material. In order to predict the behavior of a highway overhead truss structure, detailed understanding of the loads and the

response of the structure are necessary. The influences of temperature variation and wind on the structure will be examined in this study.

Structural supports for overhead signs vary by materials and design specifications. There are three main types of designs: cantilever, bridge, and butterfly (Alberta Infrastructure and Transportation [AIT], 2006). The truss structures discussed in the study are typical bridge-type truss structures, which are designed with a large span to carry heavy signs.

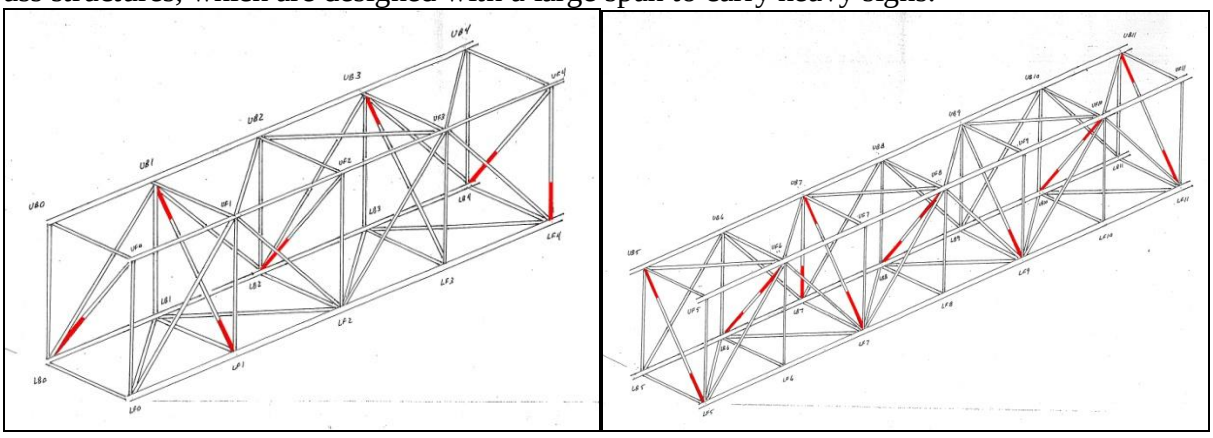

Fig. 1 Crack locations on typical truss structures (Brakke, 2007)

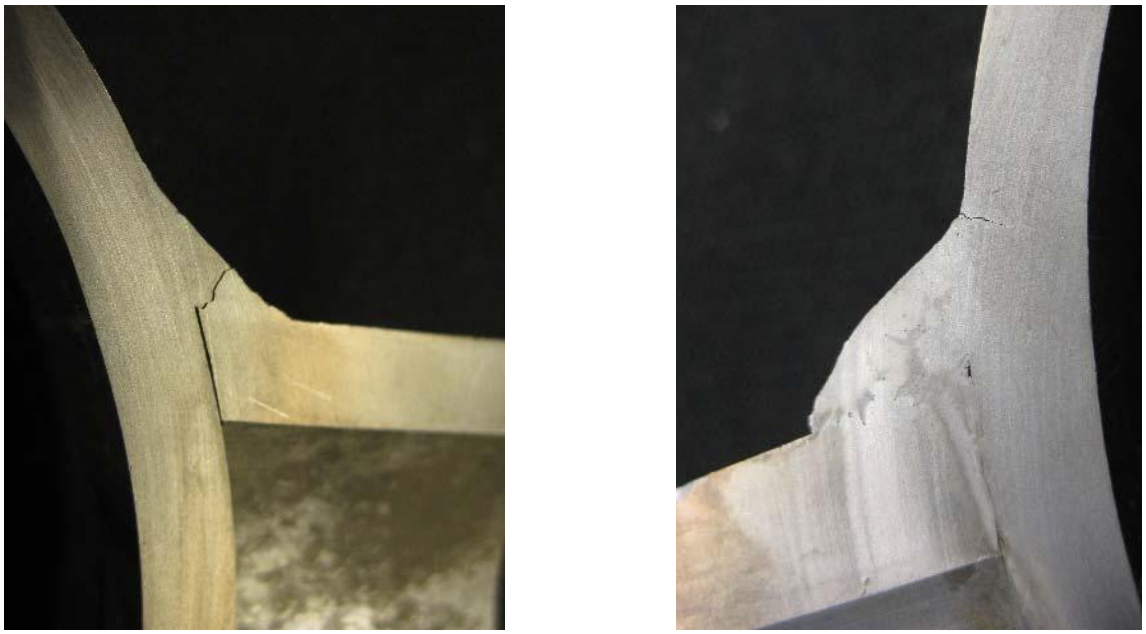

(a). Crack at throat (b). Crack at toe

Fig. 2 Cracks observed through welded throat and toe (Bowen Laboratory, 2011)

Wind or truck-induced gusts produce aeroelastic effects on these structures, especially when the gust direction is perpendicular with the DMS broad surface. In addition, when one of the natural frequencies of the bridge-type truss structure is close to the frequency of gusts or vortex shedding frequency, the structure operates in a near-resonant condition. Thus, the dynamic

excitation can be significant depending on wind speed, mechanical damping, and etc. Large ranges of daily temperatures also cause considerable displacement and thermal stress.

Several National Cooperative Highway Research Program (NCHRP) studies have been focused on fatigue failure of truss structures (Fouad et al, 2003; Dexter & Ricker, 2002), but few truss structures were tested to understand the thermal response. In general the NCHRP research has sought to identify design details that resulted in infinite fatigue design lives.

### 1.3. Main components of the study

The study is divided into two parts. The CFD component and part of the structural analysis component of the study were conducted at the University of Iowa while the field study and related structural analysis computations were conducted at the Iowa State University.

The CFD simulations are used to determine the air-induced forces (wind loads) on the DMS cabinets (Section 3) and the finite element analysis is used to determine the response of the supporting trusses to these pressure forces (Section 4). The numerical simulations model used the same trusses that were selected for the field monitoring study (Sections 5 and 6).

The field observation portion consisted of short-term monitoring of four DMS Cabinet/Trusses (Section 5) and long-term monitoring of one DMS Cabinet/Truss (Section 6). The evaluation methodology used in the short-term and long-term field monitoring of the trusses is discussed at the start of Sections 5 and 6, respectively. Analysis of the data in sections 5 and 6 focused on trying to identify important behaviors under both ambient and truck induced winds and the effect of daily temperature changes. Section 5 details the results of the field monitoring study at the four trusses and explains why loads from wind and wind gusts induced by the passage of the trucks under the DMS cabinet are not significant enough to likely cause failure in the truss members. Section 6 starts with a literature review related to highway overhead truss structures, load effects, and fatigue life estimations. The effects associated with wind induced vibrations, truck induced vibrations and temperature oscillations are discussed based on the measured data. This is followed by a detailed mathematical analysis of the effect of thermal and wind loads on the truss structure. Finite element modeling is described and the results are discussed and compared to field measurements. As part of the analysis, the stress occurring under extreme thermal conditions were estimated. Finally, a fatigue analysis of the truss structure is provided and the fatigue life of the structure is estimated.

Section 7 summarizes the main conclusions and offers suggestions for future work.

## 2. Numerical methodology

### 2.1. Computational Fluid Dynamics simulations

Most predictions of engineering flows are obtained using the so-called Reynolds Averaged Navier-Stokes (RANS) approach in which the effect of most of the scales (eddies, vortices) on the mean flow is accounted via a RANS turbulence model.

RANS based numerical simulations were performed using Fluent, a commercial Computational Fluid Dynamics (CFD) general software for modeling fluid flow and heat transfer in complex geometries. As a preprocessor for geometry modeling and mesh generation, Gambit® was used. Gambit allows the user to generate high quality meshes using unstructured multi-block grids. Fluent can use a wide range of turbulence models with both wall functions and near-wall treatment to simulate turbulent flows.

The parallel pressure based RANS solver was employed to conduct steady-state simulations. The implicit RANS solver employs a cell centered finite volume scheme and can use hybrid unstructured meshes. The continuity equation is satisfied using the SIMPLE pressure-velocity algorithm. Gradients of the solution variables are computed using Green-Gauss' theorem. Diffusion terms are discretized using second order central scheme. For the convective terms, there are several choices offered in the code including first order upwind, second order upwind, QUICK and third order MUSCL schemes. For the convective terms in the momentum equations, the second order upwind scheme was chosen as the discretization scheme in the present simulations. The discretized equations are solved using point wise Gauss-Seidel iteration in conjunction with an algebraic multi-grid method to accelerate the solution convergence.

The shear stress transport (SST) model which can be integrated up to the wall was used as the turbulence model. A full description of the models is given in Fluent User's Guide (2001). The SST version uses the classical k-ω model (k is the turbulence kinetic energy, ω is the specific turbulence dissipation rate) near solid walls and the high Reynolds number version of the k-ε model away from the solid walls and inside the free-shear layers. Major features are the zonal weighting of the model coefficients and limiting the eddy viscosity growth in rapidly strained flows. The switching between the k-ω and k-ε models is achieved using blending functions for the values of the model coefficients. To blend the k-ω and k-ε models, the latter is rewritten using a transformation of variables into a k-ω like form. As a result of the transformation of variables, an additional cross-diffusion term appears in the ω equation corresponding to the k-ε model. The k-ω SST model allows simple Dirichlet boundary conditions to be specified at the wall for the transported turbulence quantities.

The SST model has a performance very similar to that of the original k-ω model, but without the undesirable free-stream dependency. The new model was found to lead to improvements in the prediction of adverse pressure gradient flows. Several studies have shown that SST is one of the most accurate RANS models in predicting complex vortical flows like the ones considered in the present study where massive flow separation occurs as the airflow is convected past the panels.

The SST model is similar to the standard k-ω model for which the equations are given as:

$$\frac{\partial}{\partial t}(\rho k) + \frac{\partial}{\partial x_i}(\rho k u_i) = \frac{\partial}{\partial x_j}(\Gamma_k \frac{\partial k}{\partial x_j}) + G_k - Y_k \quad (1)$$

$$\frac{\partial}{\partial t}(\rho \omega) + \frac{\partial}{\partial x_i}(\rho \omega u_i) = \frac{\partial}{\partial x_j}(\Gamma_\omega \frac{\partial \omega}{\partial x_j}) + G_\omega - Y_\omega + D_\omega \quad (2)$$

In these equations $\rho$ is the density, $k$ is the turbulent kinetic energy, $u_i$ is the velocity component in the i direction, $t$ is the time and $\omega$ is the specific dissipation rate. $G_k$ represents the generation of turbulent kinetic energy due to mean velocity gradients. $G_\omega$ represents the generation of ω. $\Gamma_k$ and $\Gamma_\omega$ represent the effective diffusivity of k and ω, respectively. $Y_k$ and $Y_\omega$ are the dissipation of k and ω due to the turbulence. $D_\omega$ represents the cross diffusion term.

The effective diffusivity for the SST model is given by:

$$\Gamma_k = \mu + \frac{\mu_t}{\sigma_k} \tag{3}$$

$$\Gamma_w = \mu + \frac{\mu_t}{\sigma_\omega} \tag{4}$$

where $\mu$ is the molecular viscosity of the flow and $\mu_t$ is the turbulent viscosity. $\sigma_k$ and $\sigma_w$ are the turbulent Prandtl numbers for k and ω, respectively. The turbulent viscosity $\mu_t$ is computed as follows:

$$\mu_t = \frac{\rho k}{\omega} \frac{1}{\max\left[\frac{1}{\alpha^*}, \frac{\Omega F_2}{a_1 \omega}\right]} \tag{5}$$

where $\Omega$ may be computed as

$$\Omega \equiv \sqrt{2\Omega_{ij}\Omega_{ij}} \tag{6}$$

The expressions for the model coefficients are:

$$\sigma_w = \frac{1}{F_1/\sigma_{\omega,1} + (1-F_1)/\sigma_{\omega,2}} \tag{7}$$

$$\sigma_k = \frac{1}{F_1/\sigma_{k,1} + (1-F_1)/\sigma_{k,2}} \tag{8}$$

where $\Omega_{ij}$ is the mean rate of rotation tensor and the coefficient $\alpha^*$ is introduced to damp the turbulent viscosity and it acts as a low-Reynolds number correction. It is given by:

$$\alpha^* = \alpha^*_\infty \left( \frac{\alpha^*_0 + \mathrm{Re}_t/R_k}{1 + \mathrm{Re}_t/R_k} \right) \tag{9}$$

where

$\mathrm{Re}_t = \dfrac{\rho k}{\mu\omega}, R_k = 6, \alpha_0^* = \dfrac{\beta_i}{3}, \beta_i = 0.072$.

For the high Reynolds-number version of the SST model, $\alpha^*$ and $\alpha_\infty^*$ are assumed to be one. The blending functions $F_1$ and $F_2$ are given by

$$F_1 = \tanh(\phi_1^4) \tag{10}$$

$$\phi_1^4 = \min\left[\max\left(\frac{\sqrt{k}}{0.09\omega y}, \frac{500\mu}{\rho y^2 \omega}\right), \frac{4\rho k}{\sigma_{\omega,2} D_\omega^+ y^2}\right] \tag{11}$$

$$D_\omega^+ = \max\left[2\rho \frac{1}{\sigma_{\omega,2}} \frac{1}{\omega} \frac{\partial k}{\partial x_j} \frac{\partial \omega}{\partial x_j}, 10^{-20}\right] \tag{12}$$

$$F_2 = \tanh(\phi_2^2) \tag{13}$$

$$\phi_2^2 = \max\left(2\frac{\sqrt{k}}{0.09\omega y}, \frac{500\mu}{\rho y^2 \omega}\right) \tag{14}$$

The blending function $F_2$ served to modify the formulation of the eddy viscosity inside the boundary layers, such that the k-ω SST model can better account for the transport of the turbulent stresses. Its expression depends on the wall distance, *y*. This leads to significantly improved predictions of separated flows by avoiding common problems observed with the standard k-ω model (e.g., under-prediction of the separation caused by adverse pressure gradients).

The term $G_k$ represents the production of turbulent kinetic energy, and is defined similarly as in the standard k-ω model.

$$G_k = \mu_t S^2 \tag{15}$$

where $S$ is the magnitude of the rate of strain tensor. The term $G_\omega$ represents the production of ω and is given by

$$G_\omega = \frac{\alpha}{\nu_t} G_k \tag{16}$$

Note that this formulation differs from the standard k-ω model. Another difference between the k-ω and SST models is in the way the term $\alpha_\infty$ is evaluated. In the standard k-ω model $\alpha_\infty$ is defined as a constant, $\alpha_\infty = 0.52$. In the SST model, $\alpha_\infty$ is given by

$$\alpha_\infty = F_1 \alpha_{\infty,1} + (1 - F_1)\alpha_{\infty,2} \tag{17}$$

$$\alpha_{\infty,1} = \frac{\beta_{i,1}}{\beta_\infty^*} - \frac{\kappa^2}{\sigma_{\omega,1}\sqrt{\beta_\infty^*}} \tag{18}$$

$$\alpha_{\infty,2} = \frac{\beta_{i,2}}{\beta_\infty^*} - \frac{\kappa^2}{\sigma_{\omega,2}\sqrt{\beta_\infty^*}} \tag{19}$$

where κ is 0.41 and $\beta_{i,1}$ and $\beta_{i,2}$ are 0.075 and 0.0828 respectively. The term $Y_k$ represents the dissipation of turbulence kinetic energy.

$$Y_k = \rho \beta^* k \omega \tag{20}$$

The term $Y_\omega$ represents the dissipation of ω.

$$Y_\omega = \rho \beta_i \omega^2 \tag{21}$$

Instead of having a constant value, $\beta_i$ is given by

$$\beta_i = F_1 \beta_{i,1} + (1 - F_1)\beta_{i,2} \tag{22}$$

where $\beta_{i,1}$ and $\beta_{i,2}$ are 0.075 and 0.0828 respectively. To blend the k-ε and k-ω models together, the standard k-ε model equations have been transformed into equations based on k and ω, which leads to the introduction of a cross-diffusion term ($D_\omega$). In the SST formulation $D_\omega$ is defined as

$$D_\omega = 2(1 - F_1)\rho \sigma_{\omega,2} \frac{1}{\omega} \frac{\partial k}{\partial x_j} \frac{\partial \omega}{\partial x_j} \tag{23}$$

The other model constants are:

$$\begin{aligned} &\sigma_{k,1} = 1.176 \quad \sigma_{\omega,1} = 2.0 \\ &\sigma_{k,2} = 1.0 \quad \sigma_{\omega,2} = 1.168 \\ &a_1 = 0.31 \quad \beta_{i,1} = 0.075 \quad \beta_{i,2} = 0.0828 \end{aligned} \tag{24}$$

A mass outflow boundary was used in the exit section in all simulations. The lateral boundaries were placed at a large distance from the panel and symmetry boundary conditions were used. The DMS cabinet surfaces were treated as a no slip surface. The flow in the streamwise direction was uniform in the inflow section that was placed at a considerable distance upstream of the DMS and the truss.

### 2.2 Structural response analysis

ANSYS (ANSYS User's Manual, 2005) was used to conduct the structural analysis component of the study. ANSYS is a general purpose finite element program capable of performing static and dynamic analysis of any structure modeled with suitable elements. It can take into account nonlinear material properties as well as geometric nonlinearities due to large deformations and rotations. The highway structures considered in this project were modeled using beam and shell elements (Bhatti 2005 & 2006). The analyses due to code specified loading and those from the CFD modeling that give mean wind effects were conducted using the static analysis procedures, but included geometric nonlinearities.

## 3. CFD Simulations of the wind and truck induced forces

After meeting with the TAC committee, it was decided to concentrate on the first two tasks in the proposal dealing with the effect of wind direction on the forces acting on the DMS cabinet and the behavior of typical trusses supporting the DMS cabinets. It was decided that dynamic effects related to unsteady vortex shedding behind the DMS cabinets should be ignored for the purpose of the present analysis. Instead, a much more complex model that included not only the DMS but also the truss (all the truss members were included which allowed estimation of wind forces on each member in addition to the forces acting on the DMS cabinet) was generated and used to understand the effect of the wind on the truss members. Additionally, a simplified procedure that accounts for the presence of a truck underneath the DMS was proposed to try to estimate forces generated by the passage of a truck underneath the DMS. This is because in the initial stages of the study the IDOT was concerned about fatigue generated by the repeated passage of trucks underneath the DMS. Among the proposed matrix of CFD test cases to be considered, the TAC asked us to conduct:

3.1- a parametric study with the wind direction for the flow past an isolated DMS cabinet with no other obstacles except the presence of the ground which was not considered in the previous study. The wind velocity was constant and equal to 90 mph.

3.2- a study of the effect of the truss on which the DMS cabinet is attached. The wind velocity was constant and equal to 90 mph. Besides the base case, an additional simulation with the same DMS and a wind velocity of -90 mph and a simulation with a flat plate and a wind velocity of 90 mph were performed. Information on the forces acting on the truss members may be of interest for a more detailed structural analysis.

3.3- a study of the effect of the passage of a long truck beneath the DMS cabinet. The wind velocity was constant and equal to 90 mph. The truck velocity was constant and equal to 60, -60 and 0 mph, respectively. The truck moved either in the wind direction or in the opposite direction. This study also considered the effect of the presence of the truss.

3.4- a study of the effect of the passage of a long truck beneath the DMS cabinet for no wind conditions. The truck velocity was constant and equal to 60 mph.

3.5- a study of the effect of the passage of a long truck beneath the DMS cabinet for low wind conditions (5 mph) corresponding to the average wind conditions at the DMS during the field experiments. The truck velocity was constant and equal to 60 mph.

For all these cases the forces in the three directions acting on the DMS cabinet and the truss members were obtained as part of the CFD analysis. The main results are summarized below.

### 3.1. Effect of wind direction for an isolated DMS cabinet

We ran 5 simulations of the air flow past a DMS cabinet for the case the DMS was situated at a given height above the ground (~17 ft). Thus the constriction effect as the airflow that is convected below the DMS is taken into account in this series of simulations. The dimensions of the DMS cabinet (29.25 ft x 7.833 ft) and its position relative to the ground are identical to the ones in the document made available to us by the TAC. The simulations took into account the fact that one of the faces of the DMS cabinet was slightly tapered with respect to the vertical (frontal face is slightly inclined toward traffic, see Fig. 3). The wind speed was 90 mph in all the cases. The only parameter that was varied was the free stream wind direction in the horizontal plane. Table 1 summarizes the pressure forces on the front and back faces of the DMS cabinet and the net force acting on the DMS cabinet along the wind direction.

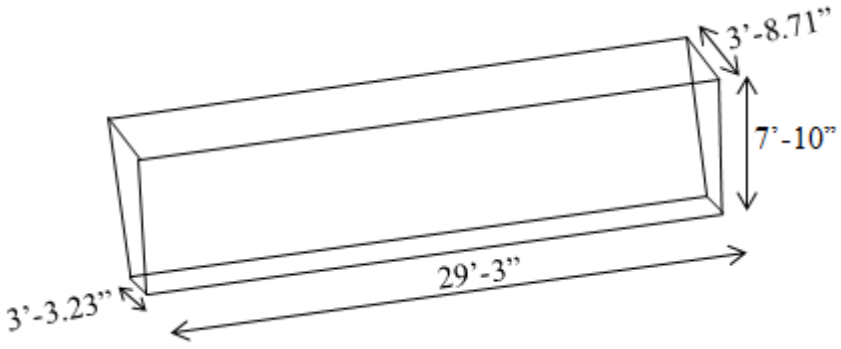


Fig. 3 Sketch of a DMS panel showing main dimensions

For comparison using the AASHTO formula for wind loading for a design wind velocity of 90 mph (~50 m/s), the pressure is in the range of 28 to 30 psf. One should also mention that the IDOT now uses a design wind-load pressure of about 40 psf for DMS cabinets mounted on an overhead truss (e.g., that was the case of a truss monitored at Kellogg site).

$$\Delta P = K_z G V I_r C_d \qquad (25)$$

where

$K_z$ = height and exposure factor (~1.0)

G = gust effect factor (~1.14)

V = design wind velocity (generally 90 mph)

$I_f$ = importance factor (=1)

$C_d$ = drag coefficient

Typical values for $C_d$ are 1.2-1.27 but values of $C_d$ as high as 1.7 are sometimes assumed. For the base case in which the wind direction was perpendicular to the DMS cabinet (Case 5, Fig. 4), the estimated net pressure is 29.3 psf assuming $C_d$=1.25. Of course an increase in the value of $C_d$ will result in an increase of $\Delta P$. This value is slightly larger than the one estimated in the previous study (24-26.8 psf) conducted for similar cabinets but without inclusion of the presence of the ground surface. As the angle between the wind and the front face of the DMS starts decreasing, the pressure distribution becomes nonsymmetrical (e.g., see Fig. 5 for Case 4) and the net pressure force in the streamwise direction starts decreasing (Table 1).

As expected, for the case in which the wind direction is parallel to the front/back faces of the DMS cabinets (Case 1, Fig. 6), the net force is negligible. Even if one accounts for the pressure net force acting on the side faces of the DMS cabinets (Fig. 7), the total force along the wind direction is negligible (0.4 psf).

The decrease in the pressure force along the wind direction with the angle between the wind direction and the front/back faces of the DMS cabinet can be inferred from Table 1.

Table 1 Net pressure force in the wind direction for isolated DMS with 90 mph wind

| **Case** | **Wind Direction (degree)** | **Average Pressure Nondimensional** | | $\Delta P = P_{ave}^{front} - P_{ave}^{back}$ **Nondimensional** | $\Delta P$ **(Psf)** | $\Delta F$ **(Pound-force)** |
|---|---|---|---|---|---|---|
| | | **Front** | **Back** | | | |
| 1<br>Sidewall surfaces | 0 | -0.0636<br>0.00817 | -0.0632<br>-0.0012 | -0.0004<br>0.00936 | (0.0168)<br>(0.3948) | ~0.<br>10.332 |
| 2 | 22.5 | 0.113 | -0.167 | 0.280 | 11.8 | 2150. |
| 3 | 45 | 0.208 | -0.316 | 0.524 | 22.1 | 5060 |
| 4 | 67.5 | 0.325 | -0.28 | 0.605 | 25.5 | 5842 |
| 5 | 90 | 0.402 | -0.293 | 0.695 | 29.3 | 6700 |

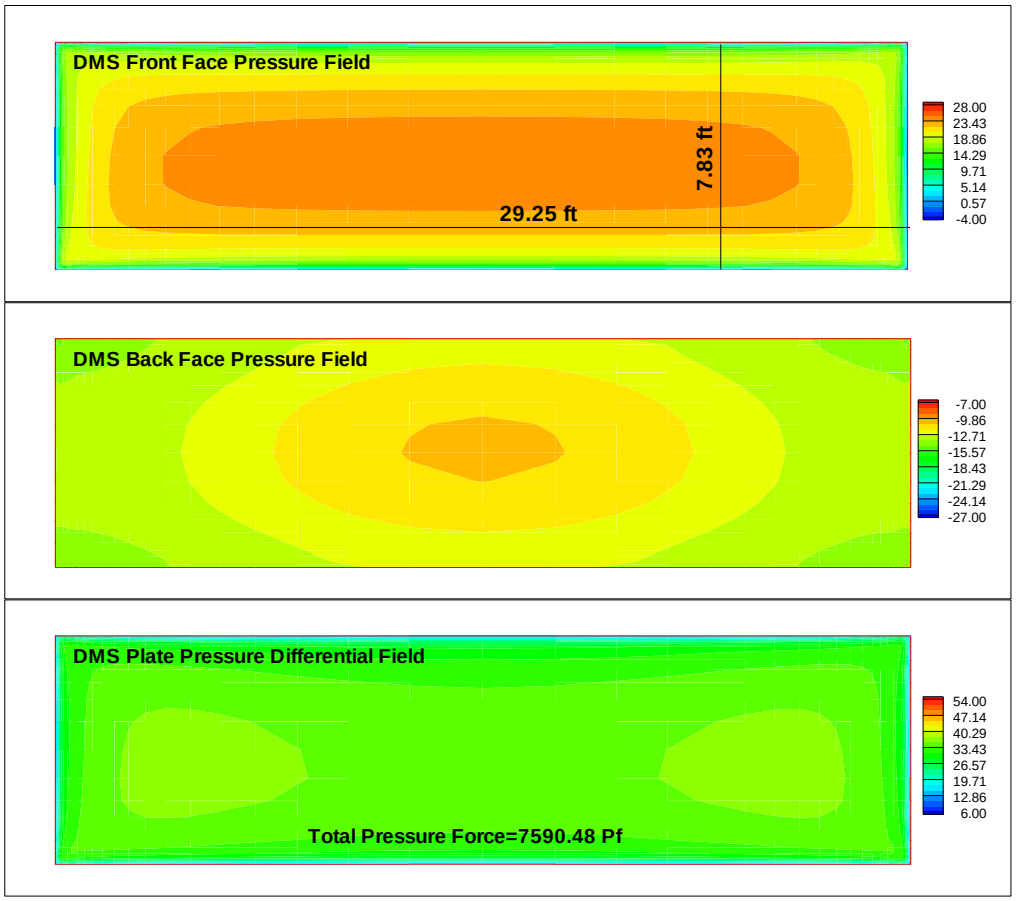


Fig. 4 Distribution of the pressure forces on the front and back faces of the DMS cabinet together with the net pressure force for Case 5 in which the wind direction is perpendicular to the front/back faces

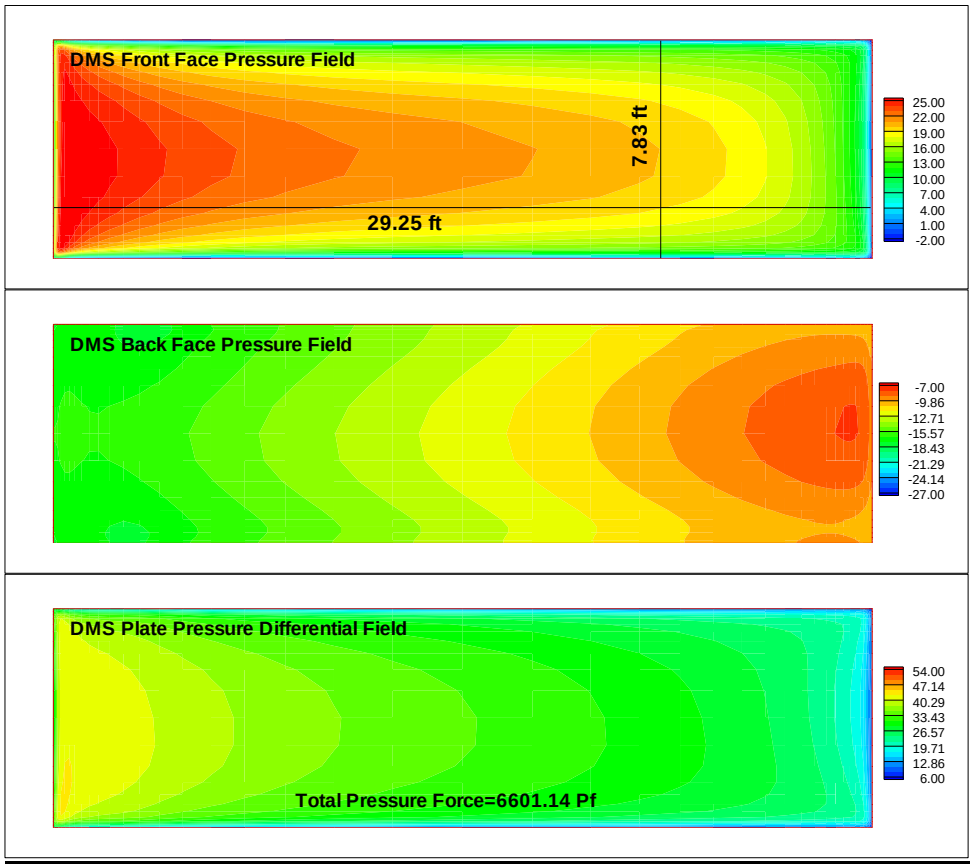


Fig. 5 Distribution of the pressure forces on the front and back faces of the DMS cabinet together with the net pressure force for Case 4 in which the wind direction makes an angle of 67 degrees with the front/back faces

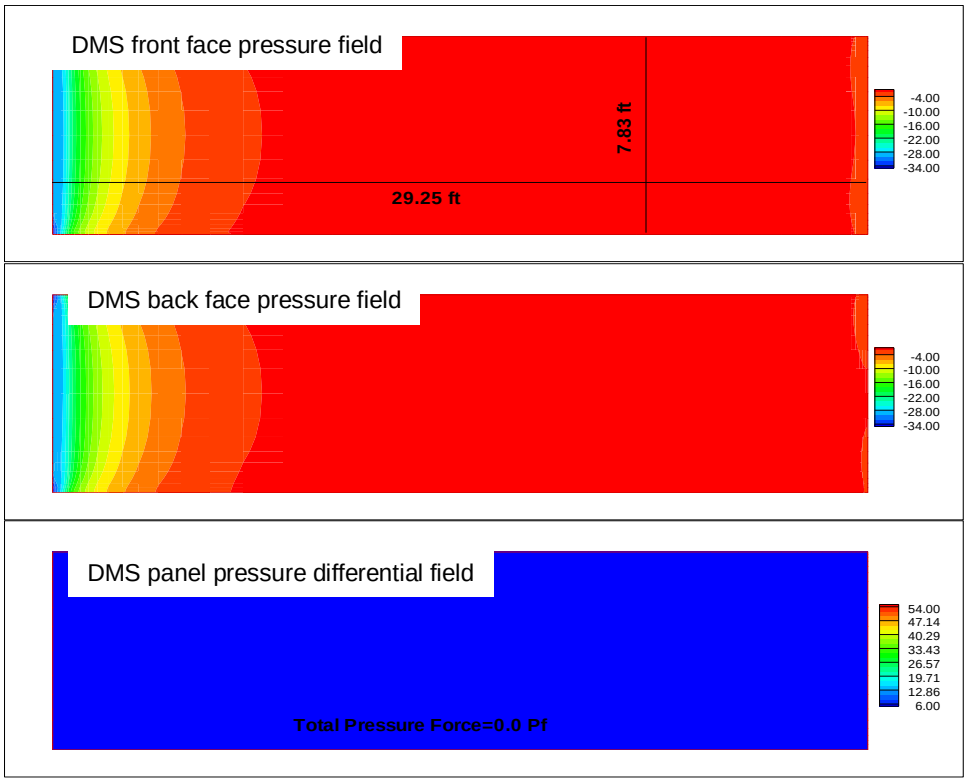


Fig. 6 Distribution of the pressure forces on the front and back faces of the DMS cabinet together with the net pressure force for Case 1 in which the wind direction is parallel to the front/back faces

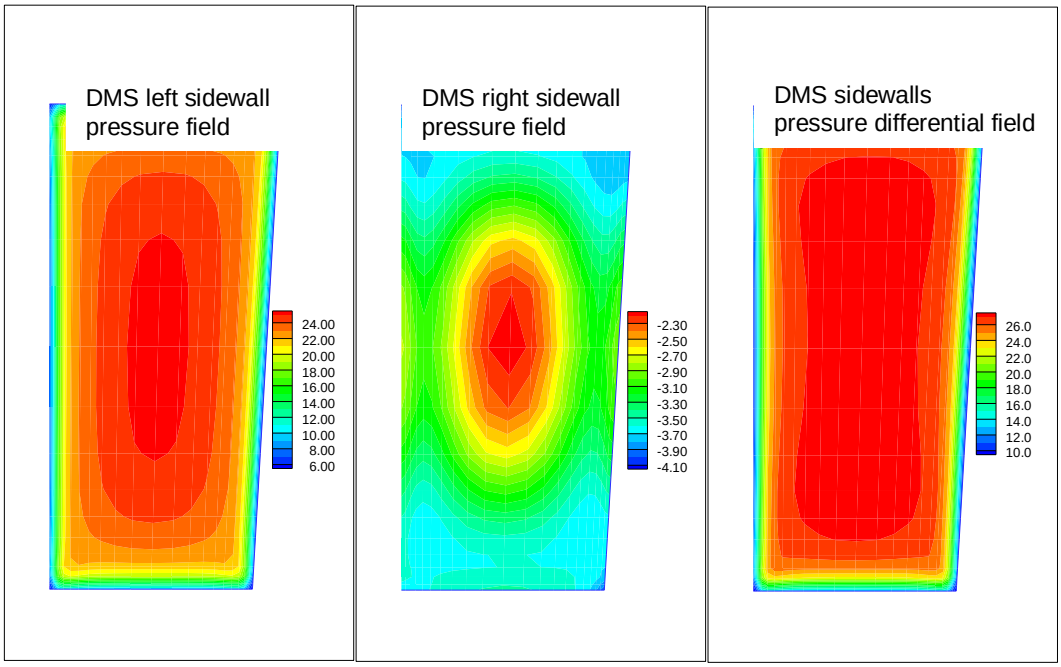


Fig. 7 Distribution of the pressure forces on the two sidewall faces of the DMS cabinet together with the net pressure force for Case 1 in which the wind direction is parallel to the front/back faces and perpendicular to the two sidewall faces

### 3.2. Effect of the truss for an isolated DMS cabinet

In the previous subsection the DMS cabinet was positioned above the ground but the truss was not included in the calculation. The inclusion of the truss on which the DMS is attached may slightly change the flow field around the DMS cabinet because of the additional obstruction of the flow around the DMS cabinet induced by the truss members. Figure 8 shows a sketch of the truss used in the simulations. The truss geometry was determined based on the specifications provided by the Iowa DOT. One should mention that the model truss used in the CFD model does not have the truss members for the uprights. This is an acceptable approximation for the CFD. The effect of attaching the DMS cabinet on the truss is to change dramatically the forces acting on the truss members that are shielded by the DMS cabinet. Most of these members are situated in the recirculating flow region induced by the DMS cabinet. The streamwise forces on the truss members not shielded by the DMS cabinet but situated close to it are expected to slightly increase with respect to the case when no DMS cabinet is attached on the truss. This detailed information on the forces acting on the truss members is of interest for a more detailed structural analysis that accounts not only for the forces induced on the truss by the wind loads on the DMS cabinet but also for the wind loads on the individual members of the truss. The sketch in Fig. 9 shows the convention used to identify the individual members of the truss. CFD provides the resultant wind force acting in each of the three directions on the individual members.

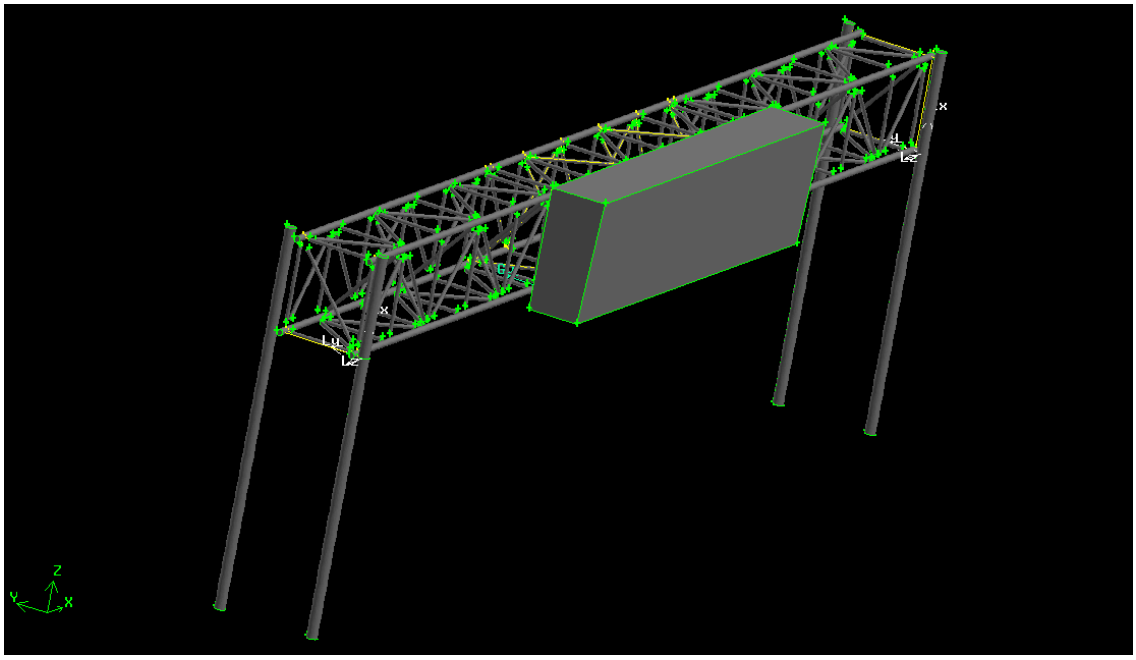

Fig. 8 Sketch showing the truss on which the DMS cabinet is attached

In the first two simulations performed, the wind velocity was constant and equal to 90 mph. In the first simulation only the truss was present (Fig. 10). In the second simulation the DMS cabinet was attached to the truss, as shown in Fig. 12. The second simulation is labeled as Case B in Table 2. The base case corresponding to an isolated DMS with a wind blowing perpendicularly to the face of the DMS cabinet and is labeled as Case A in Table 2 (same as Case 5 in Table 1). The main reason to perform the first simulation was to estimate the wind

loads in the streamwise (wind) direction for the truss members, in particular for the ones situated behind the DMS cabinet in the second simulation (Case B). The mesh in all these simulations contained close to 4 million cells needed to obtain a sufficiently fine mesh around the individual members of the truss.

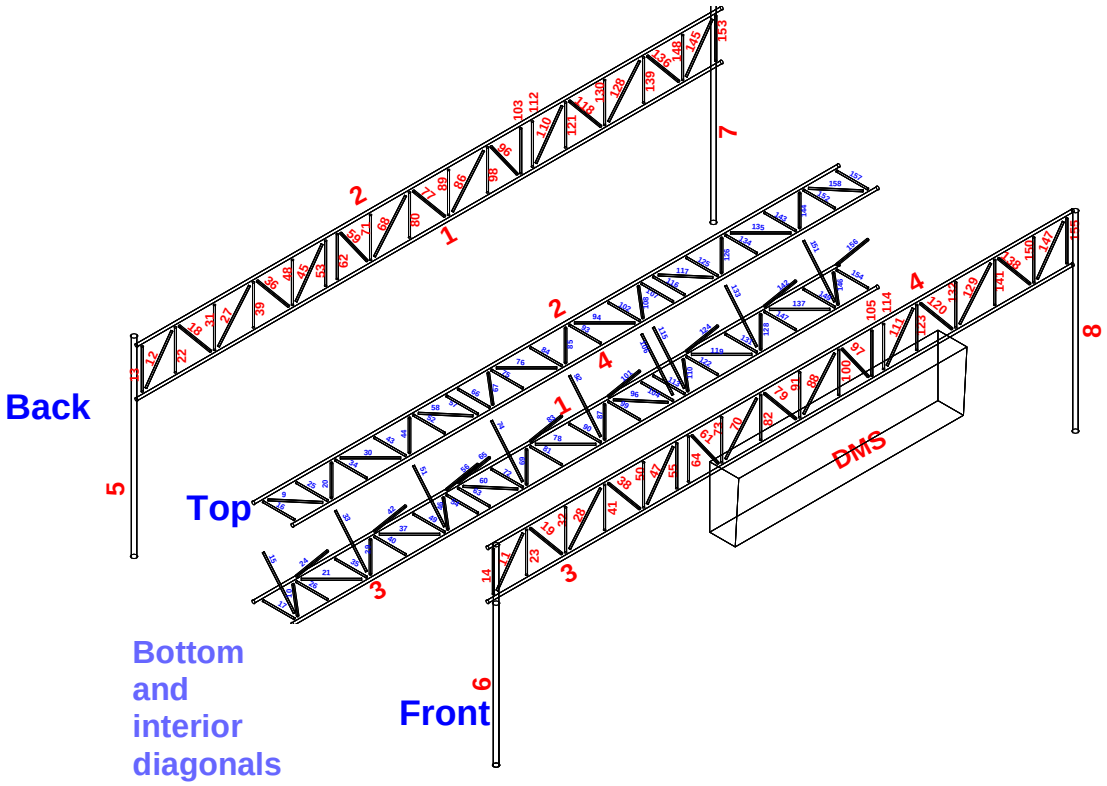


Fig. 9 Sketch showing the convention used to identify the individual members of the truss. CFD provides the resultant wind force acting in each of the three directions on the individual members.

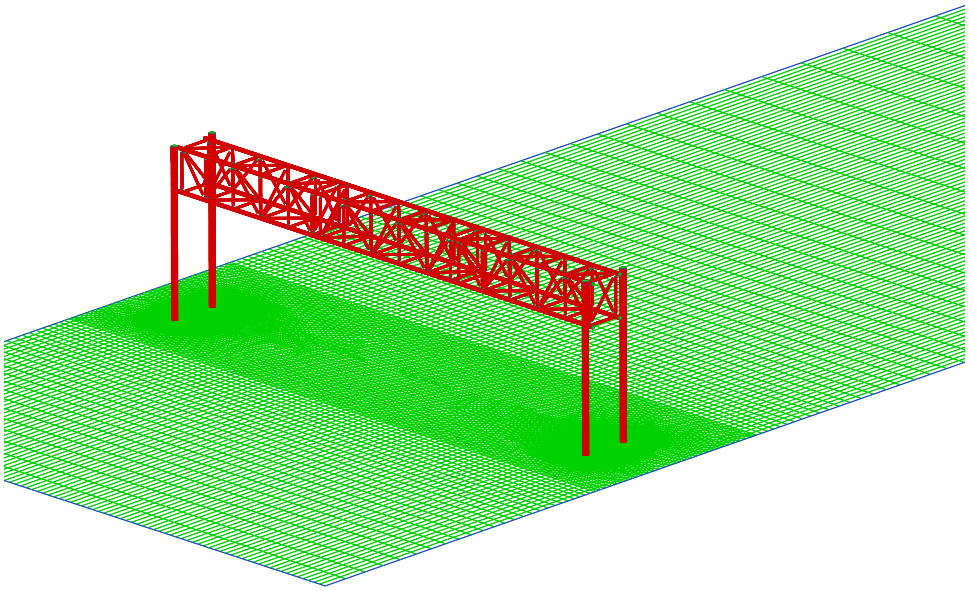

Fig. 10 View of the computational domain in the simulation in which no DMS cabinet is attached to the truss. The wind speed is 90 mph.

Table 2 Resultant mean pressure force on opposing faces of DMS cabinet for the simulations with a 90 mph wind blowing perpendicular to the DMS cabinet. If not specified otherwise, the wind velocity in each simulation is 90 mph.

| | Force (Pound Force) | | | |
|---|---|---|---|---|
| DMS Face | Streamwise Direction | Spanwise Direction | Vertical Direction | Geometry |
| front and back | 6739.39 | 0.00 | 404.73 | no truss, truck V=-60mph (Case E) |
| top and bottom | 0.00 | 0.00 | -166.68 | |
| left and right | 0.00 | -14.33 | 0.00 | |
| front and back | 6815.55 | 0.00 | 409.02 | no truss, truck V=60mph (Case F) |
| top and bottom | 0.00 | 0.00 | -165.16 | |
| left and right | 0.00 | -12.40 | 0.00 | |
| front and back | 6899.548 | 0.000 | 414.371 | with truss, truck V=-60mph (Case G) |
| top and bottom | 0.000 | 0.000 | -152.570 | |
| left and right | 0.000 | -3.496 | 0.000 | |
| front and back | 6893.426 | 0.000 | 414.331 | with truss, truck V=60mph (Case H) |
| top and bottom | 0.000 | 0.000 | -157.085 | |
| left and right | 0.000 | -3.197 | 0.000 | |
| front and back | 6895,55 | 0 | 414.32 | |
| top and bottom | 0 | 0 | -155.2 | with truss, truck V=0mph (Case I) |
| left and right | 0 | 0 | 0 | |
| front and back | 6889.419 | 0.000 | 412.554 | with truss, no truck (Case B) |
| top and bottom | 0.000 | 0.000 | -86.240 | |
| left and right | 0.000 | 3.898 | 0.000 | |
| front and back | -5924.7 | 0 | 396.4 | |
| top and bottom | 0 | 0 | -106..1 | with truss, no truck |
| left and right | 0 | -2.1 | 0 | wind Velocity=-90mph (Case D) |
| front and back | 7897.67 | 0 | 0 | |
| top and bottom | 0 | 0 | 0 | with truss, no truck |
| left and right | 0 | 0 | 0 | thin plate instead of DMS (Case C) |
| front and back | 6700.532 | 0.000 | 404.427 | no truss, no truck (Case A) |
| top and bottom | 0.000 | 0.000 | -97.025 | |
| left and right | 0.000 | -23.530 | 0.000 | |

As expected, results for the first simulation (Case A in Table 2) show that all members of the truss that are directly exposed to the wind (e.g., front face of the truss) are subjected to fairly large streamwise wind loads that are proportional to the projected area. These forces are induced by the flow deceleration as it passes the individual members. That results in a large increase of the pressure on the frontal (upstream) face of these members around the stagnation flow region (e.g., see regions of high –red- pressure in Fig. 11). The average pressure force in the streamwise direction on the small cylindrical elements located on the frontal face of the truss is around 30 psf. The truss acts as a porous obstacle that induces a region of pressure increase upstream of the region where it is situated. However, with the exception of the small recirculating flow regions behind individual truss members, there is no flow separation region behind the truss.

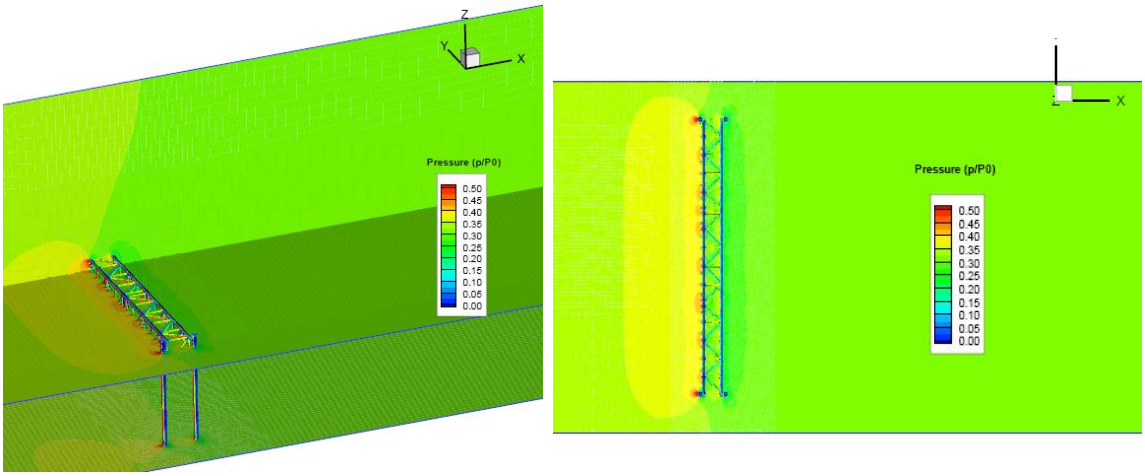


Fig. 11 Pressure distribution in 3D (left frame) and a horizontal plane showing the large amplification of the pressure in the stagnation flow region of the truss members exposed to the wind. Results are shown for the simulation in which no DMS cabinet is attached to the truss. The wind speed is 90 mph. Wind direction is from left to right.

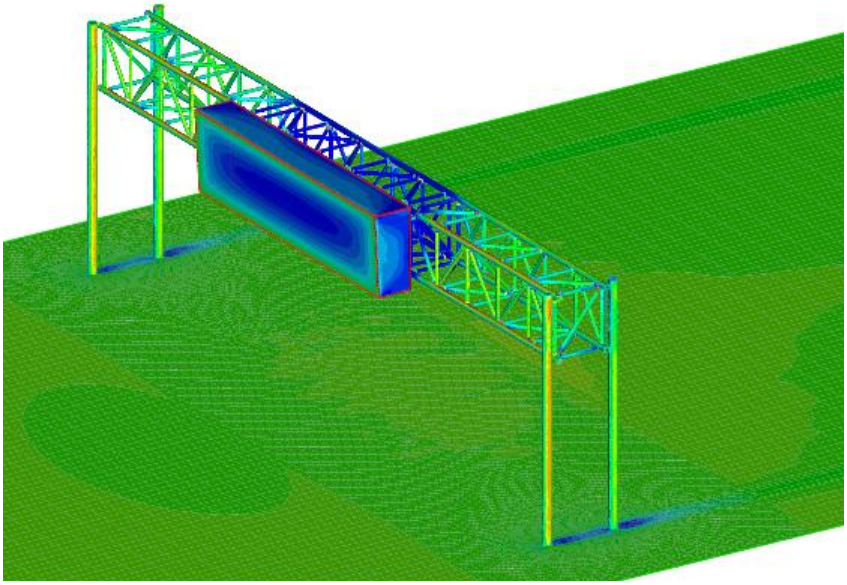

Fig. 12 View of the computational domain in the simulation (Case B) in which the DMS cabinet is attached to the truss. The wind speed is 90 mph.

In the second simulation (Case B in Table 2), the flow field around the truss members that are not situated immediately behind the DMS cabinet is relatively similar to the one observed in the first simulation. In fact, the streamwise pressure force is slightly higher on the members situated close to the lateral edges of the DMS cabinet because the flow deflected past the DMS cabinet has a slightly larger streamwise velocity compared to the incoming wind velocity. The DMS is a non-porous plate that induces a large deceleration of the flow and a large recirculation region behind it. The flow deceleration region downstream of the DMS cabinet is the strongest in horizontal planes cutting through the DMS cabinet (Fig. 13b) but it extends for some distance above and below the DMS cabinet (Figs. 13a and 13c). Figure 14 visualizes the distribution of the pressure and velocity magnitude in representative vertical and horizontal planes around the

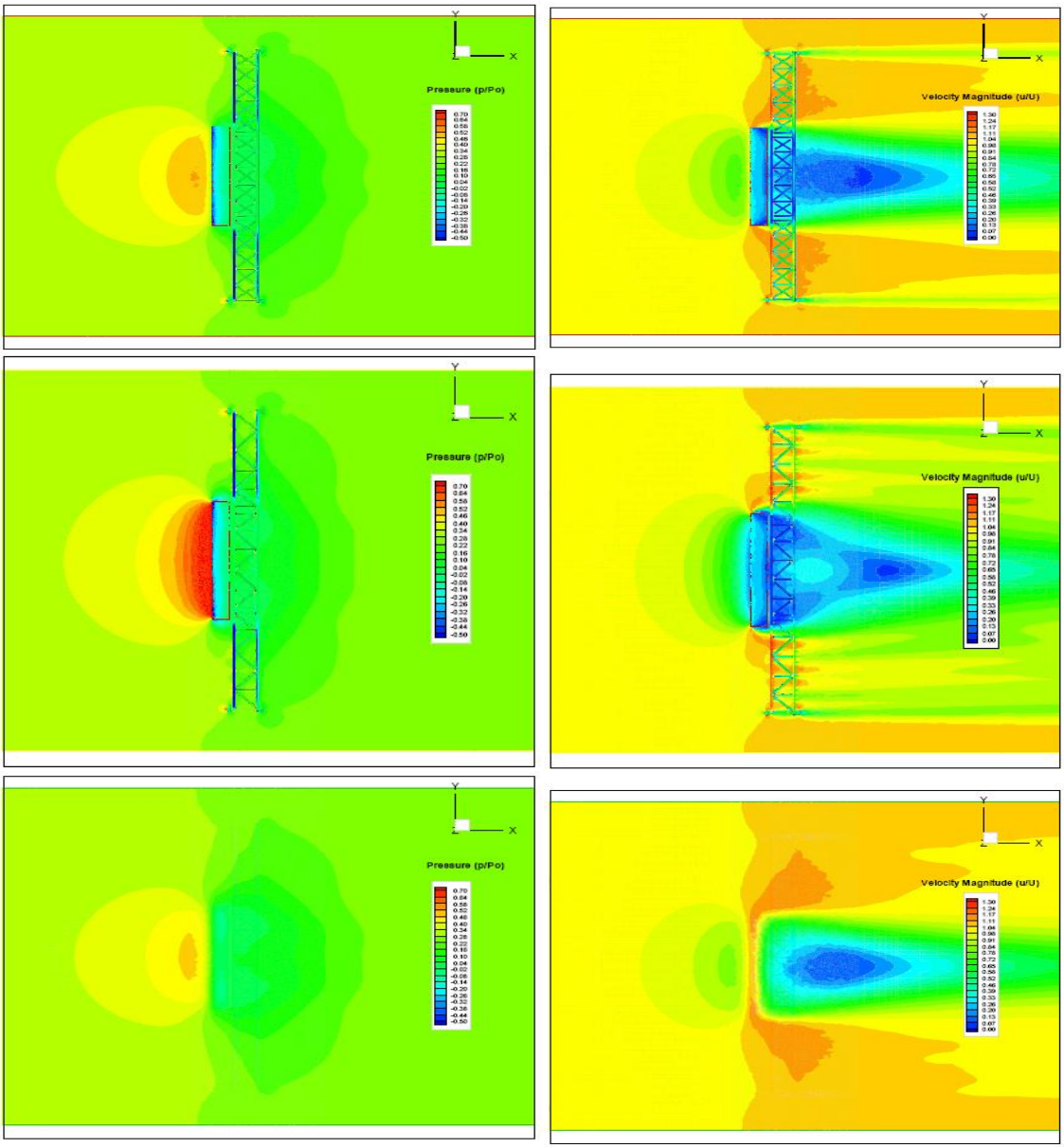


Fig. 13 Distribution of pressure (left) and velocity magnitude (right) in three horizontal planes cutting under the DMS (top), through the DMS (middle) and over the DMS (bottom) in the simulation (Case B) in which the DMS cabinet is attached to the truss. The wind speed is 90 mph. Wind direction is from left to right.

DMS cabinet and the truss. Most of the truss members behind the DMS cabinet are situated within this flow recirculation region where the velocity, including the streamwise velocity component, is very small. As a result, the pressure force in all three directions is quite small on these trusses. For example, in the first simulation the streamwise load on members 79 and 88 (Fig. 9) was close to 37 psf and the force on members 100 and 91 (Fig. 9) was close to 24 psf. In Case B, the streamwise load on the four members is around -1 psf. On the other hand, the forces on the members not shielded by the DMS cabinet continue to be high and comparable to the ones predicted in the first simulation. As part of the simulation, we obtained the pressure forces (all

three directions) acting on all individual members of the truss and on the DMS cabinet. This will allow performing a more detailed structural analysis of the truss.

In terms of the wind loads acting on the DMS cabinet, the presence of the truss (case B) had only a small effect on the resultant wind load force in the streamwise (3% increase due to the presence of the truss) and vertical directions compared to the base case in which the truss was not present (case A in Table 2).

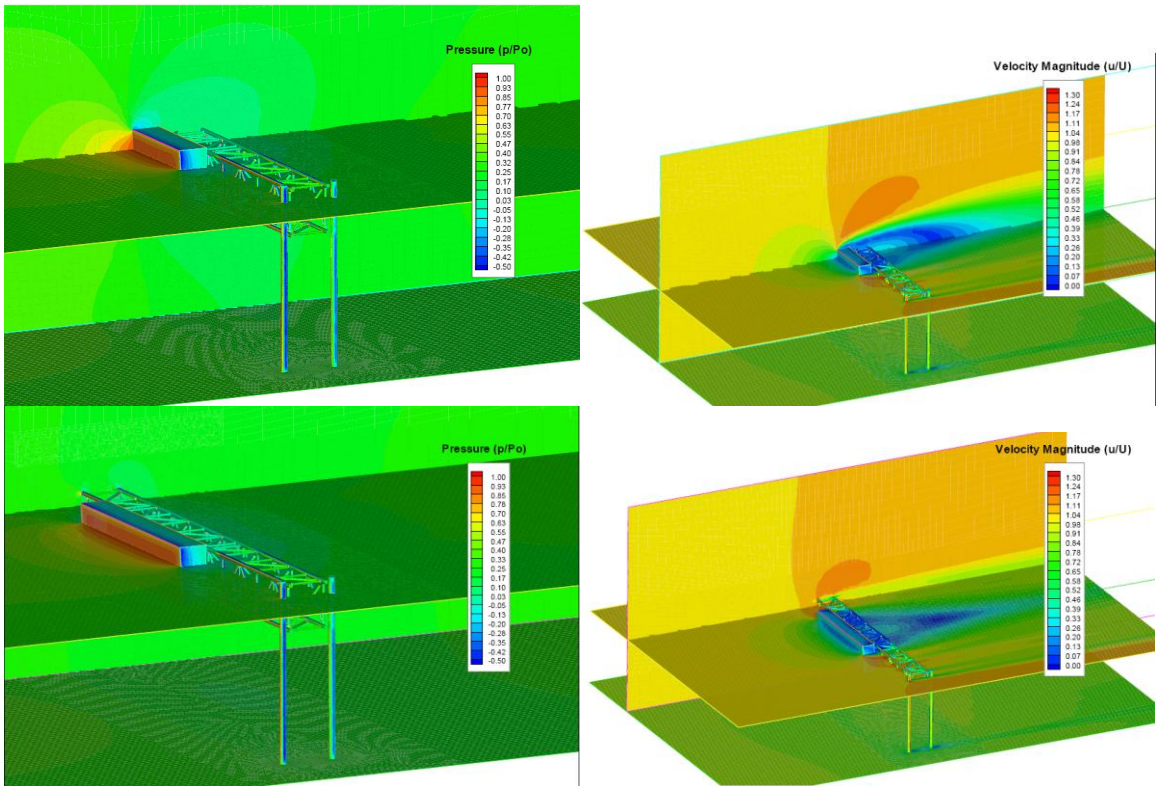


Fig. 14 Distribution of pressure (left) and velocity magnitude (right) in horizontal and vertical planes cutting through the middle of the DMS cabinet (top) and through the truss (bottom) in the simulation (Case B) in which the DMS cabinet is attached to the truss. The wind speed is 90 mph. Wind direction is from left to right.

Two additional simulations were performed. In one of these simulations the DMS was replaced by a thin flat plate of same cross section as the one of the DMS (case C). The wind velocity was the same (90 mps). Results in Table 2 show that the pressure force on the DMS increased by about 14% from 6889 to 7897 pound-force. This result is fully consistent with the one reported in the previous CFD study for DOT in which two similar simulations were performed for an isolated plate and an isolated DMS (no truss, same wind velocity). In the other simulation the wind magnitude was left the same but the wind direction was changed by 180 degrees, such that the incoming wind first encounters the members of the truss and then the back of the DMS (case D). Because of the shielding effect of the truss members situated upstream of the face of the DMS, the streamwise pressure force is expected to decay. Results of the base case and of the simulation with a wind velocity of -90 mph confirm this and predict a decay of around 12% of the streamwise pressure force. On the other hand, the force on the truss members situated in front

of the DMS will be larger in the simulation with -90 mph. So, one expects that the total force on the truss members and DMS will be roughly equal in the two cases.

### 3.3. Effect of the passage of a truck under the DMS cabinet for windy conditions

The effect of the passage of a vehicle under the DMS cabinet is of great concern to the Iowa DOT. This problem is very complex from the CFD point of view because, in principle, one has to simulate the movement of the truck relative to the ground and the DMS cabinet. Such a simulation would be extremely time consuming and computationally expensive as it will require the use of moving meshes. In the present study, the effect of the truck passage under the DMS is accounted for in an approximate way. The key idea is to assume that the truck is 'very long'. This reduces the problem to a much simpler steady state calculation, similar to the other CFD simulations reported in this study. The simulations in which a long truck is present beneath the DMS cabinet should account for the suction effect (negative pressure force in the vertical direction acting on the DMS) induced by the truck on the DMS cabinet.

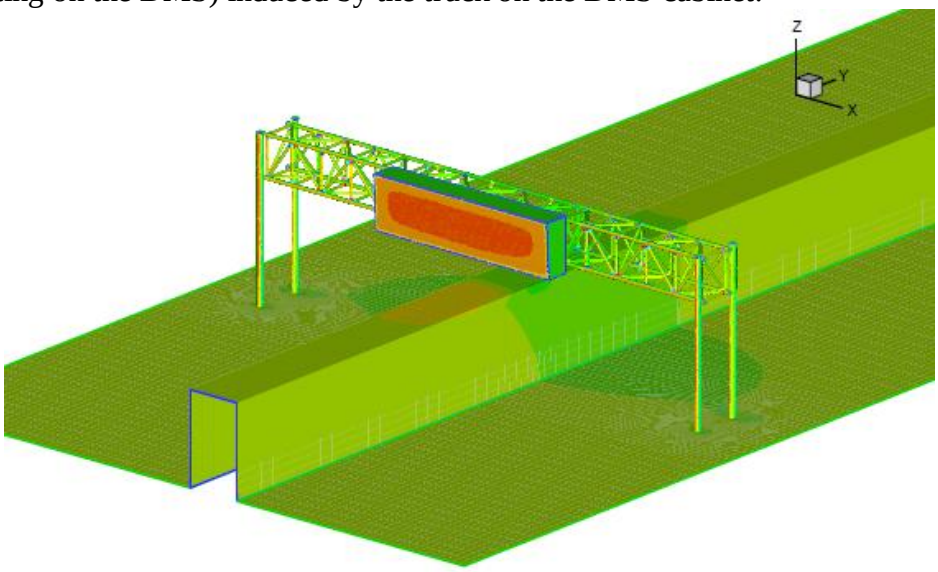


Fig. 15 View of the computational domain in the simulation (Case H) in which the DMS cabinet is attached to the truss and a truck moves beneath the DMS with a velocity of 60 mph in the direction of the wind. The wind speed is 90 mph. The quantity represented on the faces of the DMS cabinet and of the truss members is the pressure.

Except for the truck, the set up of the simulations and boundary conditions are identical to those used in Cases A and B. The width of the truck is 8 ft and its height is 13.5 ft. The truck is positioned asymmetrically with respect to the axis of the DMS cabinet (Fig. 15), to replicate conditions on a highway in which a truck typically will be traveling in the right lane. The distance between the axis of the DMS cabinet and the axis of the truck is 5 ft. The bottom of the DMS is situated at 17 ft from the ground.

In all simulations, a truck velocity of 60 mph is assumed, while the wind velocity is 90 mph. The truck velocity is specified as a boundary condition on the two lateral faces and the top face of the truck. We conducted simulations in which the truck moved in the same direction as the wind (cases F and H) and with the truck moving in opposite direction (cases E and G). In some of the

simulations only the DMS cabinet and the truck were considered (cases E and F), while in others the truss was also present (cases G and H). The mesh in all these simulations contained close to 4 million cells. Finally an extra case (case I in Table 2) in which the truck velocity was equal to zero was included for completeness in the simulations in which the truss, DMS and truck were present. As expected the wind forces in this case were in between the ones predicted for the corresponding cases in which the truck velocity was +60 mph and -60mph, where the positive sign means wind velocity and truck velocity were in the same direction.

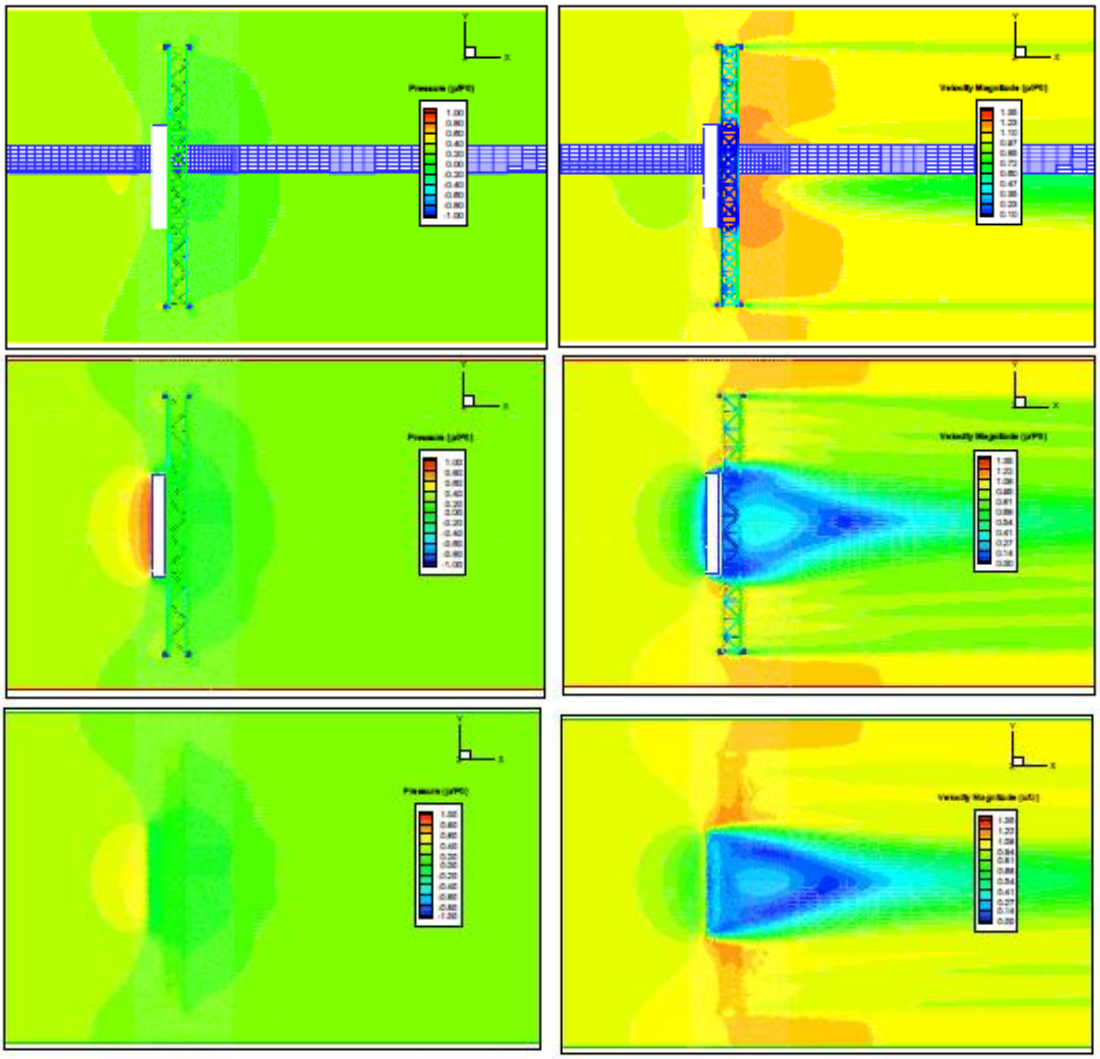

Fig. 16 Distribution of pressure (left) and velocity magnitude (right) in three horizontal planes cutting under the DMS and through the moving truck (top), through the DMS (middle) and over the DMS (bottom) in the simulation (Case H) in which the DMS cabinet is attached to the truss and a truck moves beneath the DMS with a velocity of 60 mph in the direction of the wind. The wind speed is 90 mph. Wind direction is from left to right.

Though the presence of the moving truck alters some of the details of the flow in the region of strong deceleration in front of the DMS and in the recirculation region behind the DMS, especially in horizontal planes situated close to the bottom face of the DMS and below it (compare distributions of the pressure and velocity magnitude in Figs. 13 and 14 for case B with

those in Figs. 16 and 17 for case H), the resultant pressure forces on the DMS cabinet are comparable (see comparison of cases E, F, G, H in Table 2). As expected, the largest differences are observed for the vertical pressure force between the top and bottom faces of the DMS cabinet. This force is induced by suction due to the presence of the DMS, the ground and the truck. The flow accelerates as it passes the DMS due to the decrease in the flow area. As a result, the pressure in that region decreases. This explains why the pressure on the bottom face of the DMS cabinet is smaller than the one on the top face of the DMS cabinet. The presence of the truck in cases E, F, G and H results in a vertical pressure force of about 150-160 psf. The direction of movement of the truck and the presence of the truss were found to have a negligible effect on the suction force. By comparison the vertical suction force on the DMS was around 90 psf in the simulations with no truck. Part of the reason for the moderate effect on the vertical force on the DMS is that the truck occupies only a small percentage of the total width of the DMS. So, the increased suction in between the top of the truck and the bottom face of the DMS acts only over a small region.

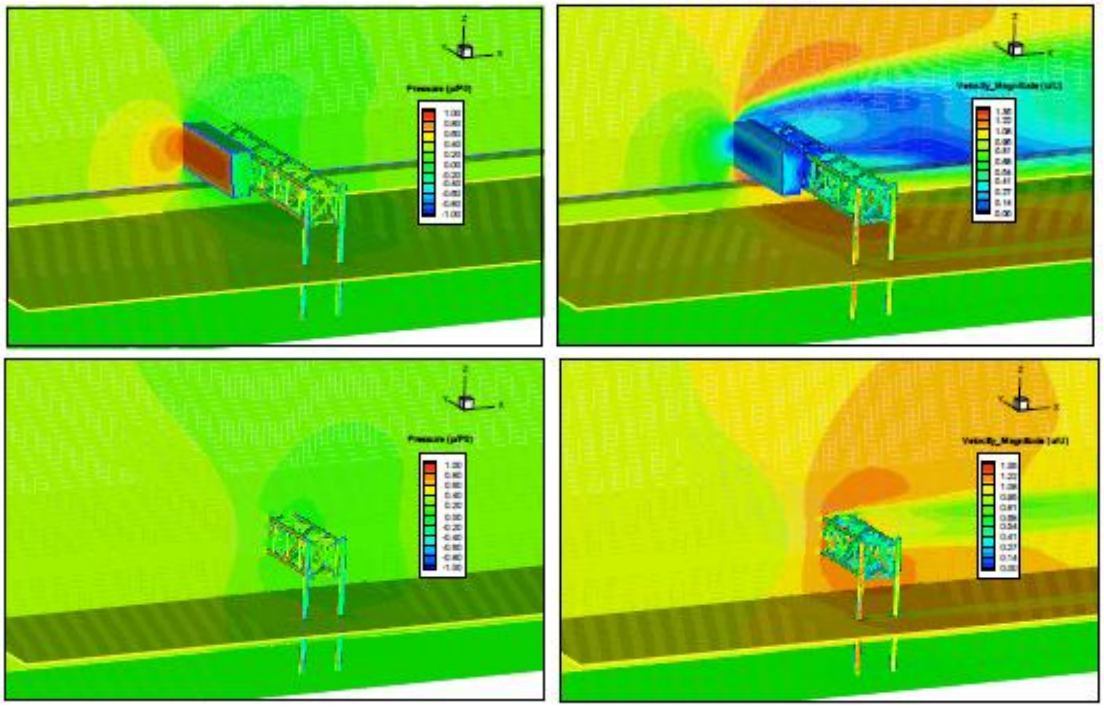

Fig. 17 Distribution of pressure (left) and velocity magnitude (right) in horizontal and vertical planes cutting through the middle of the DMS cabinet (top) and through the truss (bottom) in the simulation (Case H) in which the DMS cabinet is attached to the truss and a truck moves beneath the DMS with a velocity of 60 mph in the direction of the wind. The wind speed is 90 mph. Wind direction is from left to right.

The effect of the presence of the truck has even a smaller effect on the resultant streamwise force on the DMS. Similar to the cases with no truck, the presence of the truss results in a small increase of the resultant streamwise force on the DMS (e.g., compare results for cases G and E or for cases H and F in Table 2). Consistent with the results for the streamwise force, the vertical force induced by the inclination of the frontal face of the DMS is also close in all the simulations.

### 3.4. Effect of the passage of a truck under the DMS cabinet for no wind conditions

To isolate the effects of passage of a truck under a DMS cabinet the first field testing was conducted on a day when there was little or no wind. We made an attempt to simulate similar conditions using CFD.

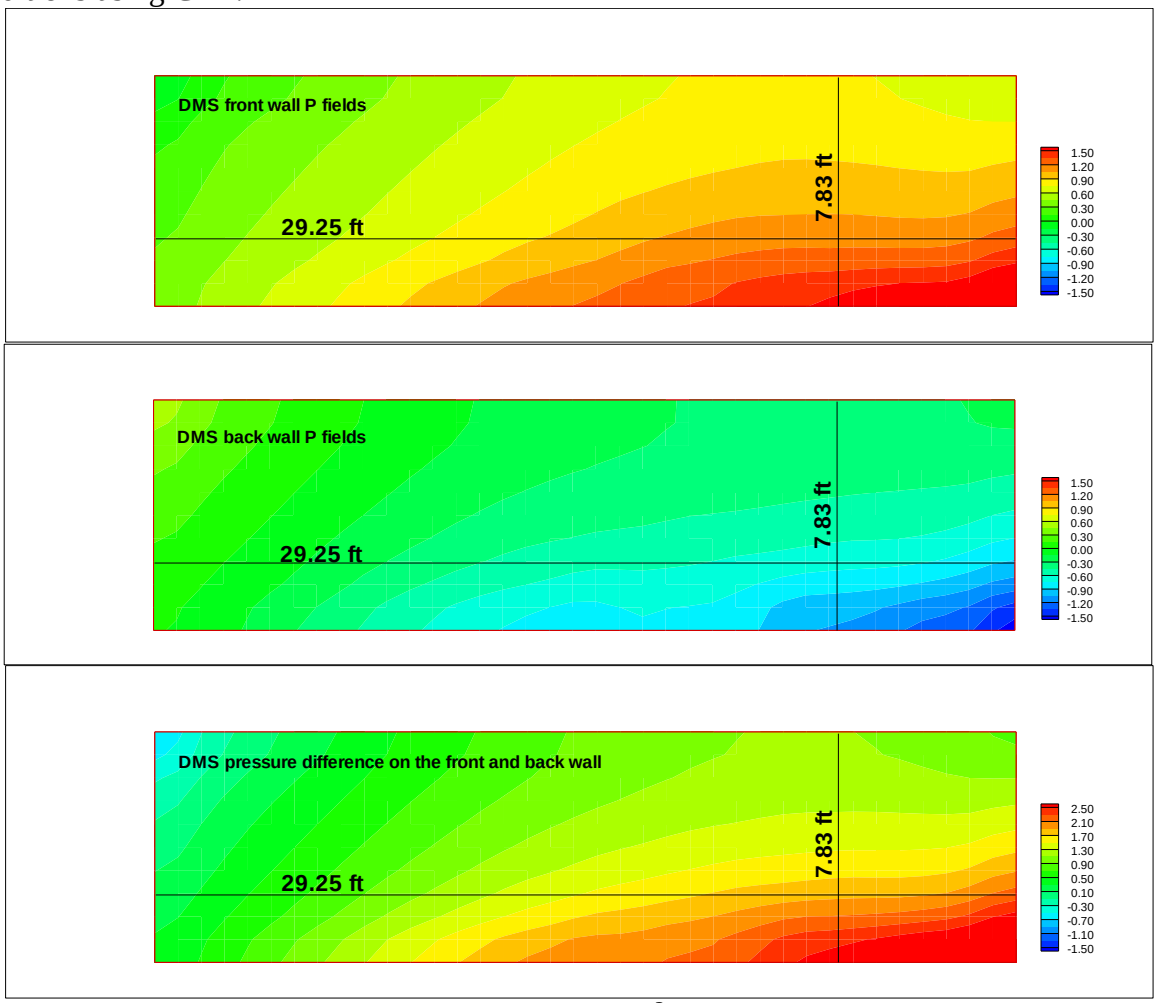


Fig. 18 Non-dimensional pressure distributions, $p/\rho U^2*1000$, on the front and back faces of the DMS cabinet for the case of a 'very long' truck and no wind. Last frame shows the distribution of the non-dimensional pressure difference between the two faces, $\Delta p/\rho U^2*1000$.

The velocity at the inlet was set equal to zero, while the velocity on the top and lateral faces of the truck was set equal to the truck velocity (60 mph). The computational domain and the other boundary conditions are the same as the one used in the corresponding simulations with wind described in the previous sections.

The large velocity on the top face of the truck and the associated boundary layer induce a decay of the pressure in between the top face of the truck and the bottom face of the DMS. This explains why the vertical component of the wind load on the DMS is oriented downwards (suction effect). The forces on the front and back faces of the DMS cabinet are non-

symmetrically distributed because of the relative position of the truck with respect to the axis of the DMS cabinet.

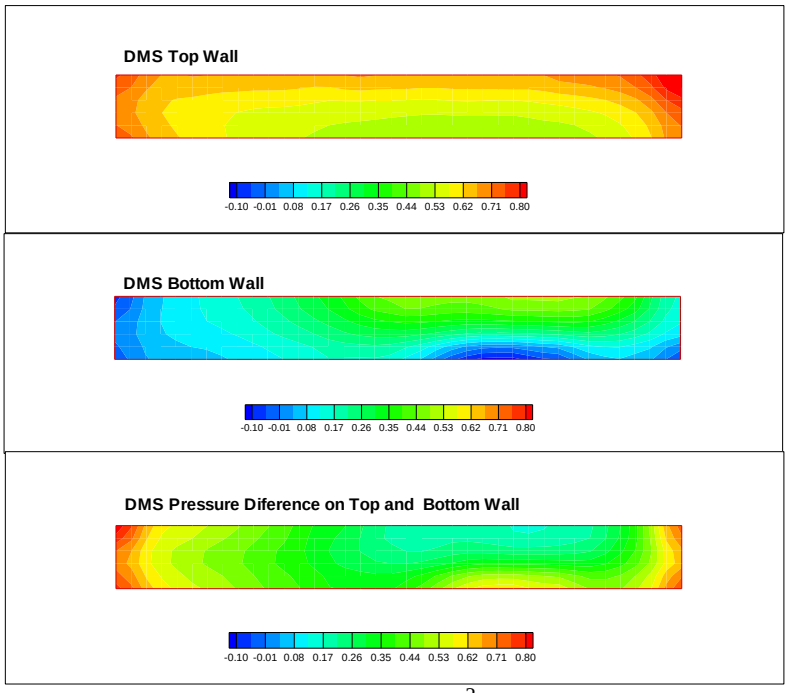


Fig. 19 Non-dimensional pressure distributions, $p/\rho U^2*1000$, on the bottom and top faces of the DMS cabinet for the case of a 'very long' truck and no wind. Last frame shows the distribution of the non-dimensional pressure difference between the two faces, $\Delta p/\rho U^2*1000$.

Table 3 Mean pressure difference on opposite faces and pressure force components induced by the truck on the DMS cabinet for the simulation with no wind and a long truck passing with a velocity of 60 mph beneath the DMS cabinet

| **Direction** | **Nondimensional average mean pressure on the faces of DMS** | | **Mean ΔP (non dimensional)** | **Mean ΔP (psf)** | **Force (pound-force)** |
|---|---|---|---|---|---|
| streamwise | Front<br>7.92e-4 | Back<br>-3.62e-4 | 1.155e-3 | 48.72e-3 | 11.16 |
| Lateral | Left<br>4.66e-4 | Right<br>1.68e-4 | 3.058e-4 | 13.00e-3 | 0.356<br>A=27.362ft$^2$ |
| Vertical | Top<br>-6.02e-4 | Bottom<br>-2.02e-4 | -3.998e-4 | -16.8e-3 | -1.83<br>A=108.94 ft$^2$ |

Figure 18 shows the pressure distributions on the front and back faces of the DMS cabinet and the distribution of the pressure difference on the two faces which is then used to calculate the resultant wind load force in the streamwise direction. Figure 19 shows the pressure distributions on the bottom and top faces of the DMS cabinet and the distribution of the pressure difference on the two faces. The resultant mean pressure difference and pressure force (pound-force units) in the streamwise, lateral and vertical directions are given in Table 3. Table 3 also gives the area of

the lateral faces and top/bottom faces of the DMS cabinet that were used to calculate the lateral and vertical components of the pressure force.

It should be noted that the pressure difference in the three directions given in Table 3 is an average value over the corresponding faces of the DMS. So, a direct comparison of the mean $\Delta P$ given in Table 3 with a value obtained as the difference of the measured pressure value at two points situated at the same location on the two opposite faces of the DMS cabinet is not always straightforward, given the large variation of the values of the pressure with location on the faces of the DMS cabinet (e.g., see Figs. 18 and 19). A comparison with the field observation values obtained from field tests conducted at the Euclid site suggests $\Delta P \sim 0.0003$ psi in the streamwise direction based on two point measurements, which corresponds to $\Delta P = 45e\text{-}3$ psf. The mean value predicted by the simulation (Table 3) is $\Delta P = 48e\text{-}3$ psf which given the simplifying assumptions used in the simulations with a truck can be considered as excellent agreement.

### 3.5. Effect of the passage of a truck under the DMS cabinet for low wind conditions corresponding to field experiment

An additional simulation was performed for low wind conditions. As in case D the speed of the truck underneath the DMS was equal to 60 mph. The value of the wind speed was chosen as the average value of the wind during the time measurements of the pressure were performed. This value was close to 5 mph. The value of the streamwise force was 27.8 pound-force (Table 4) which is consistent with the value predicted for a wind velocity of 90 mph (~7,000 pound-force) if one assumes that the force is proportional to the square of the wind velocity (quadratic regime). In fact, present CFD results show this value is slightly larger than the one deduced assuming the force is proportional to the square of the wind velocity at all Reynolds numbers.

Table 4 Mean pressure difference on opposite faces and pressure force components induced by the truck on the DMS cabinet for the simulation with 5 mph wind and a long truck passing with a velocity of 60 mph beneath the DMS cabinet

| **Direction** | **Nondimensional average mean pressure on the faces of DMS** | | **Mean $\Delta P$ (non dimensional)** | **Mean $\Delta P$ (Psf)** | **Force (Pound-force)** |
|---|---|---|---|---|---|
| streamwise | Front<br>0.973 | Back<br>-0.031 | 0.942 | 0.122 | 27.83 |
| Lateral | Left<br>-0.199 | Right<br>0.218 | 0.019 | 0.24e-2 | 0.067<br>A=27.362ft$^2$ |
| Vertical | Top<br>0.207 | Bottom<br>-0.243 | -0.036 | -0.9e-2 | -0.19<br>A=108.94 ft$^2$ |

Meanwhile the average vertical force on the DMS cabinet predicted by the numerical simulation was only 0.009 psf. This value is much smaller than the predicted point value obtained in the field experiment that was situated between 0.5 psf and 1.0 psf. However, the distribution of the pressure on the top and bottom faces of the DMS cabinet is very nonuniform. If one selects a value corresponding to the region where the maximum vertical pressure differential was recorded, the value of the vertical force is around 10-20 times larger than the mean value. Still

this value (~0.1-0.2 psf) is smaller than the predicted values. Several factors may account for this difference. One is the accuracy of the pressure measurements. The other is of course the simplifying assumptions in our CFD simulation that assumes a very long truck beneath the DMS cabinet and does not directly calculate the unsteady dynamics associated with the passage of a truck of finite length. As will be discussed later, structural simulations performed with the (larger) vertical force estimated from the field experiments will show that the deformations of the truss are very small and that the passage of the truck is most probably not the main cause for the cracks that develop over time on the trusses on which the DMS cabinets are mounted.

## 4. Structural analysis based on finite element simulations

### 4.1. Constant temperature analysis

The hypothesis of the wind study was that vertical air pressure from trucks passing beneath the DMS cabinet was causing unwanted and excessive vibrations to the supporting truss structure. Because of the DMS's large bottom face these pressures could now be transferred unlike the traditional flat aluminum signs that didn't have enough surface area to accept an upward pressure. Another contributing factor to the study was the DMS's weight. A typical aluminum sign weighs roughly 200 pounds depending on size while the DMS cabinet weighs about 4,000 pounds.

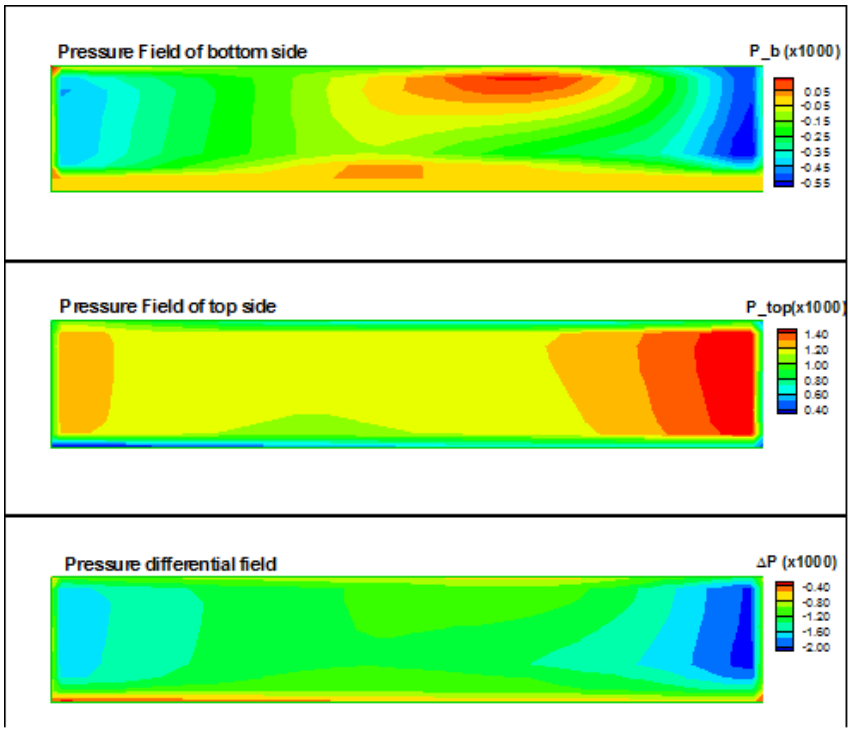


Fig. 20 Pressure field predicted on the DMS cabinet by the CFD simulation discussed in section 3.5

The approach to finding the structural response was to model the structure in a finite element program taking into consideration the pressure data gathered from the field and from CFD simulations. The CFD simulation discussed in section 3.5 (Table 4) found the total vertical

pressure to be around 0.1 psf. This was an average difference taken across the entire top and bottom of the DMS cabinet (Fig. 20).

The next step was to verify the CFD results with the field data to get an accurate description of the forces involved. Iowa State University was responsible for collecting the pressure data. Four sites were chosen for testing, the site that pertained to this study was the Kellogg truss across Interstate 80. The Kellogg truss is an all-steel structure with the main bridge being completely horizontal. The most informational data was taken at Kellogg because of its placement of pressure sensors above and below the DMS cabinet.

A total of 10 cases were captured with varying results. The interstate was not being controlled and many of the cases involved multiple trucks that had a lesser effect on the pressure than a single semi. The trials gathered could be narrowed to 4 instances when a single truck passed underneath the DMS cabinet. Figure 21 shows a plot of the pressure on each of these runs.

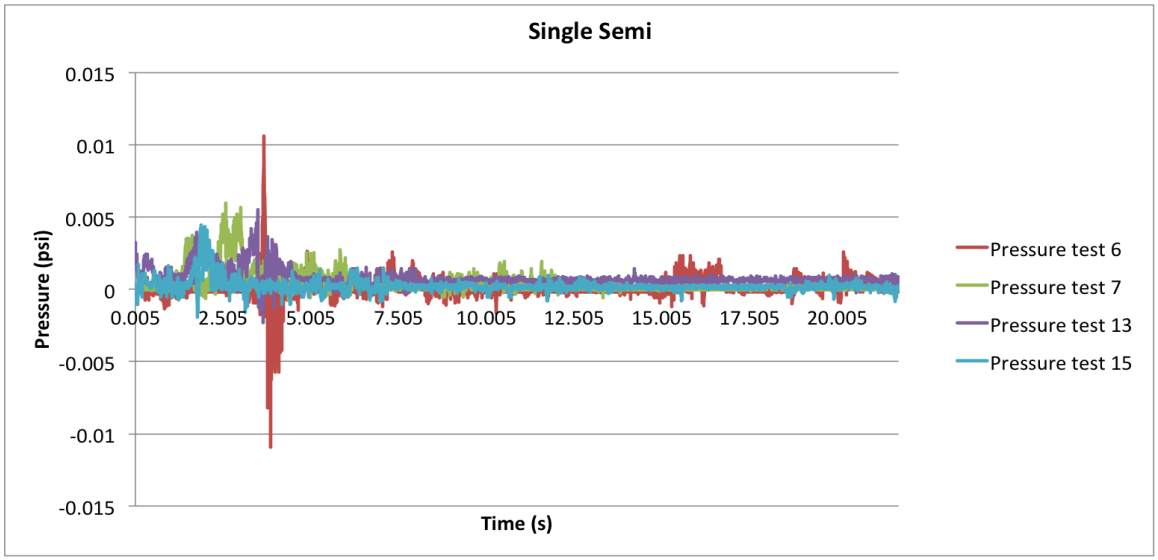


Fig. 21 Pressure data collected as part of the field experiment

As it can be seen the maximum pressure values vary from 0.004 to 0.012 psi (0.58 to 1.73 psf). This data matches data gathered from Florida State DOT that gave an average pressure of 1.0 psf or 0.007 psi. The discrepancy that is seen between the field and CFD is most likely caused by two factors. First, the CFD is a steady state simulation that captures the effects of long duration pressures well, but because the vertical pressure is an impact loading it cannot capture the full effect of the boundary layer that is shedding from the front of the truck. The other discrepancy may come from the fact that the CFD is averaging the upper and lower pressures across the entire DMS cabinet, whereas the pressure data from the field is taking a point value that may be much higher at one point on the board compared to another. This effect can be seen in Fig. 21 where the pressures vary dramatically from one run to another because of where the truck passed under the sensor.

ANSYS was used for the structural simulation of modal frequencies and response. Even though the structures are labeled trusses they do have the ability to carry moments because each member

of the structure has fully welded connections. For this reason PIPE288 elements were chosen for the simplicity and moment carrying capacity.

Table 5 List of each component's dimensions and material properties.

| **Material Properties** | **O.D.(in)** | **thicknesss(in)** | **material** |
|---|---|---|---|
| Truss web members | 3.5 | 0.216 | A36 steel |
| Truss chord members | 5.56 | 0.375 | A36 steel |
| Main supports | 10.8 | 0.5 | A36 steel |
| | | | |
| | **E (psi)** | **Poisson's ratio v** | **P (lb/in$^3$)** |
| Steel | 29000000 | 0.32 | 0.008875 |
| | | | |
| Element types | Pipe 288 | Shell 181 | |

Modeling the DMS cabinet is a challenge because it adds both mass and stiffness to the structure. To incorporate these two variables shell elements with thickness were used. The DMS cabinet is fairly large so the mass was distributed evenly over the entire board. Without fully implementing the entire casing and internal components of the DMS cabinet an estimation of the stiffness had to be made.

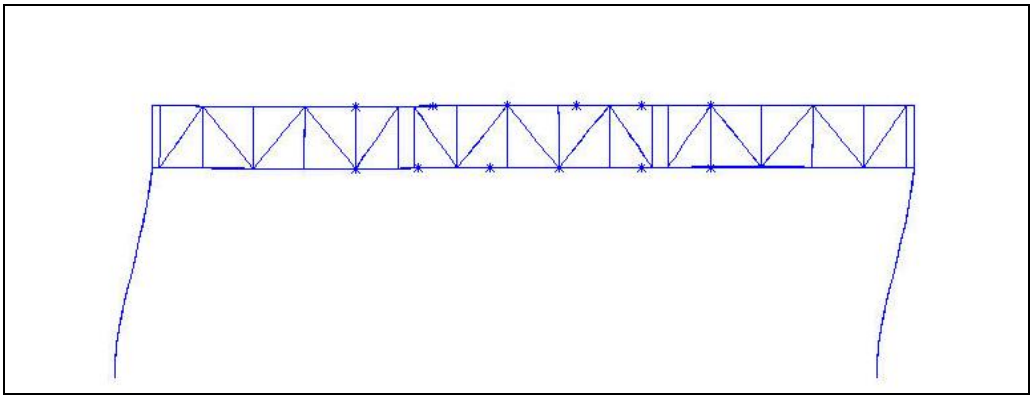

Fig. 22 Truss deformations for the case where DMS cabinet was modeled as point mass units that where evenly distributed where the DMS cabinet attaches to the truss, first frequency

To estimate the added stiffness an upper and lower range had to be established. The material of the DMS box is aluminum so an upper limit to the stiffness would be if the entire box were modeled as an aluminum block. For a lower limit the DMS cabinet was modeled as point mass units that were evenly distributed where the DMS cabinet attaches to the truss (Fig. 22). The DMS cabinet resembles a giant hollow box so a third analysis was done changing the modulus of elasticity of the box to 1/10 that of aluminum. The reason for this is that a 1 inch box of aluminum has roughly 1/10 of the moment of inertia in the strong direction as a solid 48" x 94" box. The components and materials of the truss elements are listed in Table 5.

$$I_{Solid} = \frac{1}{12} b * h^3$$
$$I_{Box} = I_{Solid} - \frac{1}{12}(b-2) * (h-2)^3 \quad (26)$$

$$\frac{I_{Box}}{I_{Solid}} \approx 0.1 \ (h = 94, b = 48)$$

Finally a fourth analysis was done with one inch thick aluminum shell elements completing a six sided box. Although this is the most complex of the structures it closely resembles the DMS (Fig. 23). It should be noted that the green arrows are located is where U-bolts are located. The U-bolts are being represented by coupling the degrees of freedom at those nodes.

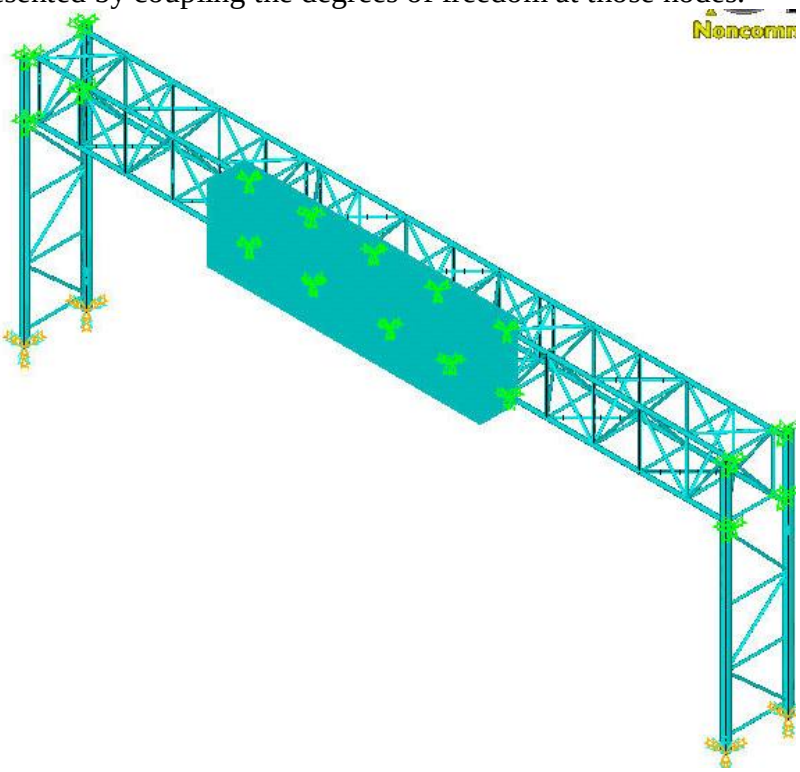

Fig. 23 Complete Kellogg Model with boundary conditions

Table 6 Modal Frequencies for Kellogg truss

| | Only mass | 1" Box | 1/10 E | Full aluminum bar |
|---|---|---|---|---|
| Mode 1 | 0.7922 | 0.7912 | 0.7914 | 0.7916 |
| Mode 2 | 1.357 | 1.505 | 1.524 | 1.551 |
| Mode 3 | 2.034 | 2.297 | 2.438 | 2.612 |
| Mode 4 | 3.256 | 3.322 | 3.317 | 3.372 |

Table 6 gives the result of each analysis through the first 4 modes. The stiffness of the DMS will contribute to the shape and deformation of the truss. However its effect on the vibration modes depends on the shapes of the vibration modes. Since the first mode is a sidesway mode the DMS does not have a large impact on the first mode of the truss.

For the purposes of the harmonic analysis it is not necessary to include the stiffness of the DMS cabinet. However, as will be shown later an equivalent stiffness is needed in place of the DMS cabinet.

To finalize the model, damping needed to be added for a full transient analysis, Rayleigh damping was used. Thus, it was important to find the correct mode that the vertical pressure was exciting. Running an undamped transient analysis showed that the vertical pressure excited the second mode in the vertical direction. A conservative estimate for the steel structure damping ratio was is given as 2-3%. The lower value was chosen to give the best chance for a resonant response. The ratio can then be used in conjunction with the frequency of 1.505 to find the $\alpha$ and $\beta$ values.

The goal of the analysis was to mimic a worst case scenario for vertical loading. The loading was chosen to duplicate the patterns that were seen in Fig. 21. It was then applied at the modal frequency that would induce resonance.

The results of the transient analysis can be seen in Fig. 24. This plot is a snapshot of the truss after the first impact loading occurs when the stress in the bars are at a maximum. Even with the worst loading case the results are very clear. The vertical loading does not have a significant impact on the structural integrity of the truss, and at a maximum value of 39 psi the stress is not a concern for fatigue failure.

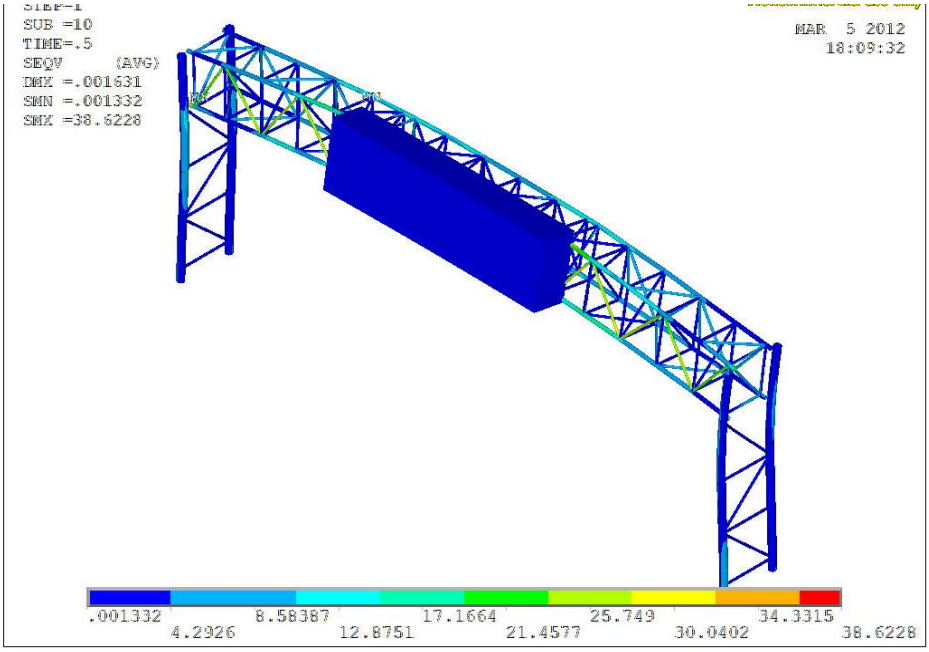

Fig. 24 Maximum transient stress for Kellogg truss

It should be noted that along with the vertical loading, a streamwise loading case was incorporated into the model and produced interesting results. Normally the trusses are loaded with lightweight aluminum signs, but because of the DMS's added mass a streamwise force induces a torsional mode shape that is not seen with the lighter signs. Future analysis can be considered to simulate streamwise resonant forces. For this to be a contributing factor a long term study of streamwise pressure loading would need to be done for input verification.

### 4.2. Thermal results

For the thermal test a linear thermal expansion model was used at a value of 3 E-7 m/°C. The reference temperature for the test was set at an arbitrary value of 15.56° C (60° F). The temperature was then increased to a value of 37.78° C (100° F) to give the following results in plots below. These values closely mimic the temperature ranges seen in the long term Ames testing so the computational results should correspond to the data as well.

The largest stress points are directly behind the sign (Fig. 25) and at the first rung of the main supports (Fig. 26). These values range from 500 psi in tension to 6000 psi in compression.

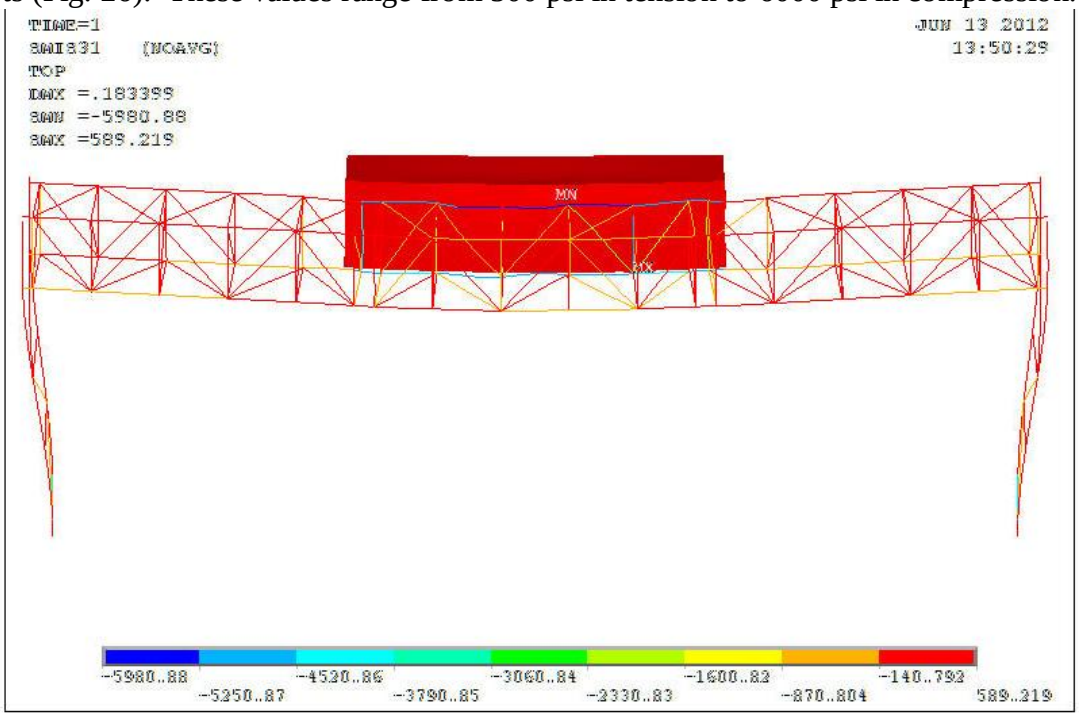


Fig. 25 Axial stress due to thermal expansion (back view)

Fig. 26 Axial stress due to thermal expansion (side view)

Note in this analysis all members were assumed to undergo the same temperature change. In the field some members could be shaded from the sun and may experience different temperature change. However incorporating this in the model will require detailed field measurement of temperature in each member.

# 5. Short-term monitoring: Field study and data analysis

## 5.1. General description of instrumentation

In total there were five DMS/sign trusses instrumented and evaluated for this project. For all five, short-term testing of each truss was conducted; in addition, long-term testing of the Ames DMS truss was also completed. Both the short-term and long-term testing scenarios had the following objectives: evaluate the truss performance under a) ambient wind conditions and b) ambient truck induced wind gusts. In general, each truss was instrumented with all or some combination of the following monitoring equipment: strain gages, accelerometers, anemometer, and pressure sensors. However, each of the five trusses had slightly different instrumentation configurations which are detailed below. Table 7 shows some important information about each of the truss tests.

Table 7. General Test Information

| | Ames | Kellogg | Euclid | Ankeny DMS | Ankeny Sign |
|---|---|---|---|---|---|
| Date of Test | Summer 2011 | 10-6-2010 | 8-5-2010 | 11-15-2011 | 11-15-2011 |
| Load Types | Uncontrolled | Truck | Truck | Truck | Truck |
| Truss Span | 70 ft | 75 ft | 69 ft | 85 ft | 85 ft |
| Truss Material | Aluminum | Steel | Aluminum | Aluminum | Aluminum |
| Connection Type | Tube-to-tube | Gusset Plate | Tube-to-tube | Tube-to-tube | Tube-to-tube |

Bridge Diagnostic Inc. (BDI) intelliducer strain gages were most frequently used for recording strains in the truss members for the short term tests. For locations where strain gages were attached to larger members of the truss, i.e. the top and bottom chords and the truss support columns, the gages were glued on using the standard attachment tabs for the gages as shown in Fig. 27. In areas where the gages were to be attached to smaller members of the trusses, i.e. vertical, diagonal, and secondary horizontal members of the truss, the gages were attached with pipe clamp jigs specifically designed for the diameter of that member as shown in Fig. 28. For the long-term testing, both Hitec glue-on strain gages and Geokon vibrating wire (VW) strain gages were utilized instead of the BDI strain gages.

Fig. 27 View of a strain gage attached on a large member of the truss

Fig. 28 View of a strain gage attached on a small member of the truss

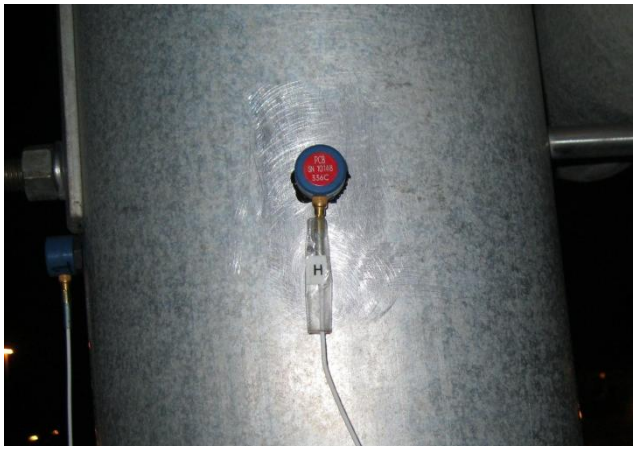

Fig. 29 View of an accelerometer attached to a truss member

Accelerometers used for this testing included PCB 3741B1210G for the Ames DMS truss, and PCB 336C accelerometers for all other trusses. The testing configuration for all trusses included a minimum of three accelerometers mounted on the truss and/or truss support columns such that accelerations in the direction parallel and perpendicular to traffic could be measured. The accelerometers were typically attached directly to the truss and/or column members with adhesive as shown in Fig. 29.

In addition to the typical structural monitoring instrumentation described above, pressure sensors and an anemometer were installed on several of the trusses to evaluate the significance of ambient and traffic induced wind and its effects on the behavior of the trusses. Omega pressure sensors were used for this testing and, when used, were installed directly on the DMS cabinet. For the trusses equipped with an anemometer, it was located and mounted as shown in Fig. 30, underneath the DMS cabinet at mid-width except for the Ames DMS Truss which had the anemometer mounted above the DMS cabinet.

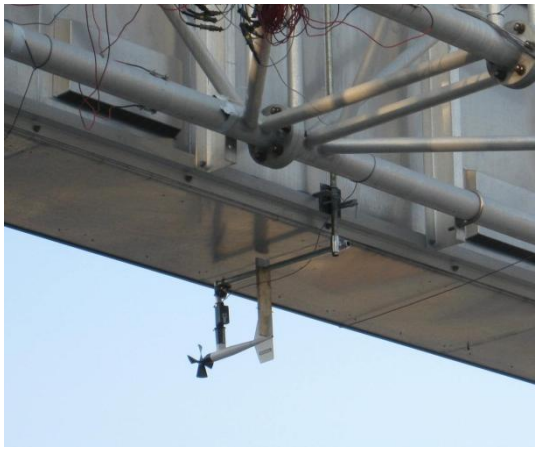

Fig. 30. View of an anemometer mounted underneath the DMS cabinet

Short-term testing for the trusses was completed using an Optim Megadac data acquisition system (DAS) and a Dell laptop computer running TCS software to provide communication between the Megadac and the sensors. In some cases, the Bridge Diagnostic Inc. (BDI) inteliducers (strain gages) were connected to the Megadac, in others they were connected to the BDI Structural Testing System (STS) for data collection. For the long term testing, the vibrating wire gages/instrumentation was connected to a Campbell Scientific CR1000 data logger and all other gages were connected to a Campbell Scientific CR9000 data logger.

### 5.2. Instrumentation plan: Ames DMS Truss

The DMS truss on northbound I-35 south of Ames, Iowa is a 70-ft span truss, consisting of two 20-ft end sections, each with four truss panels, and a 30-ft center section with six truss panels as shown in Figs. 30 and 31. Instrumentation for this truss consisted of an anemometer, six pressure sensors, four accelerometers, 12 Hitec strain gages connected to a Campbell Scientific CR9000 Datalogger, and 6 VW strain gages connected to a Campbell Scientific CR1000 Datalogger. The location of the aforementioned instrumentation is illustrated in Fig. 32 and 33.

The anemometer was mounted above the DMS cabinet facing oncoming traffic. The six pressure sensors were installed directly to the DMS cabinet, in the same transverse location as the strain gages near midspan (described below) of the truss. One pressure sensor was installed on both the top and bottom surface of the DMS cabinet, two pressure sensors were installed on the front face of the DMS cabinet at approximately 2-ft and 4-ft from the bottom of the cabinet, and the last two pressure sensors were installed on the back of the DMS cabinet in the same locations as the two on the front face.

There were two clusters of accelerometers on the truss. At midspan of the truss there were two accelerometers, one mounted horizontally (parallel to traffic flow) on the top chord, and one mounted vertically on the top chord as shown in Fig. 32 at Cross Section A. In addition, there were two accelerometers mounted near the top of the Southeast truss support column, as shown in Fig. 33. Both column accelerometers were mounted horizontally, one on the north side of the column and one on the east side of the column.

There were a total of 18 strain gages installed on the Ames DMS truss. At Cross Section B near midspan, shown in Figs. 31 and 32, 12 strain gages were installed on the chord members. Each chord member was instrumented with two Hitec strain gages and one VW strain gage. The remaining six strain gages were installed at Cross Section C and consisted of two Hitec strain gages and one VW strain gage on a diagonal in the vertical plane of the South truss and two Hitec strain gages and one VW strain gage on a diagonal in the horizontal plane of the bottom truss.

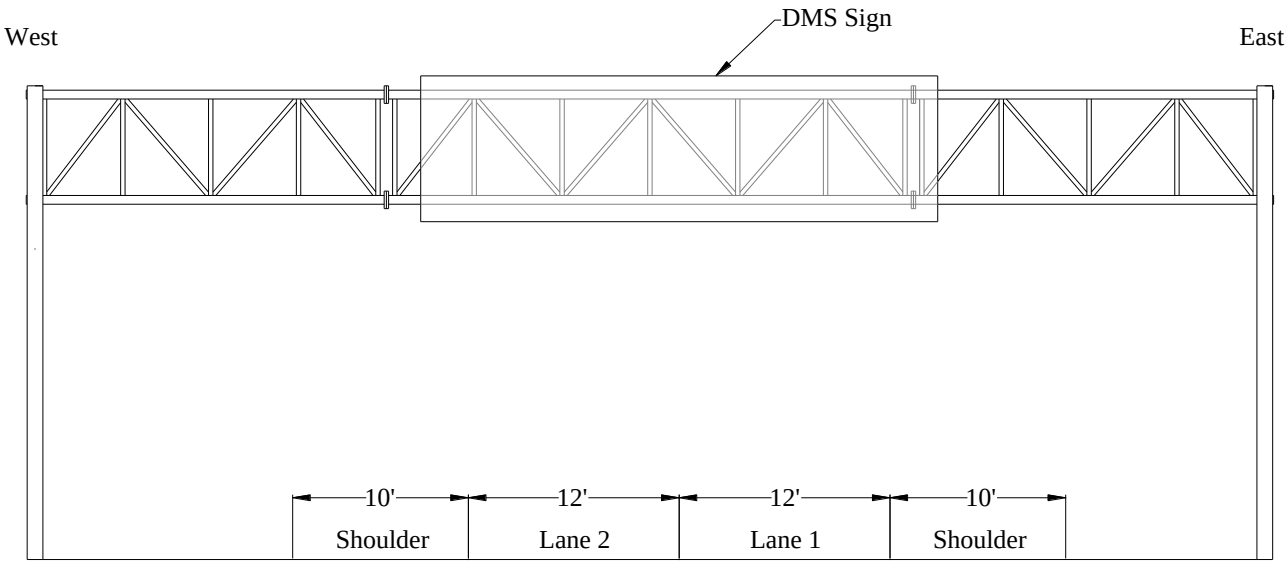


Fig. 30. Ames DMS truss lane configuration.

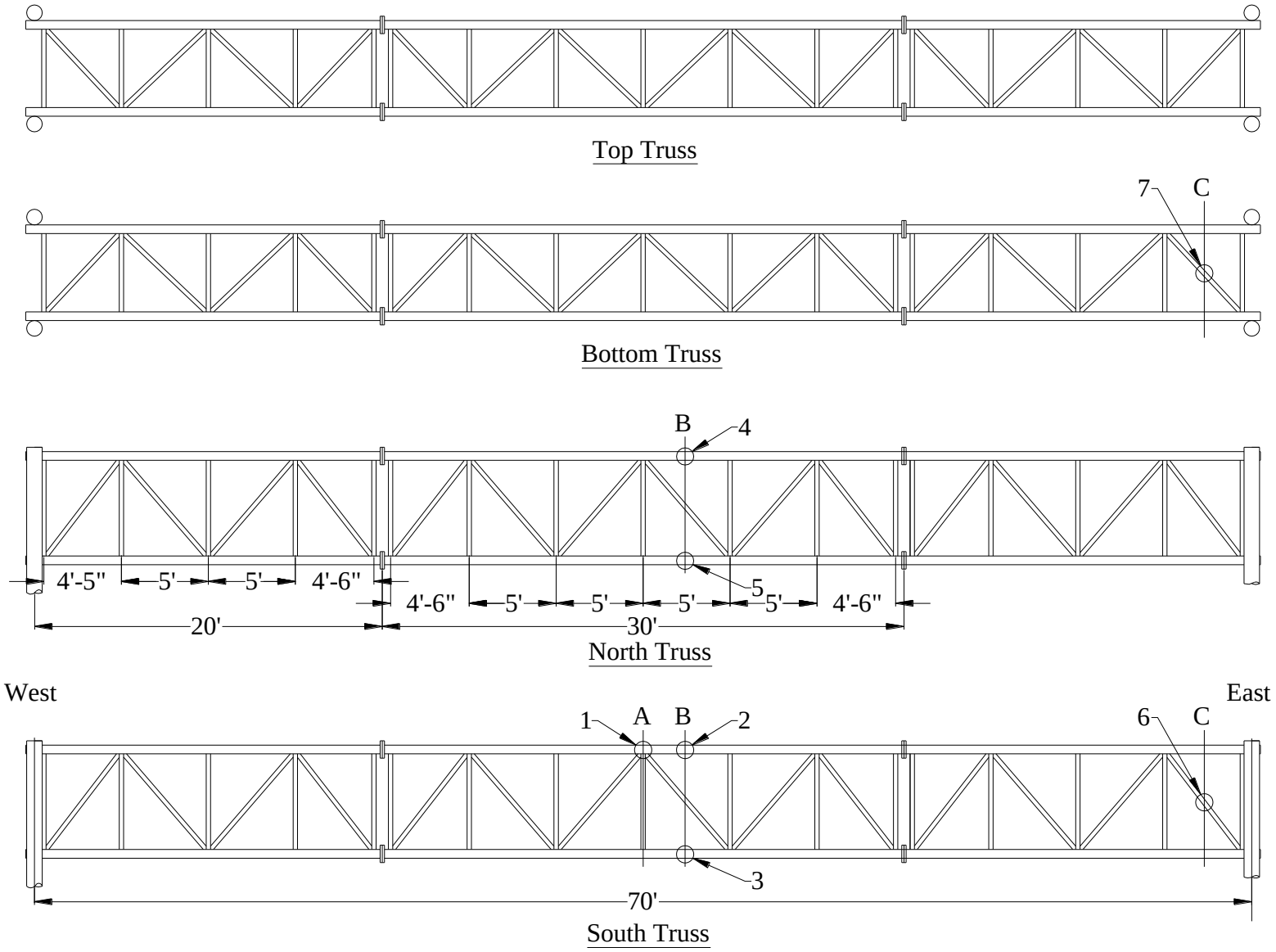


Fig. 31. Truss configuration and gage locations for Ames DMS truss.

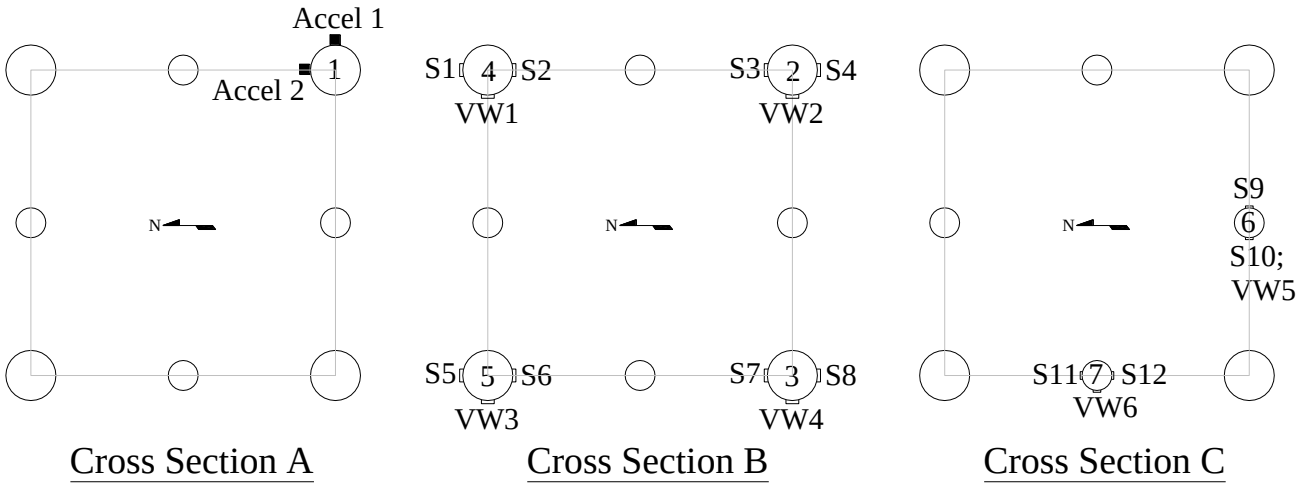


Fig. 32. Ames DMS Truss chord instrumentation configuration.

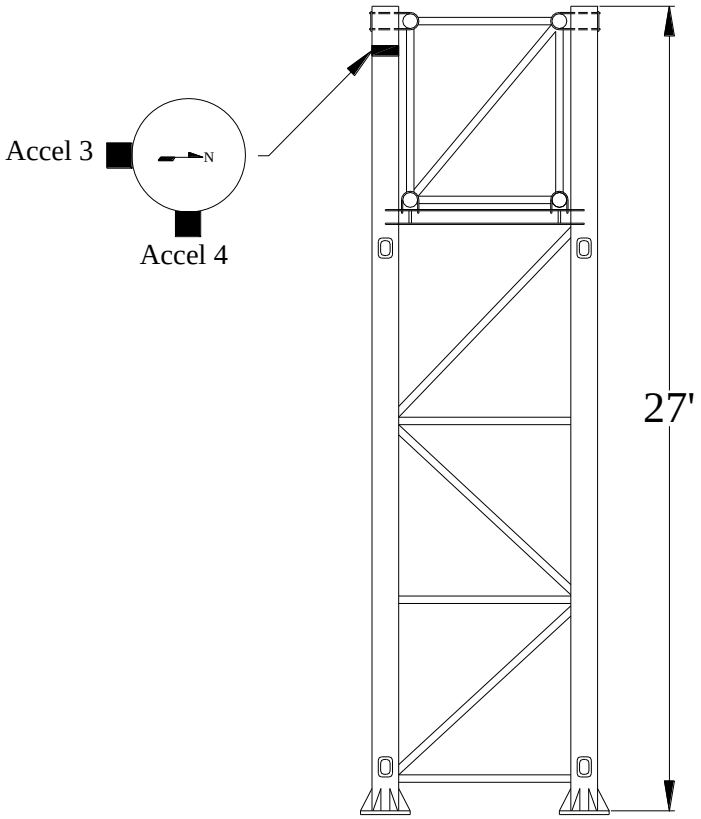


Fig. 33. Ames DMS Truss support column instrumentation configuration.

### 5.3. Instrumentation plan: Kellogg DMS Truss

The DMS truss on I-80 near Kellogg, Iowa is a 75-ft span truss, consisting of three 25-ft sections each with five truss panels as shown in Figs. 34 and 35. Instrumentation for this truss consisted of an anemometer, six pressure sensors, five accelerometers, and 28 BDI strain gages connected to the Megadac DAS. The location of the aforementioned instrumentation is illustrated in Figs. 35 through 37. The anemometer was mounted below the DMS cabinet facing oncoming traffic (see Fig. 30). Two pressure sensors were installed on the front side of the DMS cabinet at approximately 8-ft (1/3$^{rd}$ the DMS width) from the north edge, at 16-in and 47-in from the bottom edge. This configuration of pressure sensors was mirrored on the back side of the DMS, along with a fifth pressure sensor on the top of the DMS cabinet.

There were two clusters of accelerometers on the truss on which the DMS was installed. At midspan of the truss there were three accelerometers, one mounted horizontally on both the top and bottom chord, and one mounted vertically on the bottom chord as shown in Fig. 36 at Cross Section C. In addition there were two accelerometers mounted near the top of the Northwest truss support column, as shown in Fig. 37. Both column accelerometers were mounted horizontally, one on the south side of the column and one on the west side of the column.

There were a total of 28 strain gages installed on the Kellogg DMS truss, 20 of which were located on the top and bottom chord members in the truss panel immediately north of the centerline of the truss at Cross Sections A, B and C shown in Figs. 35 and 37. Both of the top chord members had three cross section instrumented with a strain gage on the east and west side of the members at each location. In addition, each of the bottom chord members had two cross sections instrumented with a strain gage on the east and west side of the members at each location. The remaining eight strain gages were installed on the northern truss support columns, four on each of the two columns located 4.5-ft from the base of the column on the north, south, east and west faces of the columns as illustrated in Fig. 36.

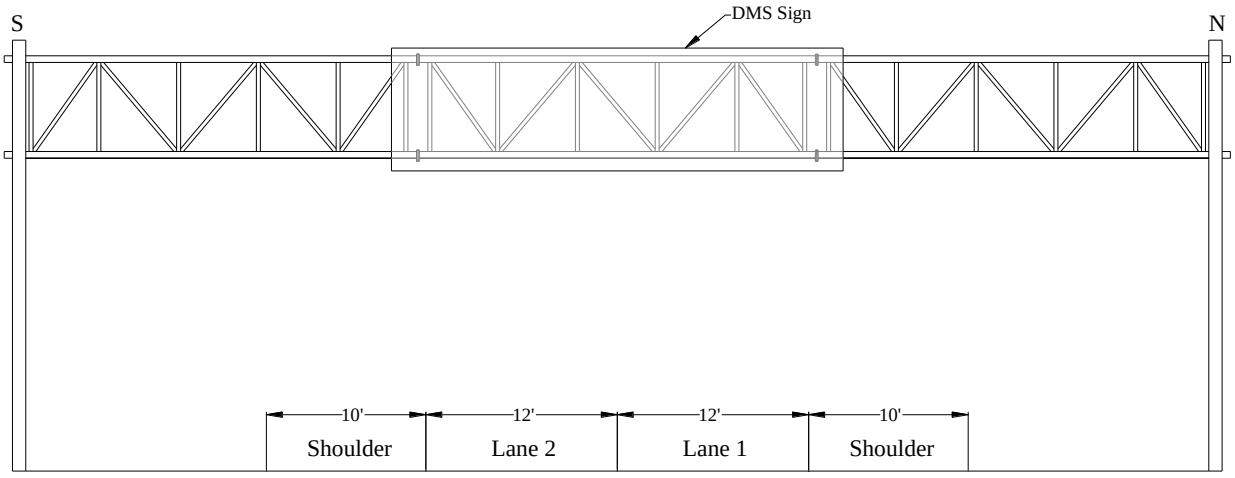


Fig. 34. Kellogg DMS truss lane configuration.

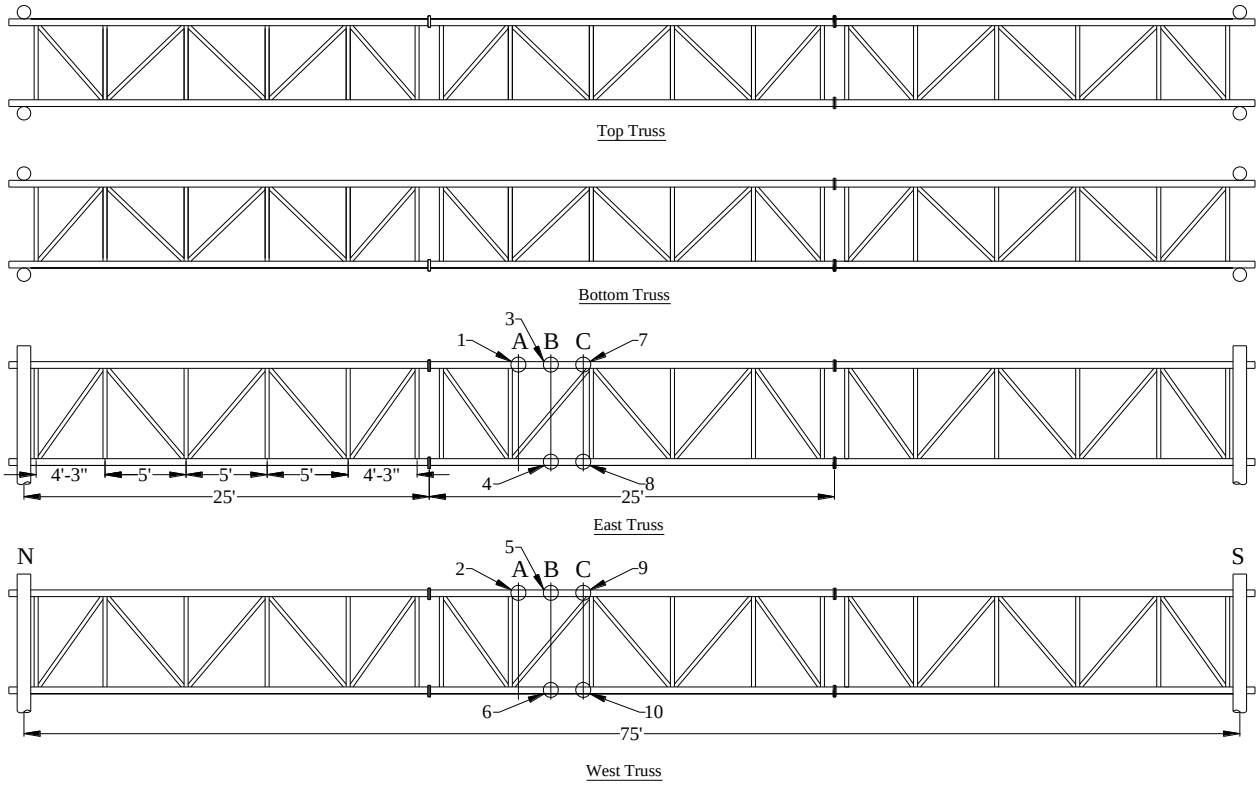


Fig. 35. Truss configuration and gage locations for Kellogg DMS truss

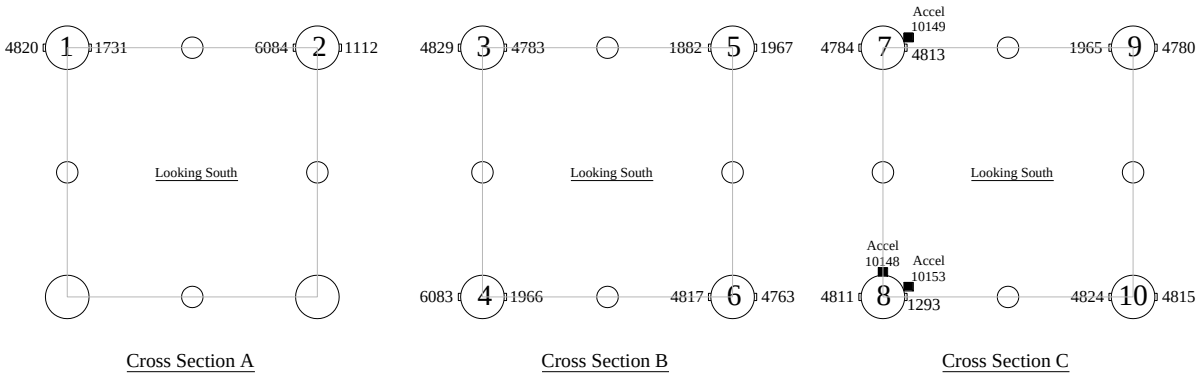


Fig. 36. Kellogg DMS Truss chord instrumentation configuration.

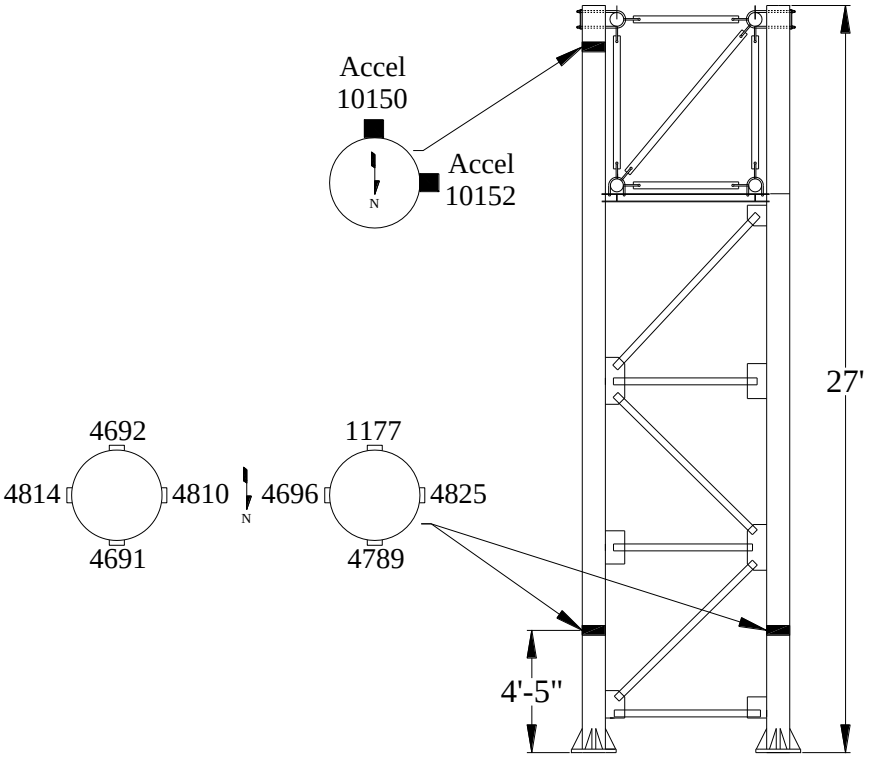


Fig. 37. Kellogg DMS Truss support column instrumentation configuration.

### 5.4. Instrumentation plan: Euclid (I-235) DMS Truss

The DMS truss on I-235 near the Euclid exit in Des Moines, Iowa is a 21-m span truss, consisting of two 10.5-m sections each with four truss panels as shown in Figs. 38 and 39. Instrumentation for this truss consisted of an anemometer, two pressure sensors, six accelerometers, and 36 BDI strain gages connected to the Megadac DAS. The location of the

aforementioned instrumentation is illustrated in Fig. 39, 40 and 41. The anemometer was mounted below the DMS cabinet facing oncoming traffic (see Fig. 30). The two pressure sensors were installed on the front face of the DMS cabinet at approximately the 1/3$^{rd}$ points of the cabinet width and at mid-height, see Figs. 39 and 42.

There were three groups of two accelerometers on the DMS truss. One pair on both the top and bottom chord at midspan of the north truss, and a third pair on the top of the northeast truss support column as shown in Figs. 40 and 41. Each of the two groups of accelerometers at midspan consisted of one accelerometer mounted horizontally and one mounted vertically; the two accelerometers mounted on the column were both mounted horizontally, one on the north side of the column and one on the east side of the column.

There were a total of 36 BDI strain gages installed on the Kellogg DMS truss, 20 of which were located on the truss and 16 on the truss support columns. Strains were recorded on the top and bottom chords as well as the diagonals in the first truss panel east of the truss midspan, Cross Section B in Fig. 39 and 40; in addition, strains were recorded on the diagonal members in the eastern most truss panel, Cross Section C in Fig. 39 and 40. As shown in Fig. 41, each column of the truss was instrumented with four strain gages, one each on the north, south, east and west faces at a height of 1.28-m and 1.08-m from the base of the East (shoulder) and West (median) columns, respectively.

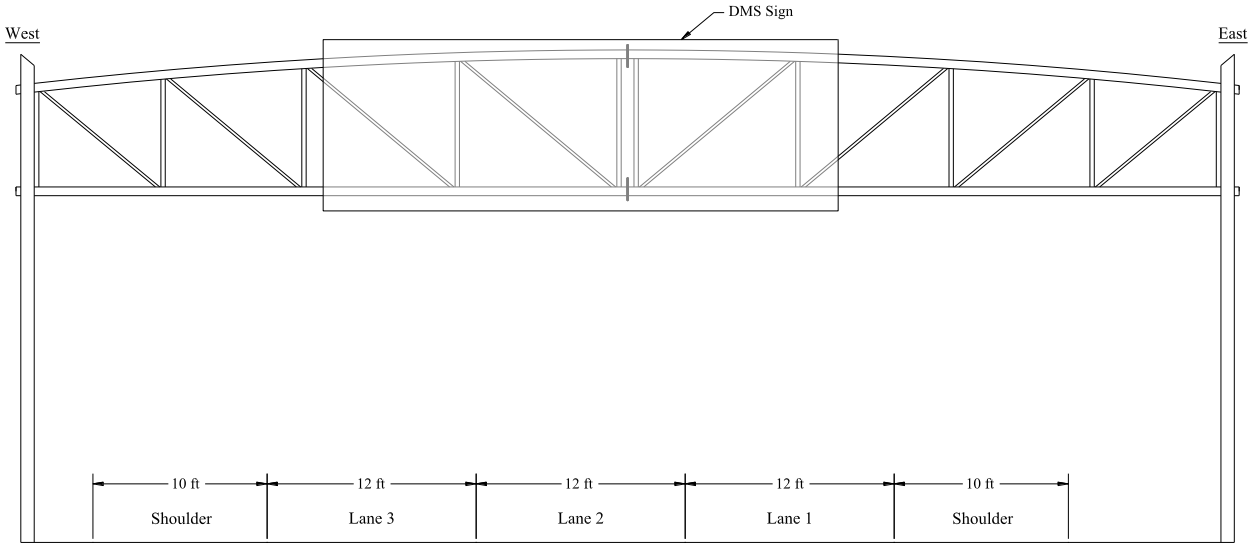


Fig. 38 Euclid (I235) DMS truss lane configuration.

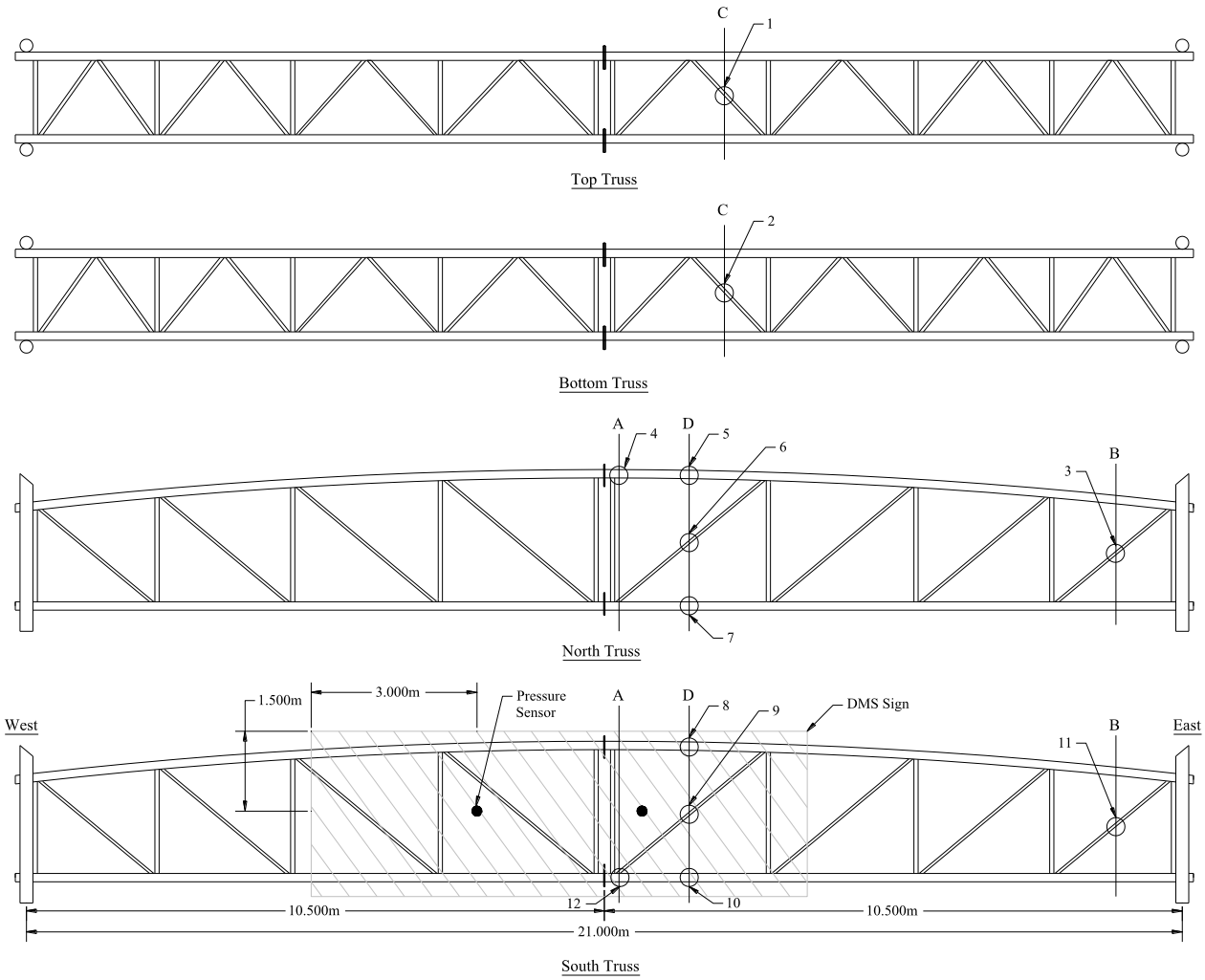


Fig. 39 Truss configuration and gage locations for Euclid (I-235) DMS truss.

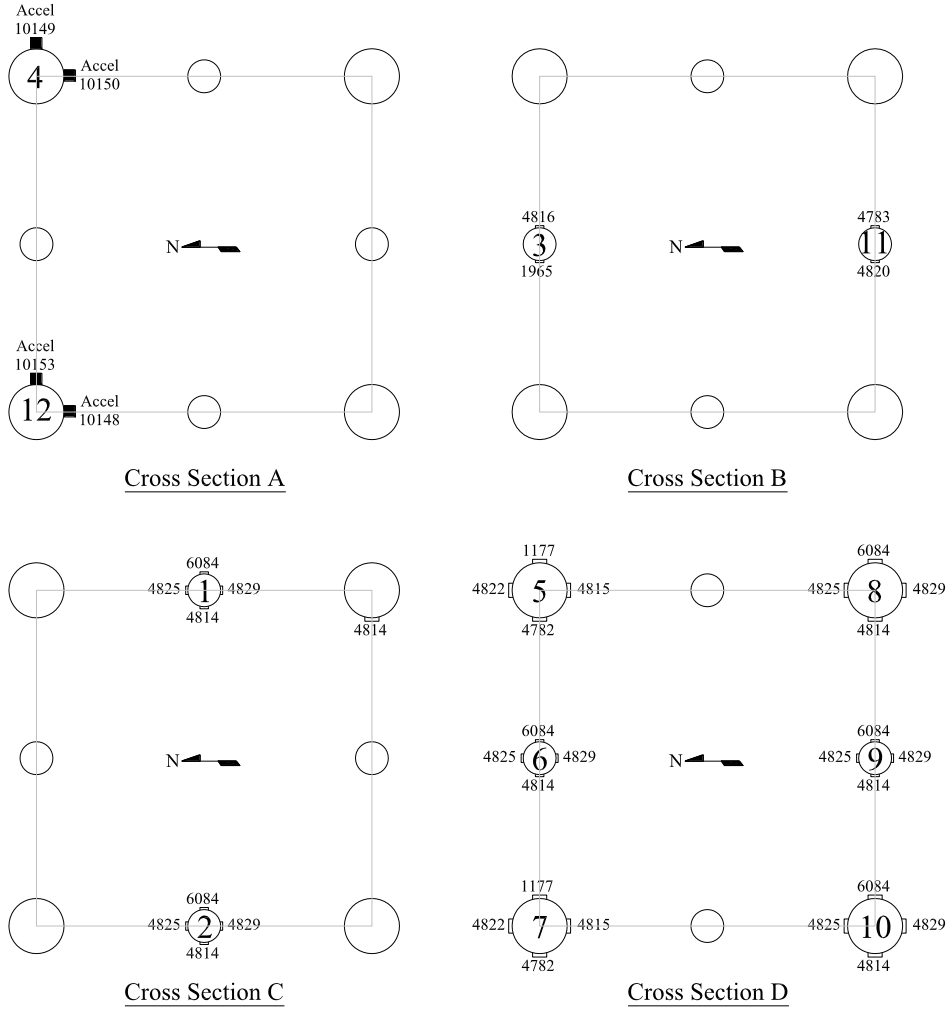


Fig. 40 Euclid (I235) DMS Truss chord and diagonal instrumentation configuration.

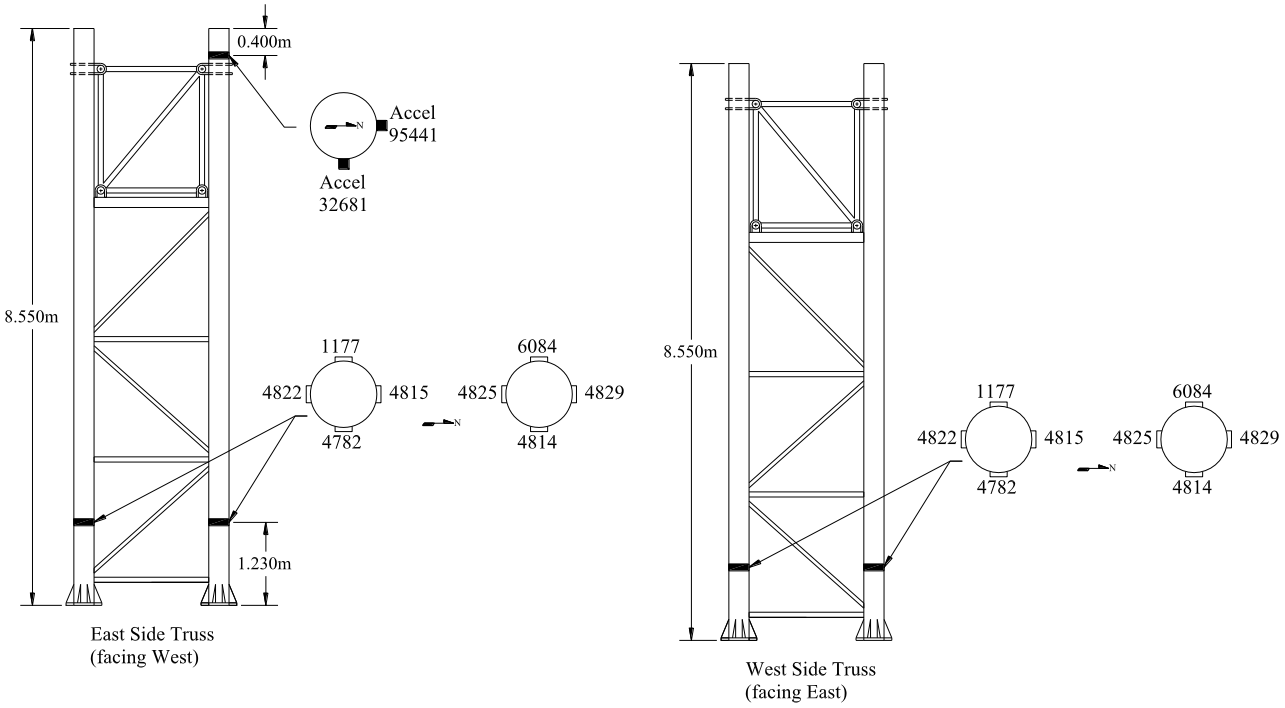


Fig. 41 Euclid (I235) DMS Truss support column instrumentation configuration.


Fig. 42 Pressure sensor locations on Euclid (I235) DMS cabinet

### 5.5. Instrumentation plan: Ankeny DMS and Sign Trusses

Both the DMS truss and the Sign truss on southbound I-35 near Ankeny, Iowa were 85-ft span trusses, consisting of two 30-ft end sections each with six truss panels and a 25-ft center section with five truss panels as shown in Figs. 43, 44 and 45. Instrumentation for both trusses consisted of four accelerometers and 24 BDI strain gages. The Megadac DAS was used for data collection on the DMS truss, and the BDI STS system was used for data collection on the Sign truss so that both trusses could be tested simultaneously. In addition, a gradient gage was implemented on the DMS truss near the west support columns. The location of the aforementioned

instrumentation for the DMS and Sign trusses were the same and are illustrated in Figs. 45, 46 and 47.

There were two sections instrumented on each truss, one truss panel immediately west of midspan of the truss (Cross Section A) and the western most truss panel (Cross Section B). Cross Section A included two accelerometers on the north truss top chord (one mounted horizontally and one mounted vertically), and four strain gages on each of the four chord members as shown in Fig. 46. Cross Section B included eight strain gages, two on each of the diagonals as shown in Fig. 47. In addition, there were two accelerometers on the southwest truss support column of each truss, which were installed horizontally, one on the east side of the column and one on the south side of the column as shown in Fig 48. The location of the gradient gage on the DMS truss is illustrated in Figs. 48 and 49.

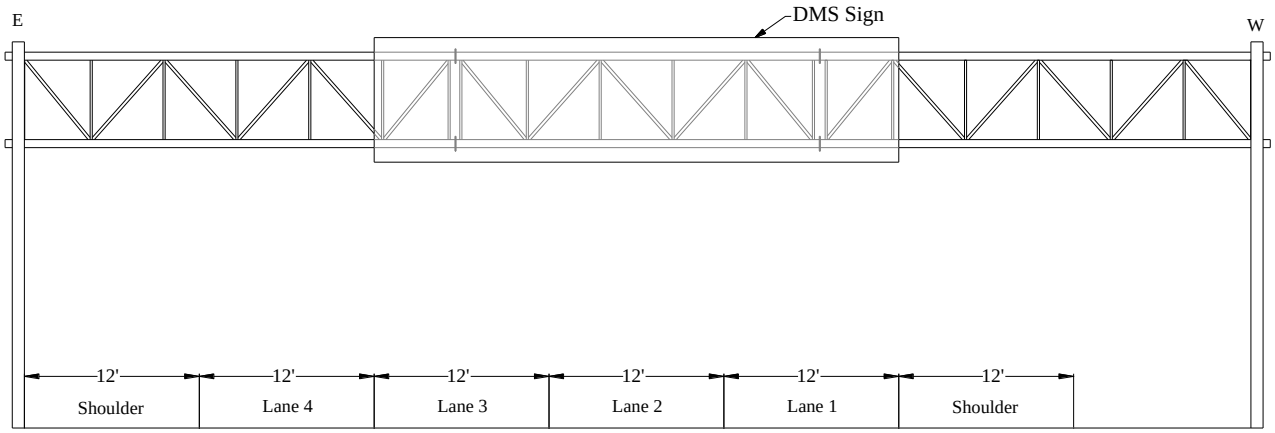


Fig. 43 Ankeny DMS truss lane configuration.

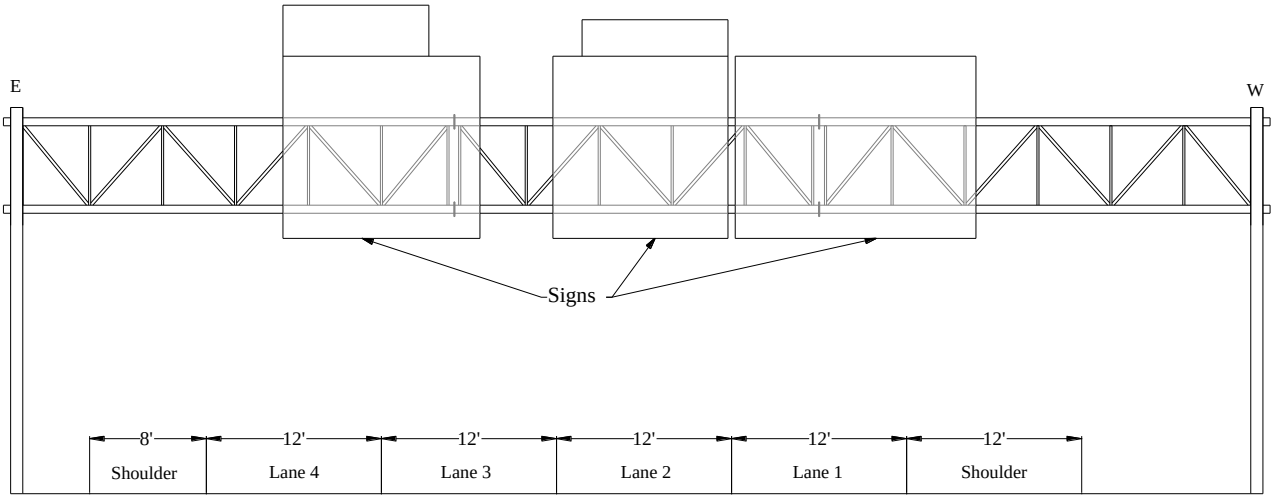


Fig. 44 Ankeny Sign truss lane configuration.

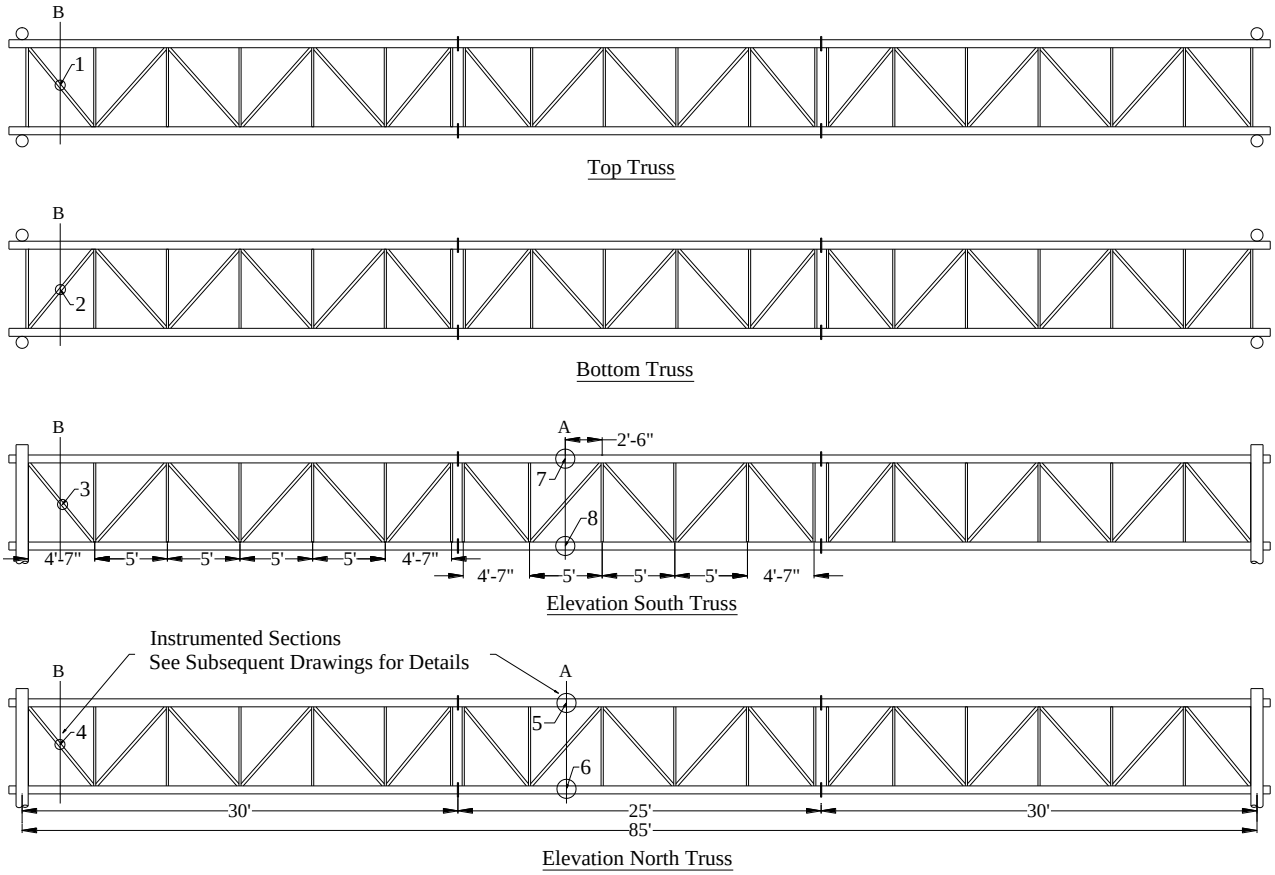


Fig. 45 Truss configuration and gage locations for Ankeny DMS and Sign trusses

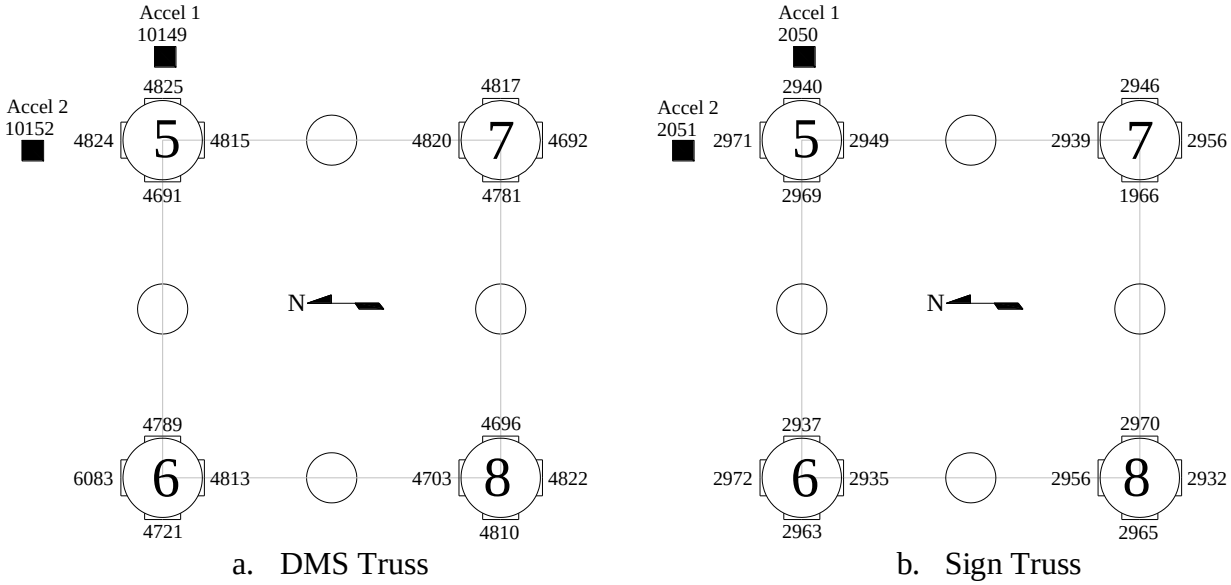


a. DMS Truss b. Sign Truss

Fig. 46 Ankeny DMS/Sign Truss instrumentation configuration at Cross Section A.

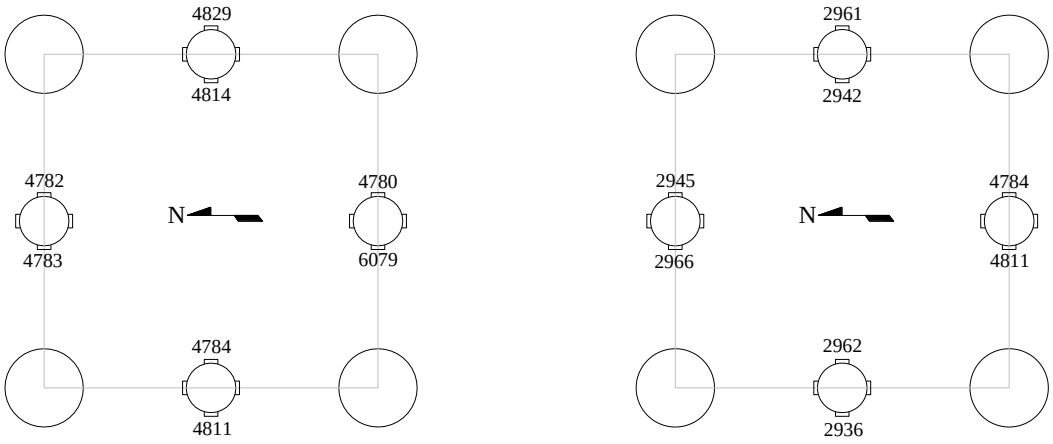


a. DMS Truss b. Sign Truss

Fig. 47 Ankeny DMS/Sign Truss instrumentation configuration at Cross Section B.

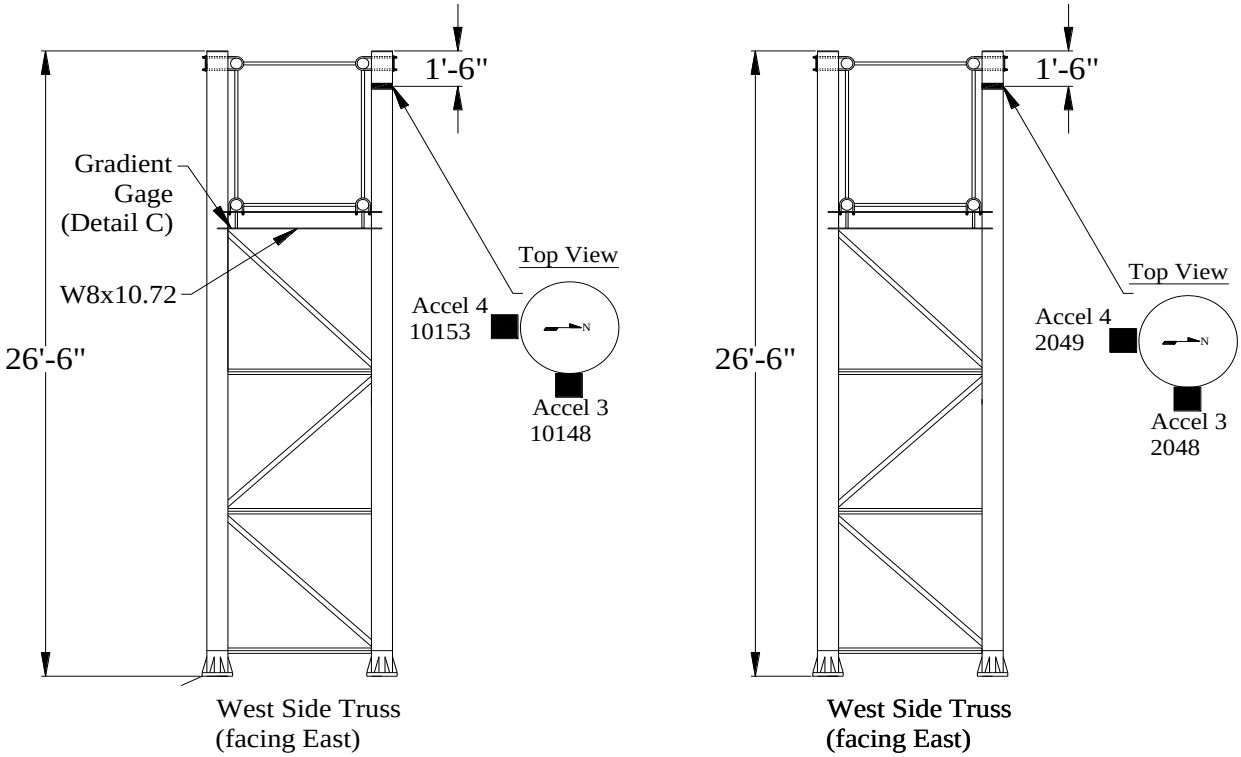


a. DMS Truss b. Sign Truss

Fig. 48 Ankeny DMS/Sign Truss instrumentation configuration on southwest support columns.

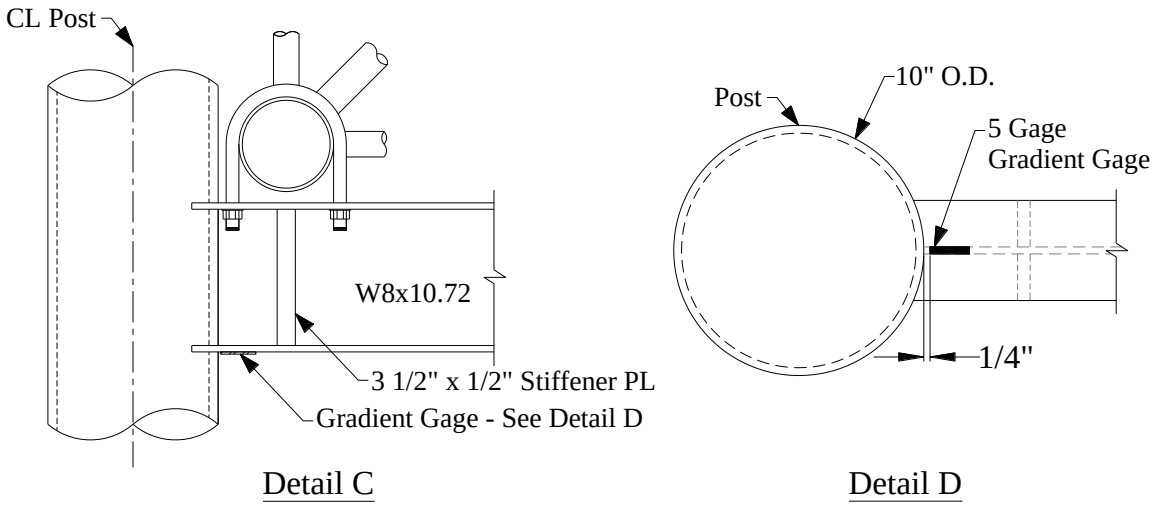


Fig. 49 Ankeny DMS Truss gradient gage configuration.

### 5.6. Data Analysis

Data were collected for each of the 5 previously-mentioned trusses. Comparison among the data sets facilitates understanding the general behavior characteristics of the trusses. Anywhere from 15 to hundreds of data files were collected. Several data files were closely analyzed because they had one or more of the following features: high wind speed, wind direction approximately perpendicular to the DMS cabinet/sign, or a worst case truck and travel lane combination creating large wind gusts. General trends are described in the following paragraphs.

Pressure sensors were installed on three DMS trusses and Table 8 summarizes the peak measured pressures. As shown, the largest pressure was 0.35 psi (50.4 psf) for the Ames truss. For the other two trusses the pressure are lower (<30 psf). Pressure on front of the DMS panel was generally slightly greater than pressure on back of the DMS panel, as shown in a sample from Ames truss below in Fig. 50. Also, pressure was greater near the top of the DMS panel than it was towards the bottom as shown in Table 8. The pressures shown in Table 8 should be considered with caution. The pressure sensors used in this work were designed to operate in a laboratory environment. Thus, the reliability of the readings (especially on the Ames truss) may be somewhat questionable.

Table 8 Pressure at Sensor Locations

| | Top | Bottom | Front Mid-Height | Back Mid-Height | Front Towards Bottom | Back Towards Bottom | East Side | West Side |
|---|---|---|---|---|---|---|---|---|
| | psf | psf | psf | psf | psf | psf | psf | Psf |
| Ames | 50.4 | 43 | 31 | 2.9 | 48.8 | 44.6 | NA | NA |
| Kellogg | 8.0 | 7.2 | 0.004 | 0.43 | 0.58 | 0.29 | NA | NA |
| Euclid | NA | NA | NA | NA | NA | NA | 0.43 | 0.43 |

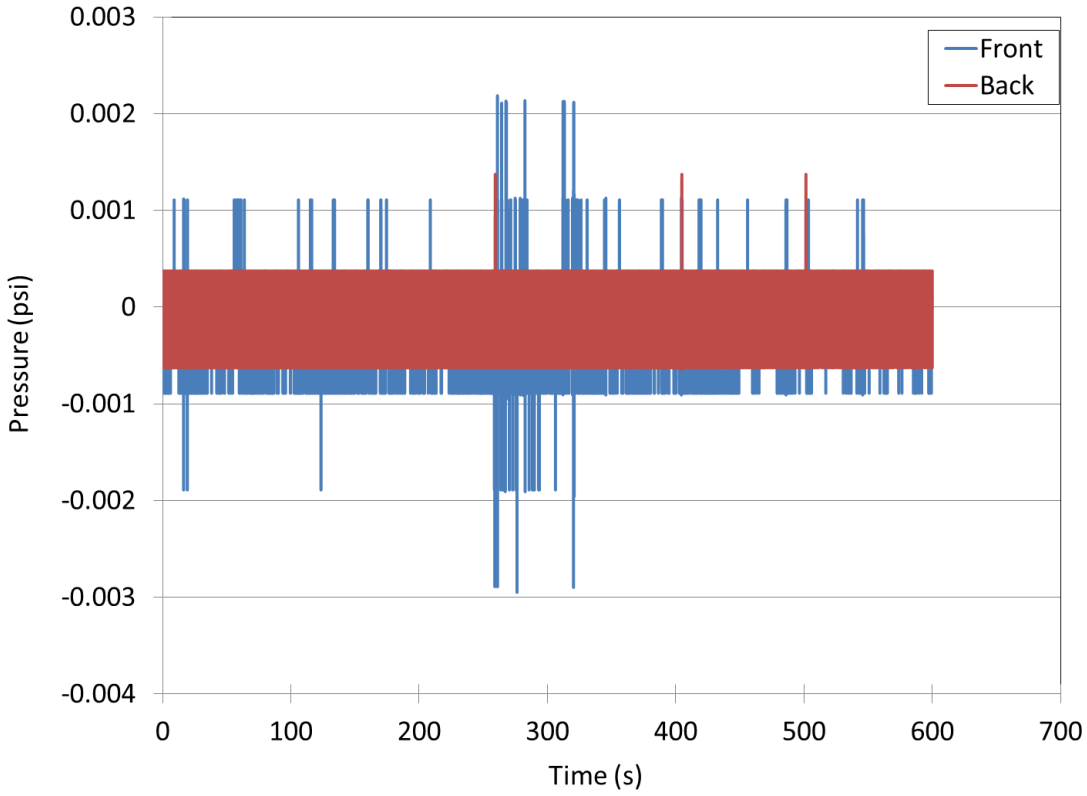

Fig. 50 Ames Truss Pressures

Acceleration data trends tended to be very small with the largest measured acceleration being 0.12g as shown in Table 9 below. Another trend was that accelerometers mounted horizontally had higher magnitudes than accelerometers mounted vertically as shown in Table 9 and also shown in Fig. 51 for the Euclid truss. The one exception to this trend was on the Ames truss where the vertically measured acceleration was larger than the horizontally measured acceleration.

Table 9 Acceleration

| | Columns, Horizontal Orientation | | Orientation on Truss Member | |
|---|---|---|---|---|
| | Perpendicular to Sign | Parallel to Sign | Vertical | Horizontal |
| | g | G | g | g |
| Ames | 0.061 | 0.070 | 0.121 | 0.080 |
| Kellogg | 0.024 | 0.071 | 0.017 | 0.022 |
| Euclid | 0.055 | 0.061 | 0.028 | 0.120 |
| Ankeny DMS | 0.092 | 0.042 | 0.035 | 0.035 |
| Ankeny Sign | 0.028 | 0.013 | 0.030 | 0.095 |

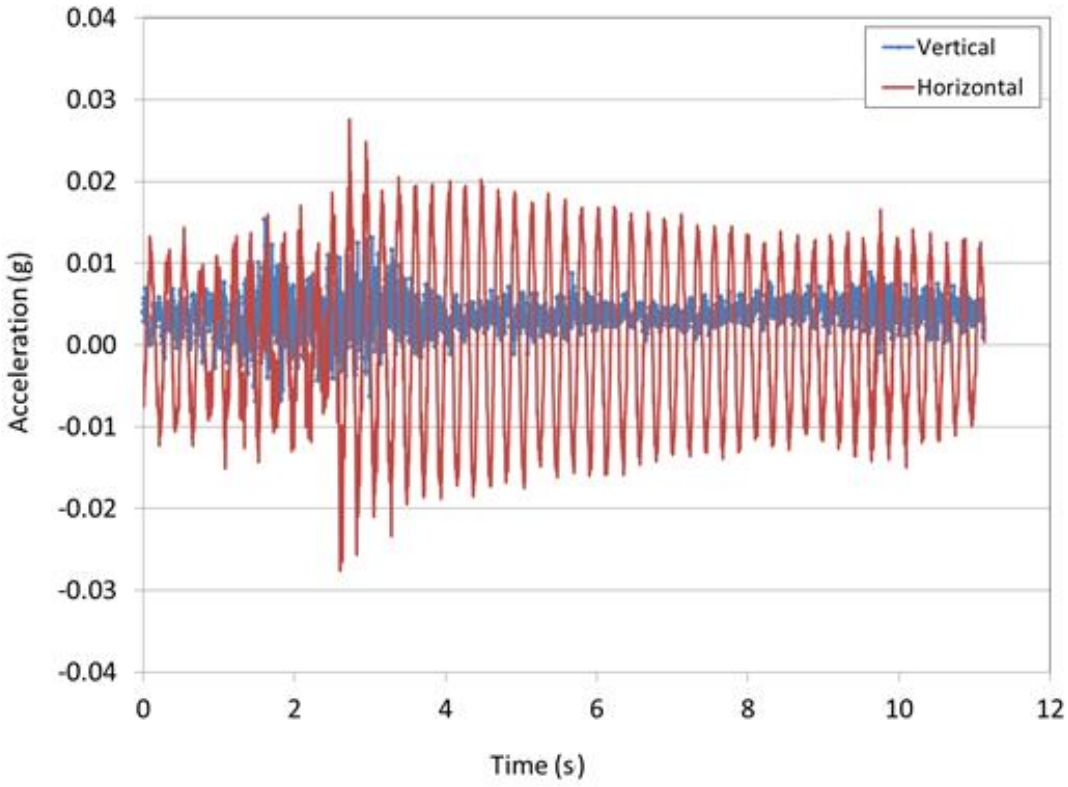


Fig. 51 Euclid Truss Accelerations

The general trend with respect to the measured strains is that the largest strains were measured in the columns followed by the chord members and diagonal members.. An example graph with four sensors on the same member is shown below in Fig. 52. All four sensors have nearly identical strains over time as shown in Fig. 52 and thus the plotted lines overlap. This would indicate that the measured response is primarily axial with very little bending and/or torsion. Lastly, truck gust induced strains were all relatively small with the largest measured strain being 28 microstrain. These small strains will be discussed later. The maximum strain data for Kellogg, Euclid, and Ankeny are shown below in Tables 10, 11, and 12 respectively.

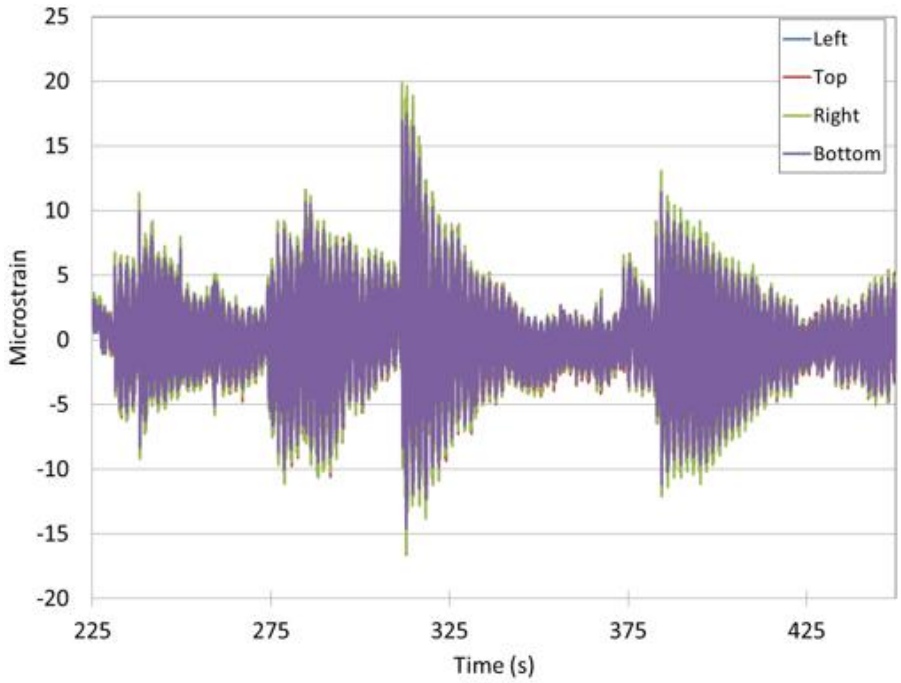

Fig. 52 Strain (aluminum) from Four Sensors on Same Member

Table 10 Kellogg Strains

| Column (steel) | | Chords (steel) | | | | | | | | | |
|---|---|---|---|---|---|---|---|---|---|---|---|
| | | Section A | | Section B | | | | Section C | | | |
| | | Top | | Top | | Bottom | | Top | | Bottom | |
| West | East | East | West | East | West | East | West | East | West | East | West |
| με | με | με | με | Με | με | με | Με | με | με | με | Με |
| 12.5 | 12.0 | 7.4 | 10.1 | 7.2 | 9.2 | 11.0 | 10.0 | 8.5 | 12.1 | 10.2 | 10.0 |

Table 11 Euclid Strains (N-North, S-South)

| Column (steel) | | | | Chords (aluminum) | | | | Diagonals (aluminum) | | | | | |
|---|---|---|---|---|---|---|---|---|---|---|---|---|---|
| West Truss | | East Truss | | Top | | Bottom | | Sect. B | | Sect. C | | Sect. D | |
| N | S | N | S | N | S | N | S | N | S | Top | Bottom | N | S |
| με | με | με | με | με | με | με | με | με | με | Με | με | Με | με |
| 2.1 | 2.0 | 1.8 | 2.4 | 3.6 | 4.0 | 4.6 | 3.8 | 1.8 | 3.4 | 1.6 | 1.3 | 1.8 | 2.1 |

Table 12 Ankeny Strains

| | Chords (aluminum) | | | | Diagonals (aluminum) | | | |
|---|---|---|---|---|---|---|---|---|
| | Top | | Bottom | | Top | Bottom | North | South |
| | North | South | North | South | | | | |
| | με | με | Με | με | Με | Με | με | Με |
| DMS Truss | 23 | 20 | 20 | 22 | 14 | 17 | 13 | 5 |

| | | | | | | | | |
|---|---|---|---|---|---|---|---|---|
| Sign Truss | 26 | 26 | 28 | 27 | 13 | 15 | 8 | 9 |

The temperature induced strains measured at the Ames truss far exceeded any strains resulting from wind. This revelation guided much of the work described subsequently. A graph of temperature induced strains is shown in Fig. 53.

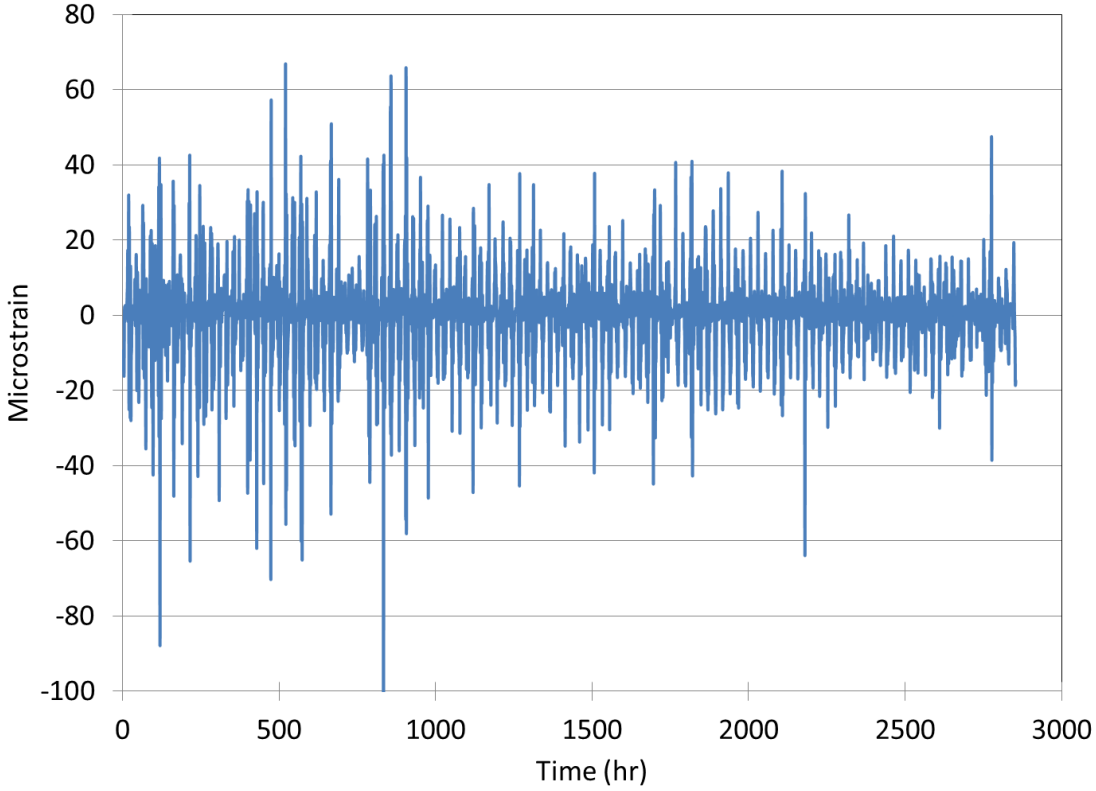


Fig. 53 Temperature Induced Strains (aluminum)

The Ankeny DMS truss and Sign truss were selected to analyze stresses and computed internal forces. The stresses included: axial stress, x-axis bending stress which is vertical, and y-axis stress which is horizontal. The axial forces were also calculated and are shown below in Table 13 and Table 14. As with the measured strains, and as expected, the wind induced forces and stresses were all small. Another trend is that axial stresses in the chords were greater than in the diagonals. Likewise, axial forces in the chords were greater than in the diagonals with the largest axial force of 1.0 kips. In the chords, y-axis bending stresses, meaning bending the member horizontally, were greater than x-axis bending stress with the largest being 0.095 ksi. In the diagonals, only the x-axis bending stresses, meaning bending vertically, were measured and the largest was 0.11 ksi. Also, the x-axis bending stresses were generally larger in the diagonals than in the chords. The difference in strains in a given member cross section were small, typically 5 microstrain, and the corresponding bending stresses were small. Therefore the bending forces in the truss members are insignificant.

Table 13 Ankeny DMS Truss

| | | Chords (aluminum) | | | | Diagonals (aluminum) | | | |
|---|---|---|---|---|---|---|---|---|---|
| | | North Top | South Top | South Bottom | North Bottom | Top | South | Bottom | North |
| Max Strain | με | 23.0 | 20.2 | 22.1 | 20.0 | 14.0 | 5.1 | 17.0 | 13.0 |
| Average Strain | με | 21.6 | 18.2 | 20.6 | 18.5 | 11.2 | 3.6 | 13.4 | 7.3 |
| X-Axis Strain Difference | με | 1.1 | 1.4 | 1.4 | 0.0 | 3.6 | 3.9 | 6.2 | 10.7 |
| Y-Axis Strain Difference | με | 3.5 | 3.3 | 3.5 | 3.0 | NA | NA | NA | NA |
| Outside Diameter | in | 5.50 | 5.50 | 5.50 | 5.50 | 2.75 | 2.50 | 2.75 | 2.50 |
| Area | $in^2$ | 4.123 | 4.123 | 4.123 | 4.123 | 1.963 | 1.767 | 1.963 | 1.767 |
| Axial Stress | ksi | 0.216 | 0.182 | 0.206 | 0.185 | 0.112 | 0.036 | 0.134 | 0.073 |
| X-Axis Bending Stress | ksi | 0.011 | 0.014 | 0.014 | 0.000 | 0.036 | 0.039 | 0.062 | 0.107 |
| Y-Axis Bending stress | ksi | 0.035 | 0.033 | 0.035 | 0.030 | NA | NA | NA | NA |
| Axial Force | kip | 0.891 | 0.750 | 0.849 | 0.763 | 0.220 | 0.064 | 0.263 | 0.129 |

A comparison of the DMS truss and the Sign truss at Ankeny did not reveal any significant differences in their short-term behavior. However, as shown previously in Table 13 and Table 14, the chord strains were greater in the Sign truss than in the DMS truss while the diagonal strains were greater in the DMS truss than in the Sign truss. The difference in chord strains are likely due to the fact that the Sign truss had a much larger sign area facing the wind and truck gusts. The DMS truss had greater, overall, accelerations than the Sign truss as shown previously in Table 9. In conclusion, having a DMS sign instead of a regular sign mounted on a truss did not have a significant effect on truss performance from short-term wind loads.

The gradient gage consisting of 5 closely spaced sensors that was installed on the Ankeny truss near the West column support revealed expected trends. The strain magnitudes were all small with a maximum of 20 microstrain as shown in Table 15. Note that sensor 1 is farthest from the support. Also the strain magnitudes were slightly less at sensors that were farther from the column support as shown in Table 16 and Fig. 54. This makes sense since the strain should be larger closer to the support since the support carries loads from multiple members.

Table 14 Ankeny Sign Truss (Aluminum)

| | | Chords | | | | Diagonals | | | |
|---|---|---|---|---|---|---|---|---|---|
| | | North Top | South Top | South Bottom | North Bottom | Top | South | Bottom | North |
| Max Strain | με | 26.0 | 26.0 | 27.0 | 28.0 | 13.0 | 9.0 | 15.0 | 8.0 |
| Average Strain | με | 20.6 | 24.3 | 23.9 | 23.2 | 12.1 | 6.0 | 14.6 | 5.4 |
| X-Axis Strain Difference | με | 3.7 | 0.9 | 0.1 | 0.8 | 0.8 | 3.3 | 0.2 | 5.4 |
| Y-Axis Strain Difference | με | 8.3 | 4.4 | 0.3 | 9.5 | NA | NA | NA | NA |
| Outside Diameter | in | 5.50 | 5.50 | 5.50 | 5.50 | 2.75 | 2.50 | 2.75 | 2.50 |
| Area | $in^2$ | 4.123 | 4.123 | 4.123 | 4.123 | 1.963 | 1.767 | 1.963 | 1.767 |
| Axial Stress | ksi | 0.206 | 0.243 | 0.239 | 0.232 | 0.121 | 0.060 | 0.146 | 0.054 |
| X-Axis Bending Stress | ksi | 0.037 | 0.009 | 0.001 | 0.008 | 0.008 | 0.033 | 0.002 | 0.054 |
| Y-Axis Bending stress | ksi | 0.083 | 0.044 | 0.003 | 0.095 | NA | NA | NA | NA |
| Axial Force | kip | 0.849 | 1.002 | 0.985 | 0.957 | 0.238 | 0.106 | 0.287 | 0.095 |

Table 15 Maximum Strains (Aluminum) in Gradient Gage

| Gradient Sensor Number | | | | |
|---|---|---|---|---|
| 1 | 2 | 3 | 4 | 5 |
| με | με | με | με | με |
| 14 | 16 | 16 | 17 | 20 |

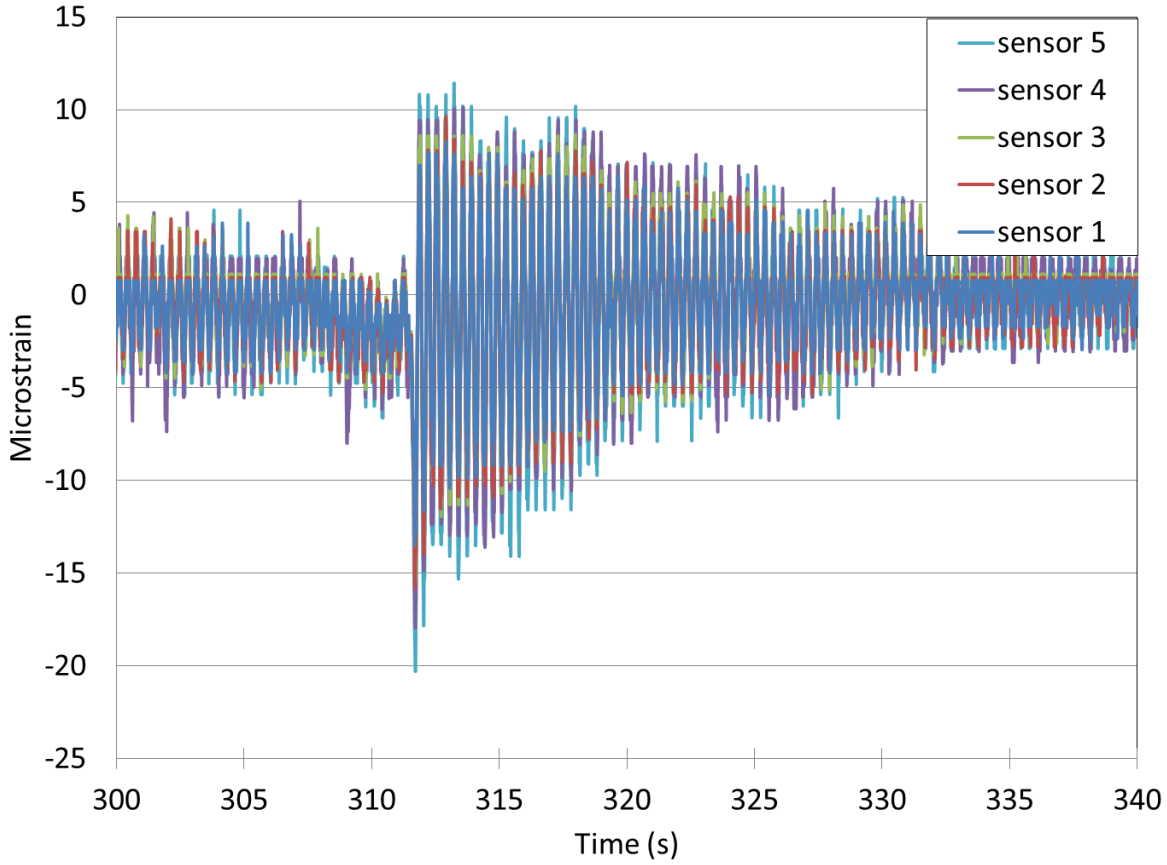


Fig. 54 Gradient Gage Strains (Aluminum)

The structural fundamental frequencies of each truss were determined by performing Fast Fourier Transform analyses. All of the accelerometers were used in the analyses and the results are listed in Table 16. A sample graph of the Fast Fourier Transform results for the trusses: Ames, Kellogg, Euclid, Ankeny DMS, and Ankeny Sign are shown in Figs. 55, 56, 57, 58, and 59 respectively. Results for the third fundamental frequency in the Ames and Ankeny Sign trusses were not consistent so they are not listed.

Table 16 Fundamental Frequencies

| | First | Second | Third |
|---|---|---|---|
| Ames | 4.0 | 4.7 | - |
| Kellogg | 4.4 | 14.4 | 15.7 |
| Euclid | 4.4 | 8.6 | 13.1 |
| Ankeny DMS | 2.9 | 3.5 | 7.1 |
| Ankeny Sign | 3.4 | 4.6 | - |

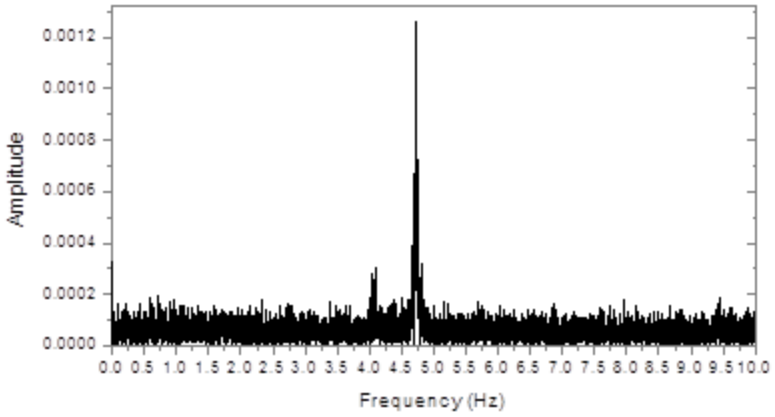


Fig. 55 Ames FFT

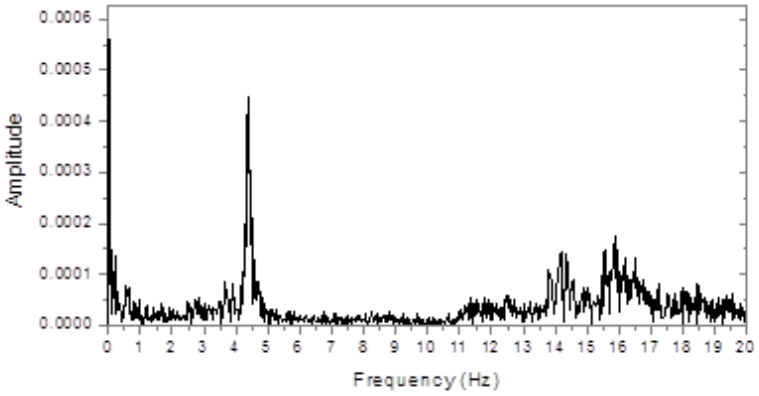


Fig. 56 Kellogg FFT

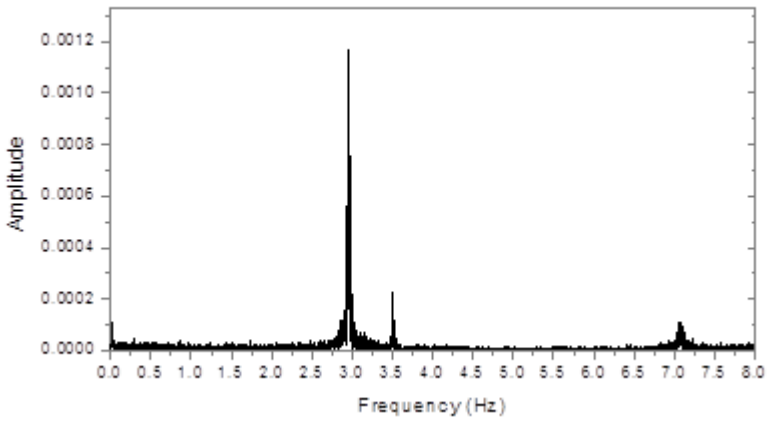


Fig. 57 Euclid FFT

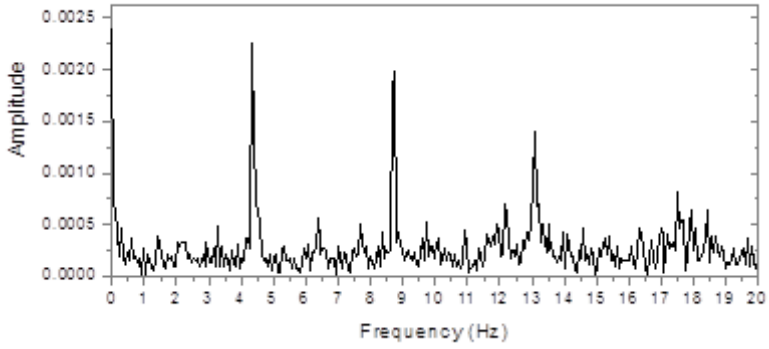


Fig. 58 Ankeny DMS FFT

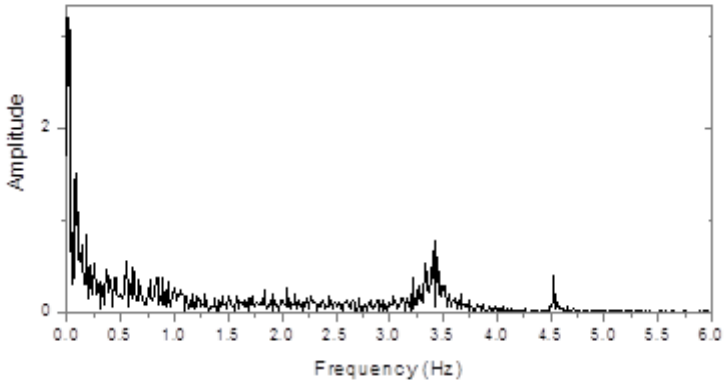


Fig. 59 Ankeny Sign FFT

The general results from the field monitoring are summarized as follows. First recall that in the presentation made in this section, data files were selected that had one or more of the following features: high wind speed, wind direction approximately perpendicular to the sign, or a worst case truck and travel lane combination creating large wind gusts. The maximum wind pressures were close to 0.35 psi (50.4 psf). Accelerations were fairly small, with the largest being 0.12g and the trusses moved more horizontally than vertically. The largest strains were relatively small along with the corresponding axial stresses, bending stresses, and axial forces. The largest axial force was 1.0 kip. The horizontal bending stresses were greater than the vertical bending stresses. However the bending stresses were small and the largest was 0.11 ksi. A truss with a DMS cabinet did not perform significantly different under wind loads than a truss with a regular sign. Lastly, the five trusses may look similar but are structurally different as proved in FFT analysis. In conclusion, the loads from wind and wind gusts from trucks are not significant enough to likely cause failure in the truss members.

## 6. Long-term monitoring: Field study and data analysis

### 6.1. Fatigue evaluation of trusses: literature review

AASHTO Standard Specifications for Structural Supports for Highway Sign, Luminaires and Traffic Signals (AASHTO, 2010) defines the limit loads and fatigue design process for

cantilevered and non-cantilevered steel and aluminum structures supporting highway sign, luminaires and traffic signals. The loads are defined to be dead load, live load, wind load, and ice load. The limit strength for both aluminum alloy and its welding are listed in the specification as shown in Table 17. The typical fatigue-sensitive connection details contribute to the stress categories through A to K2, and a constant-amplitude fatigue limit (CAFL) is allocated to each category for fatigue estimation. A stress range below the CAFL at each fatigue category is considered to provide infinite life without leading to fatigue failure. The typical connection for the highway overhead support structures in this study is a fillet-welded chord-to-vertical and chord-to-diagonal connections with $r / t \leq 24$ (where r is the radius of column and t is thickness), which is defined as ET in AASHTO standards (Fig. 60). The allowable CAFL for this stress category is given as 0.44 ksi for Aluminum. A stress range larger than 0.44 ksi should be evaluated for fatigue. Although CAFLs for various categories have been defined in the AASHTO standard specification, the life cycle corresponding to CAFL is not included. The constants to derive fatigue cycles can be found in AASHTO LRFD Bridge code (AASHTO, 2004). By analyzing the combined data from both standard specification and the bridge code, S-N curve can be extrapolated. Table 18 lists some important parameters from the AASHTO codes.

Table 17 Mechanical properties of Aluminum alloy T-6061 in AASHTO standards

| Material | Tension | | Compression | Shear | | Bearing | |
|---|---|---|---|---|---|---|---|
| | Ultimate (ksi) | Yield (ksi) | Yield (ksi) | Ultimate (ksi) | Yield (ksi) | Ultimate (ksi) | Yield (ksi) |
| T6061 | 38 | 35 | 35 | 24 | 20 | 80 | 56 |
| T6061 with 5556 filler | 24 | 20 | 20 | 15 | 12 | 50 | 30 |

Table. 18 Fatigue parameters for various categories in AASHTO for aluminum alloy

| Fatigue Category | $C_f$ (cycles/ksi$^{1/m}$) | M | CAFL (ksi) |
|---|---|---|---|
| A | 1.00E+13 | 0.155 | 10.2 |
| B | 5.20E+10 | 0.211 | 6.0 |
| C | 3.60E+09 | 0.237 | 4.0 |
| D | 8.40E+08 | 0.249 | 2.5 |
| E | 1.20E+08 | 0.284 | 1.9 |
| ET | - | - | 0.44 |

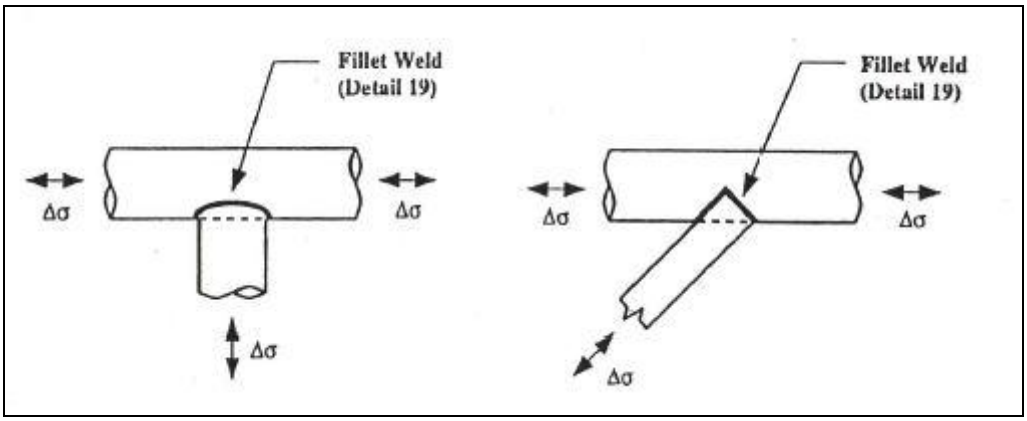


Fig. 60 ET stress category (AASHTO, 2010)

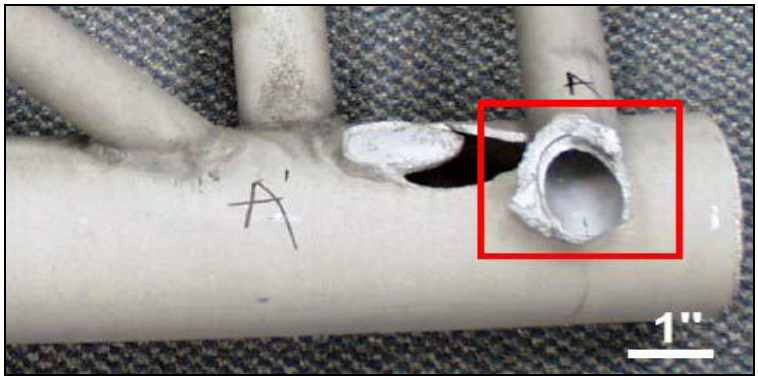


a) Crack at fillet-welding

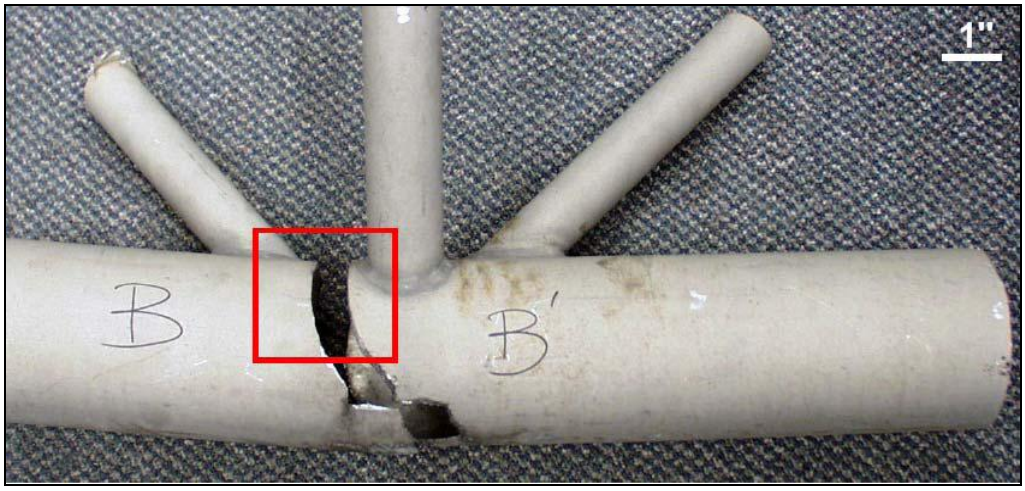


b) Crack at welding heat zone

Fig. 61 Cracks of fillet welding on truss support

The Illinois Department of Transportation (Foutch, Rice, LaFave, Valdovinos, and Kim, 2006) conducted research with respect to the fatigue of bridge-type overhead truss support structures. A

set of field monitoring tests were designed for different types of structures and the data were processed to study the efficacy of the DOT's design specification. Fast Fourier Transform was used to identify the structure natural frequencies. Stress values were extrapolated for fatigue analysis and a damper system was discussed as a tool to minimize the effect of structural vibration from wind loads. The study concluded that the current Illinois DOT design satisfied the AASHTO standards.

A Dayton, Ohio sign truss failure was investigated by a research team (Huckelbridge and Metzger, 2007) at Case Western Reserve University. The research focused on truck-induced vibration, and related field tests were conducted. Finite element modeling was used to identify the natural frequency of the truss structure. The study extrapolated S-N curve information based on the AASHTO specification and other codes. Constant amplitude stress was also developed and fatigue life was estimated based on Palmgren-Miner Rule. A metallurgical examination was performed to verify the conclusions. Figure 61 shows the failures in the investigation. Figure 61a shows that the failure occurred near the weld area that totally separated from the main chord. The failure shown in Fig. 61b occurred near the heat affected zone, which caused the main chord to be broken into two pieces.

University of Pittsburgh analyzed the wind loads induced on truss structures (Kacin, Rizzo and Tajari, 2010). The methodology was mainly derived from numerical modeling. The research project concluded that the critical members were the welded diagonal members and they have an infinite fatigue life under normal conditions.

The Alabama Department of Transportation performed a fatigue evaluation of two DMS structures (McLean, Park, and Stallings, 2004) using numerical modeling and field tests. A finite fatigue life was determined for several truss members based on the AASHTO specifications. The largest stress range occurred near the truss chord splices.

## 6.2. Field data analysis

The results of the long-term field monitoring program conducted on the previously described Ames truss are summarized in this subsection. Note that the measured data were converted to one-minute ranges or averaged during data processing unless otherwise is specified.

### *6.2.1. Wind induced vibration*

Figure 62 shows the measured wind speed and the corresponding strain range, which presents a low correlation between each other. The strain range has a trend to increase when wind speed is increasing. The maximum strain occurred around wind speed of 5 mph. The measured pressure data are plotted against average windspeed in Fig. 63. In this figure, the pressures are almost constant regardless of the wind speed. Hence the pressure data are not analyzed further.

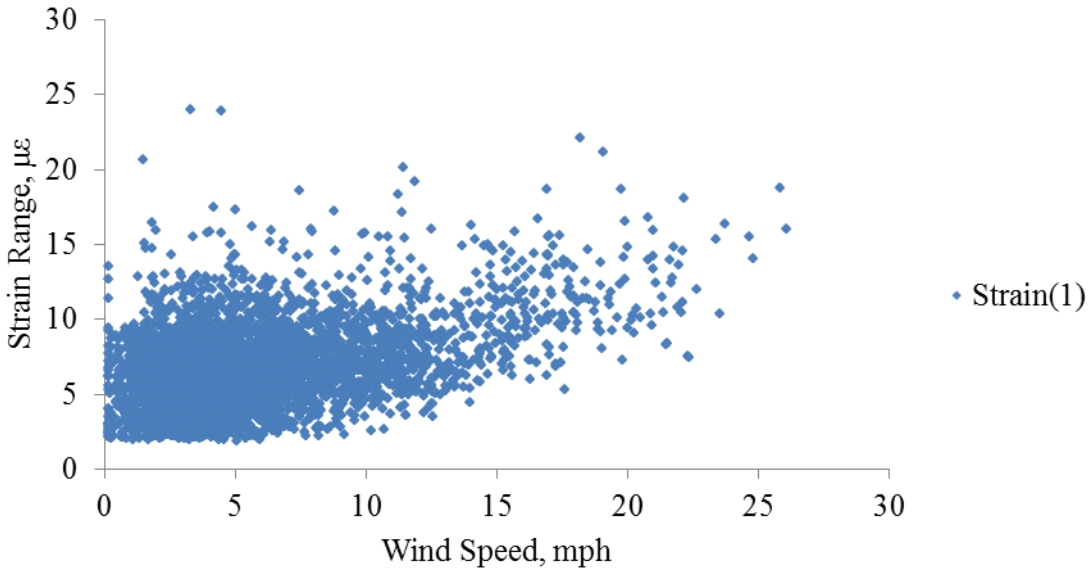


a) Strain range 1 in chord member gages

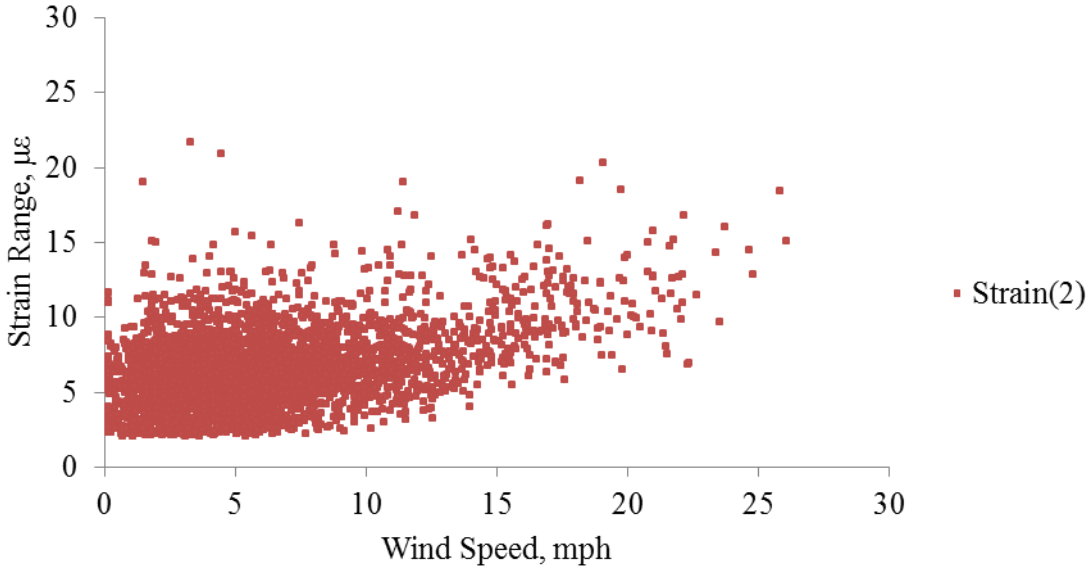


b) Strain range 2 in chord member gages

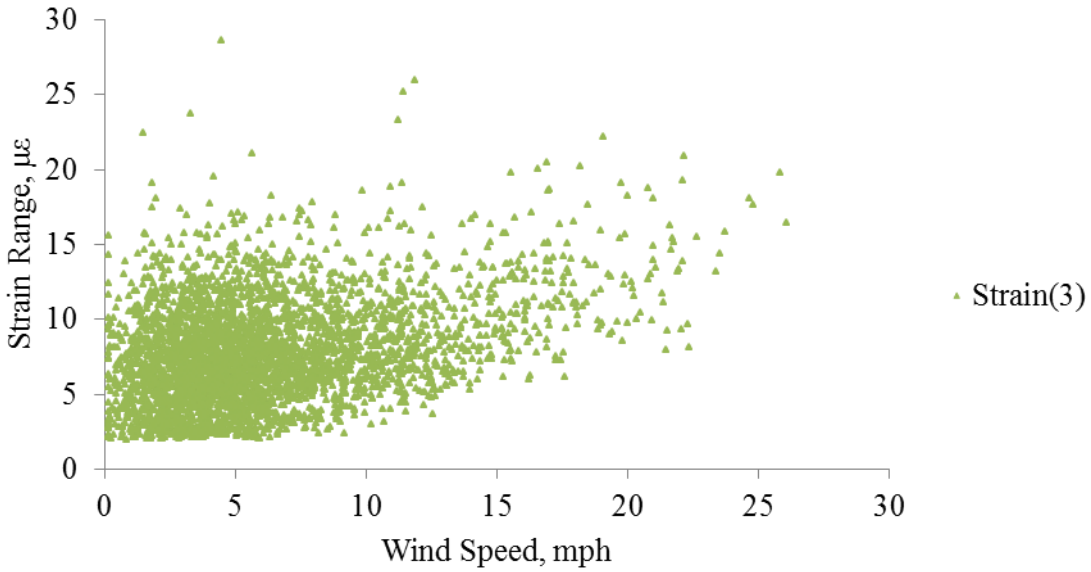


c) Strain range 3 in chord member gages

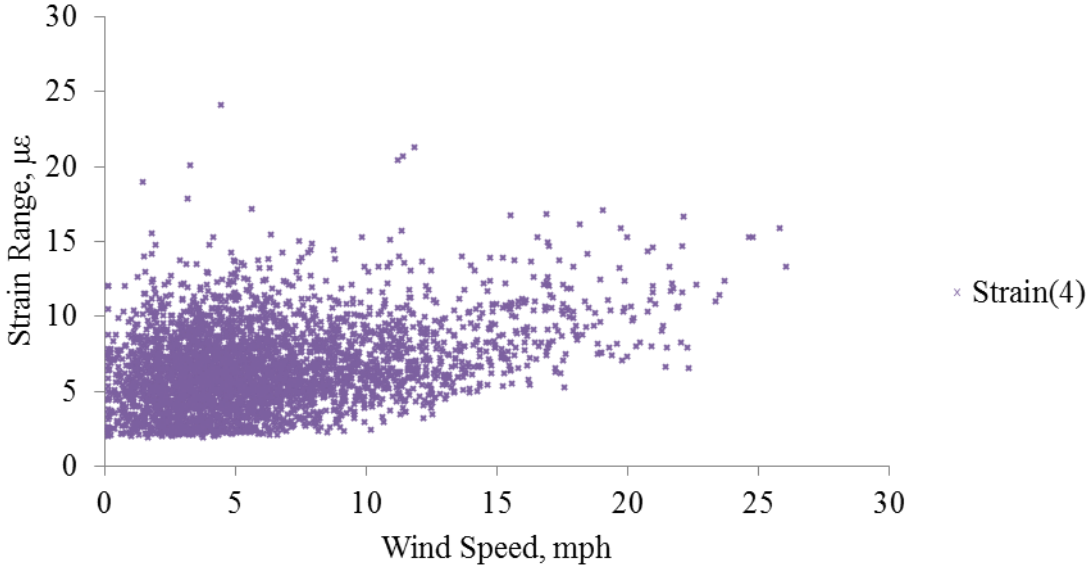


d) Strain range 4 in chord member gages

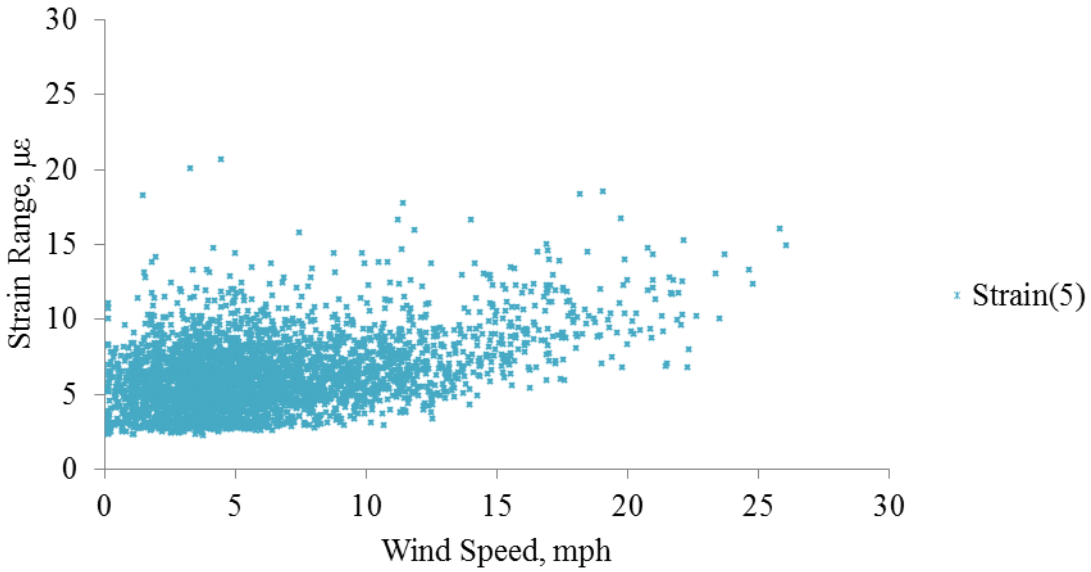


e) Strain range 5 in chord member gages

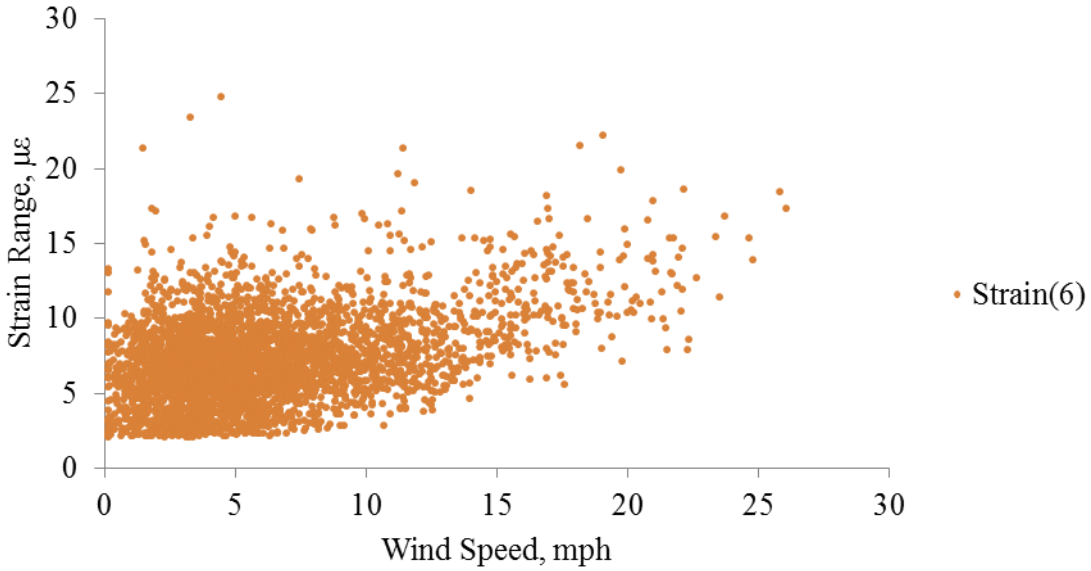


f) Strain range 6 in chord member gages

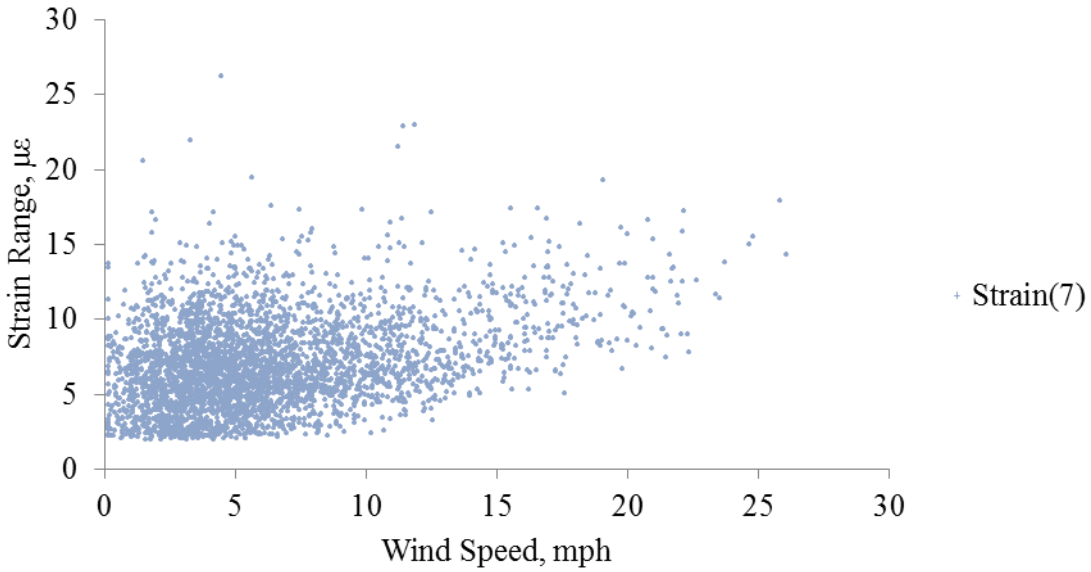


g) Strain range 7 in chord member gages

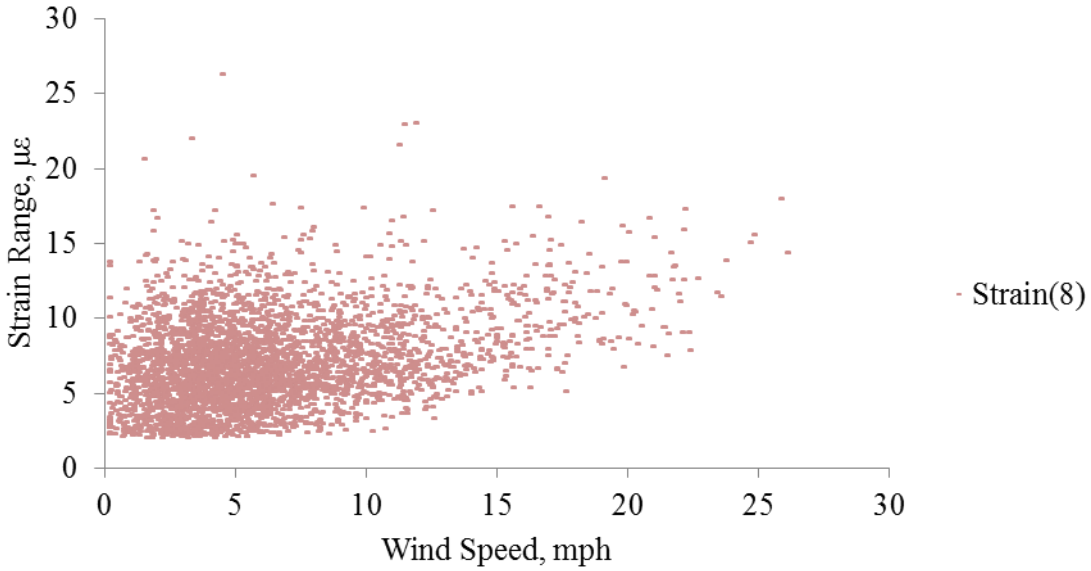


h) Strain range 8 in chord member gages

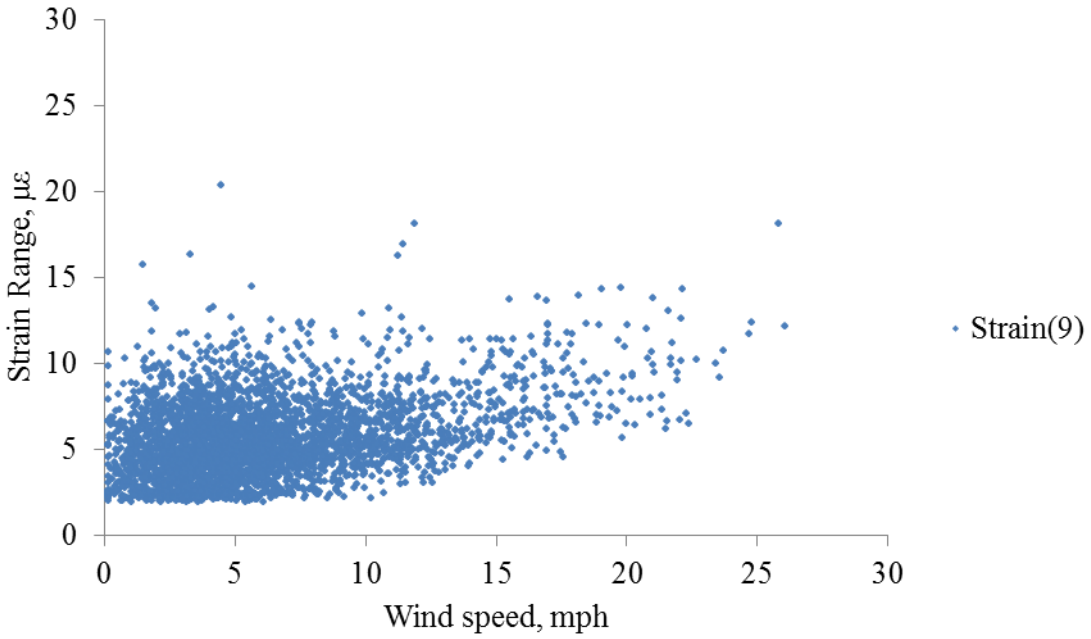


i) Strain range 9 in chord member gages

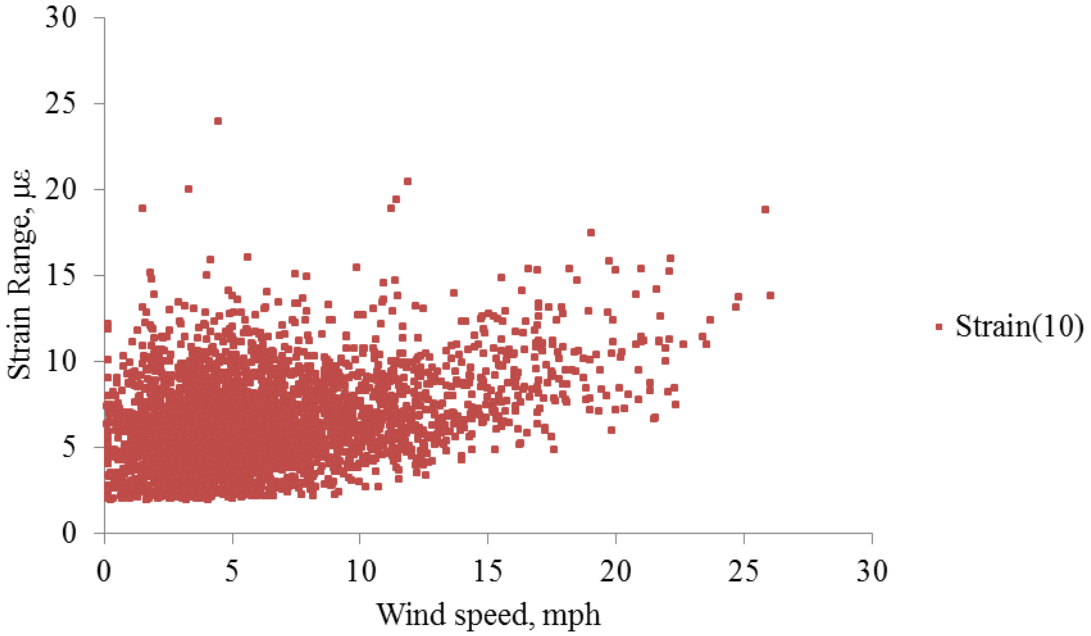


j) Strain range 10 in chord member gages

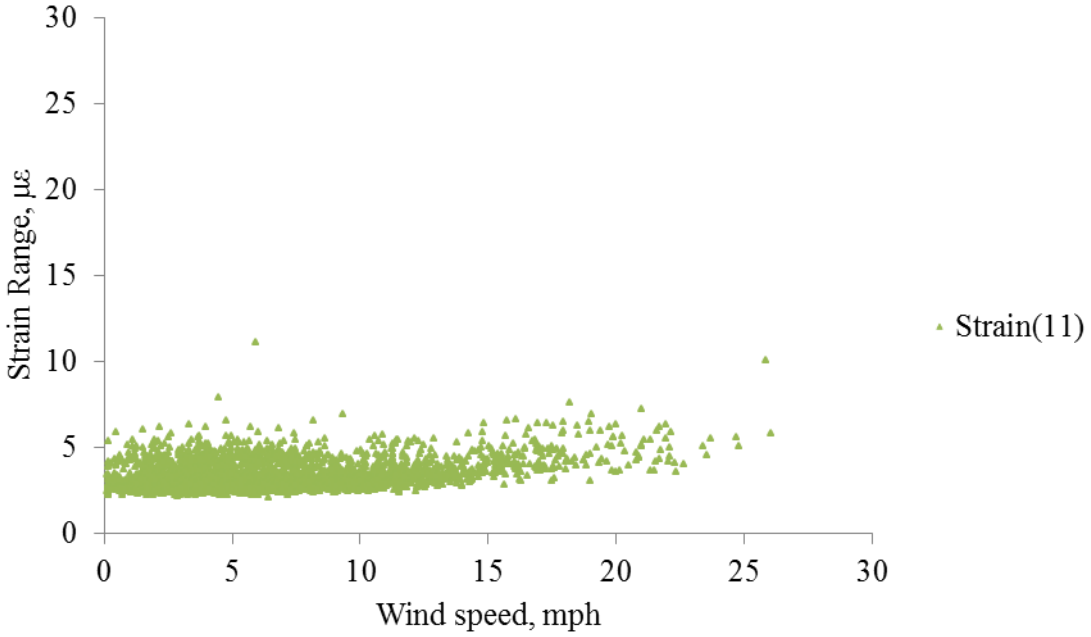


k) Strain range 11 in chord member gages

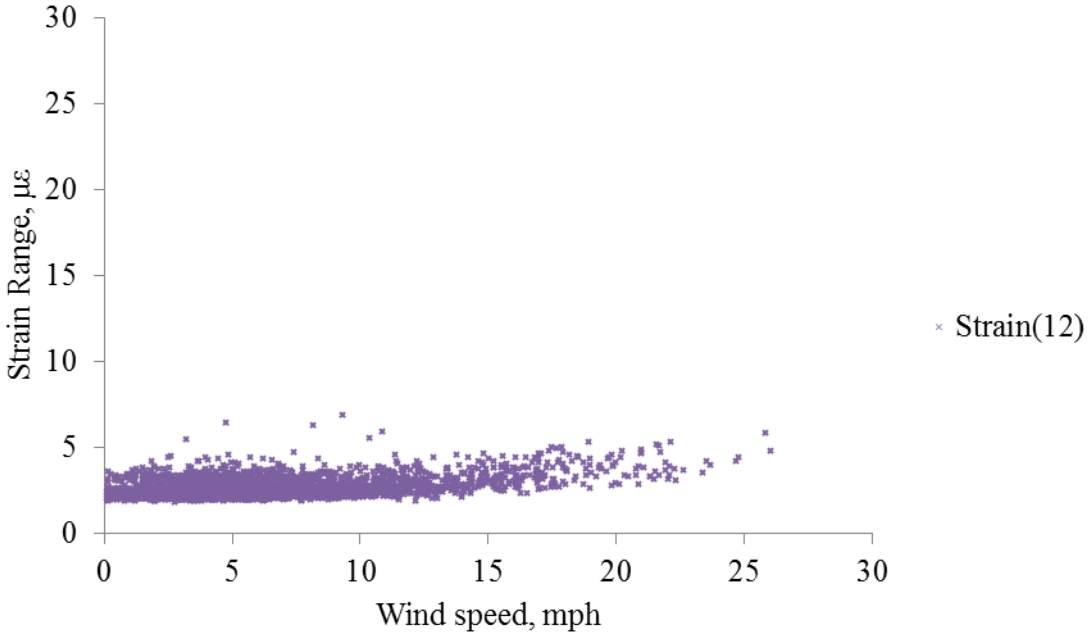


l) Strain range 12 in chord member gages

Fig. 62 Strain range in various wind speed range

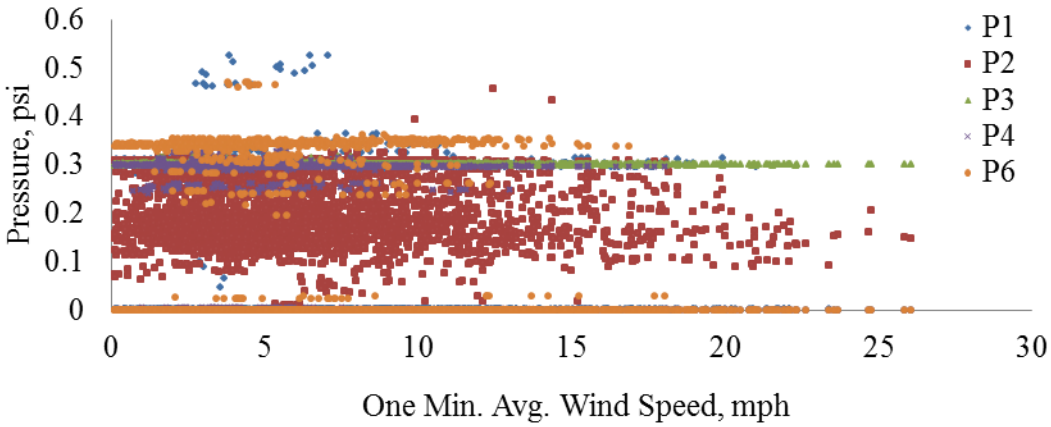


Fig. 63 Pressure value in average wind speed

### *6.2.2. Truck induced vibration*

Figure 64 presents 10-minute records for wind speed, acceleration, and strain. An event around 14:04 in the figure shows a typical structural excitation from a truck-induced gust.

Figure 65 presents a detailed acceleration, strain plots and wind direction during the period following the truck induced vibration. Wind speed and direction are also shown in Figs. 65c and 65d. From the wind speed measured on top of DMS, it was observed that there was no strong ambient wind gust during the period. There was no significant change in wind direction either. Figure 66 shows the strain range verses acceleration range. As acceleration range increases, strain range has a trend to increase. The maximum strain was found at an acceleration of 0.15g.

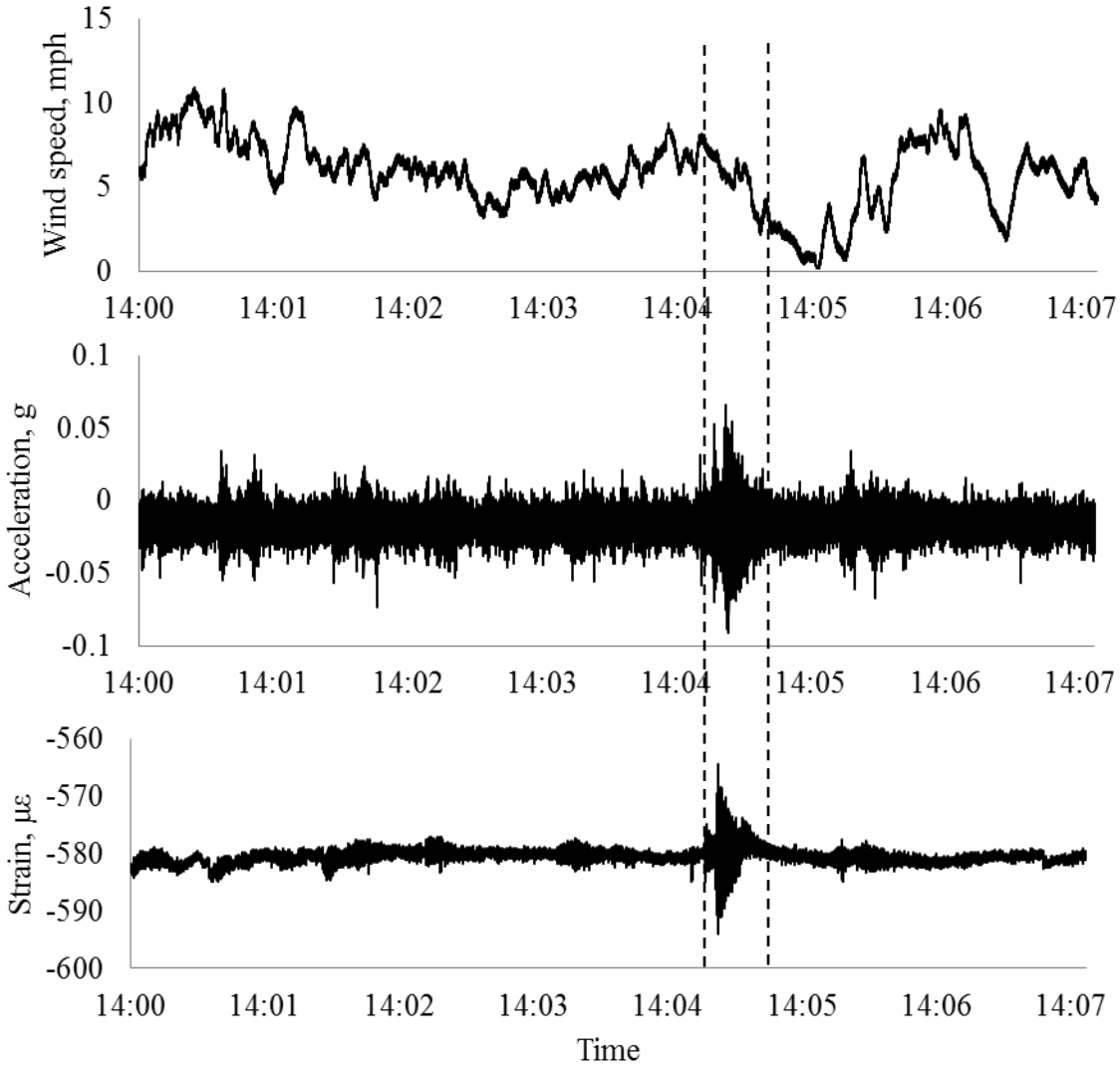


Fig. 64 Truck induced vibration

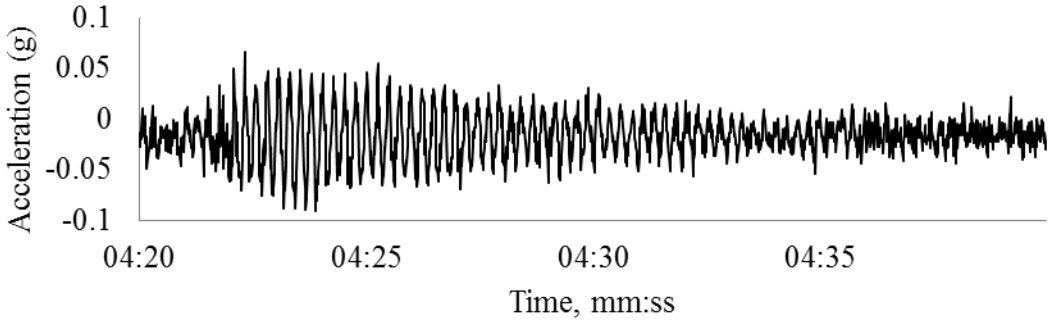


a) Acceleration

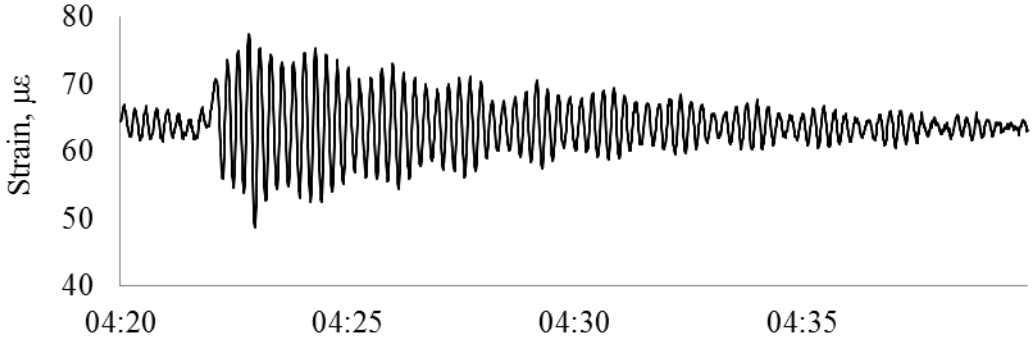


b) Strain

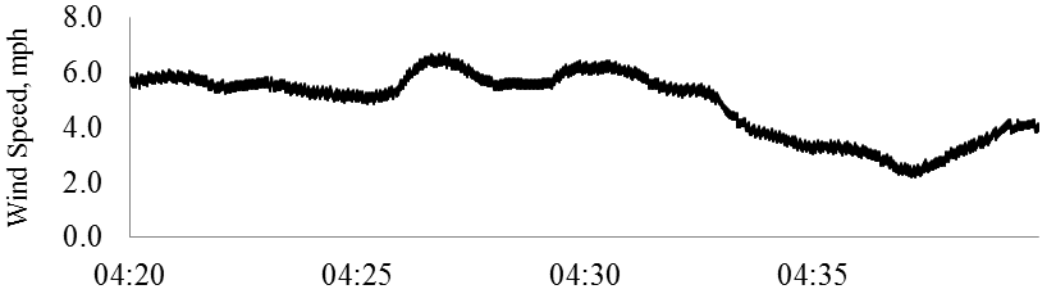


c) Wind speed

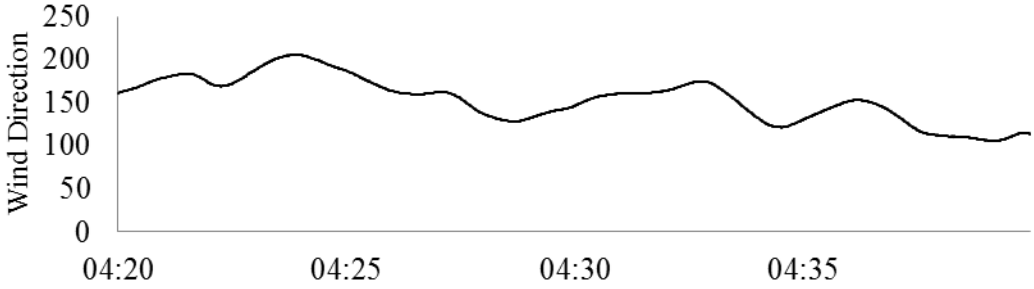


d) Wind direction

Fig. 65 Acceleration and strain fluctuation by truck-induced gust

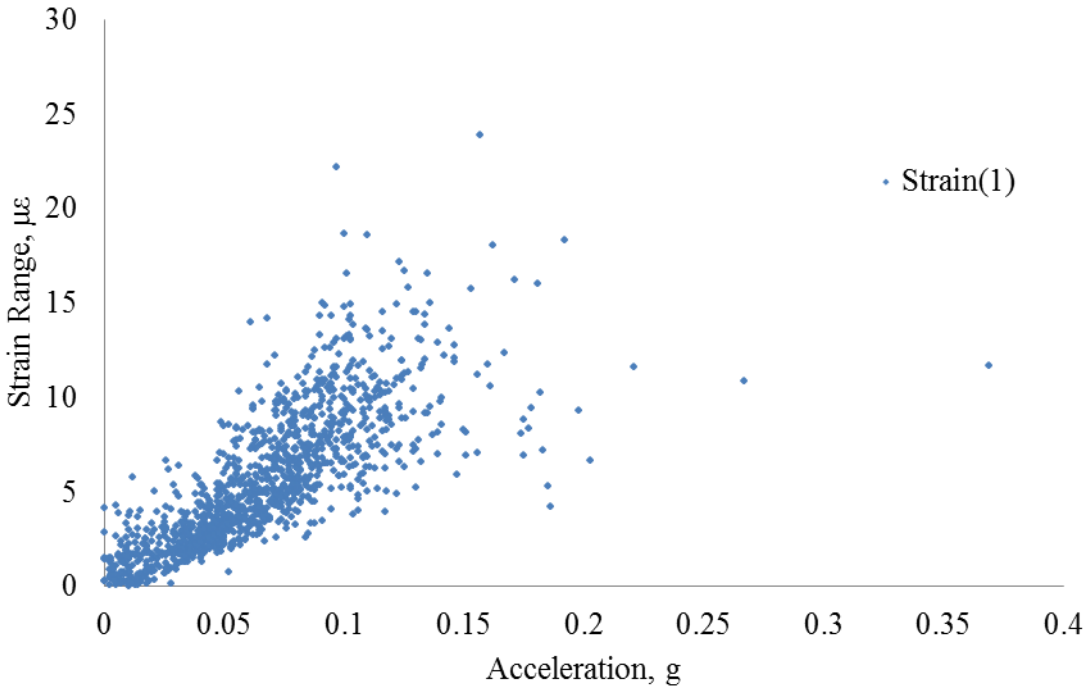


a) Strain gage 1

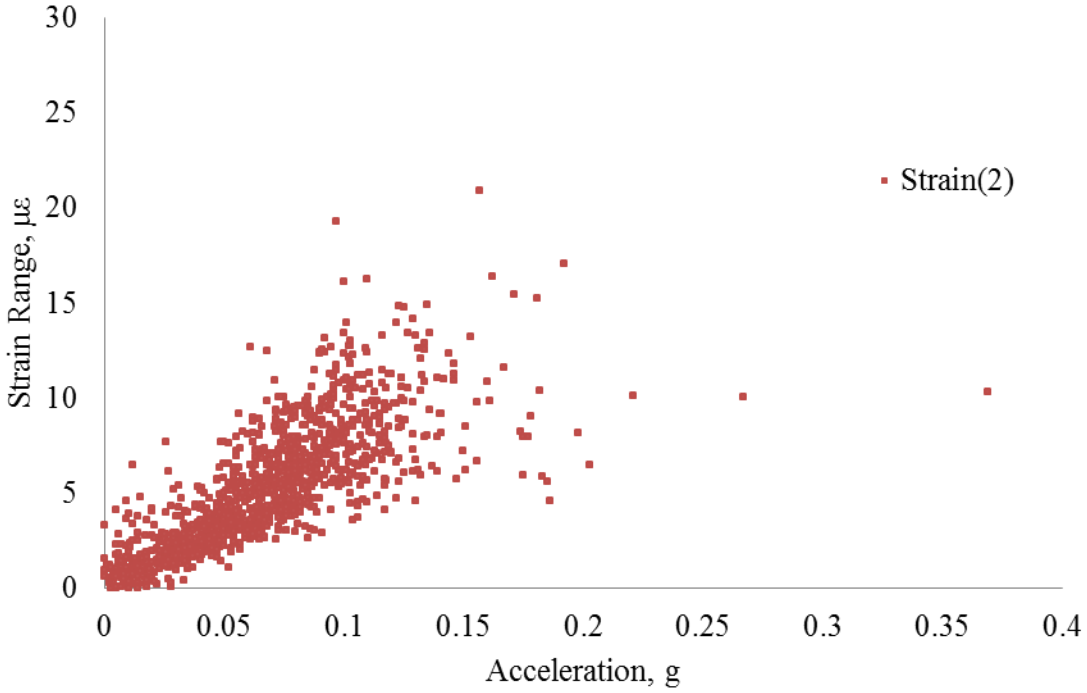


b) Strain gage 2

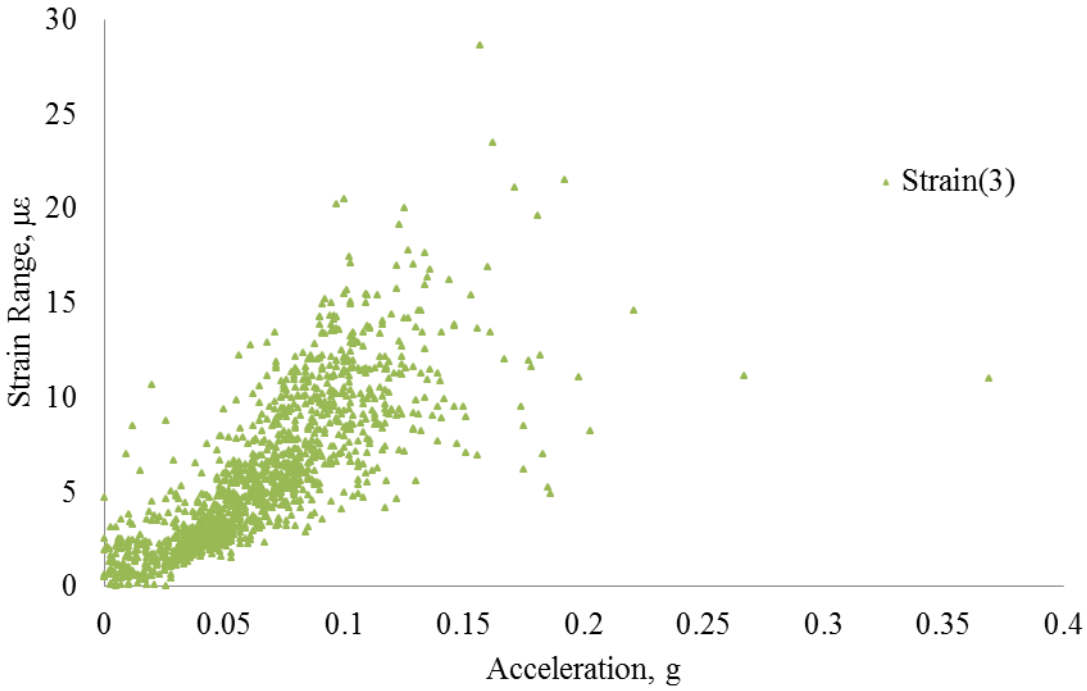


c) Strain gage 3

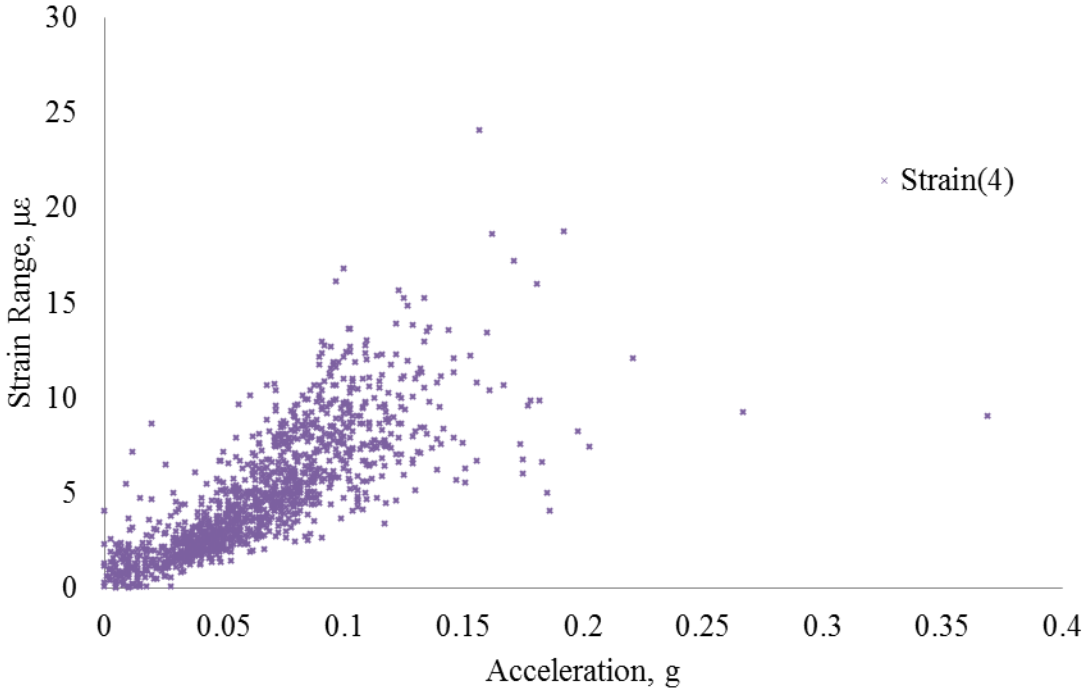


d) Strain gage 4

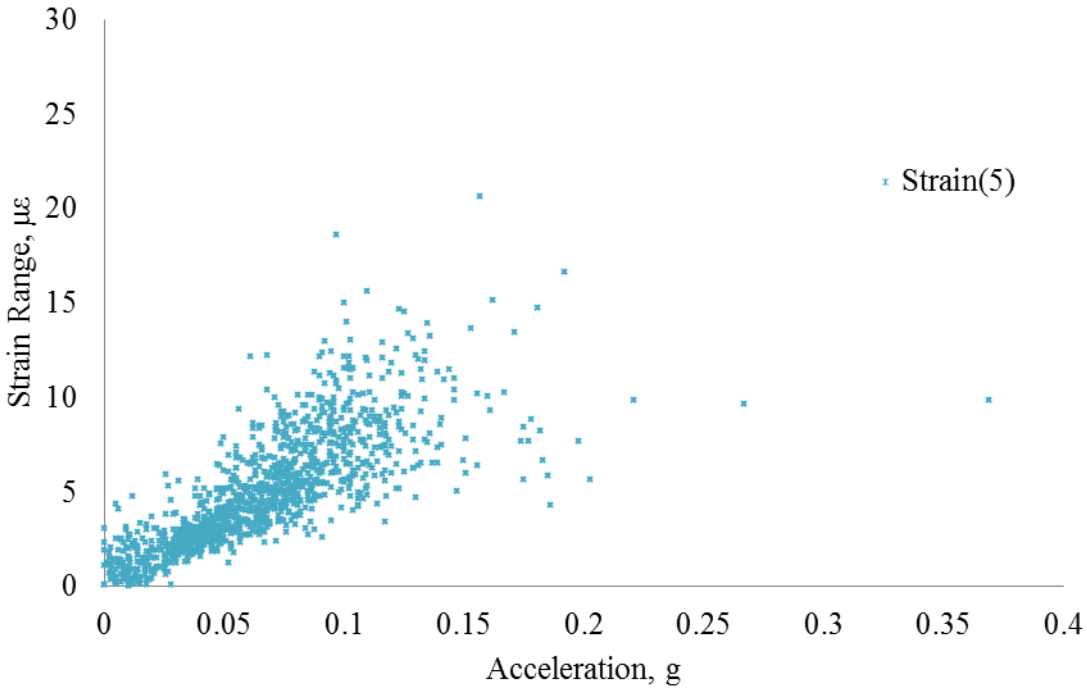


e) Strain gage 5

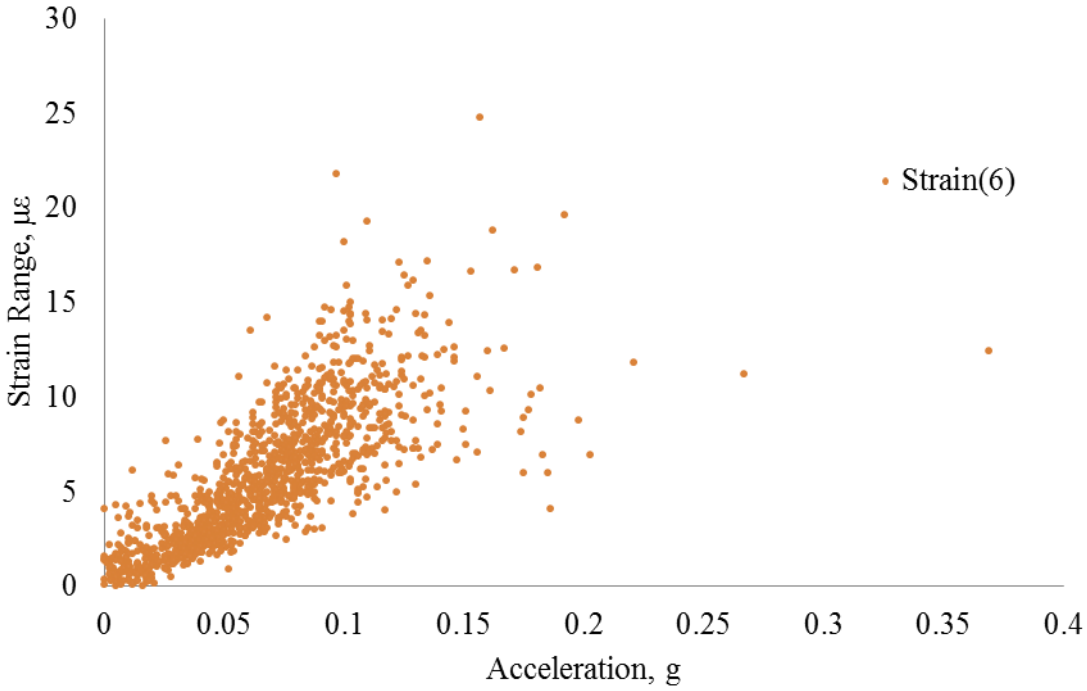


f) Strain gage 6

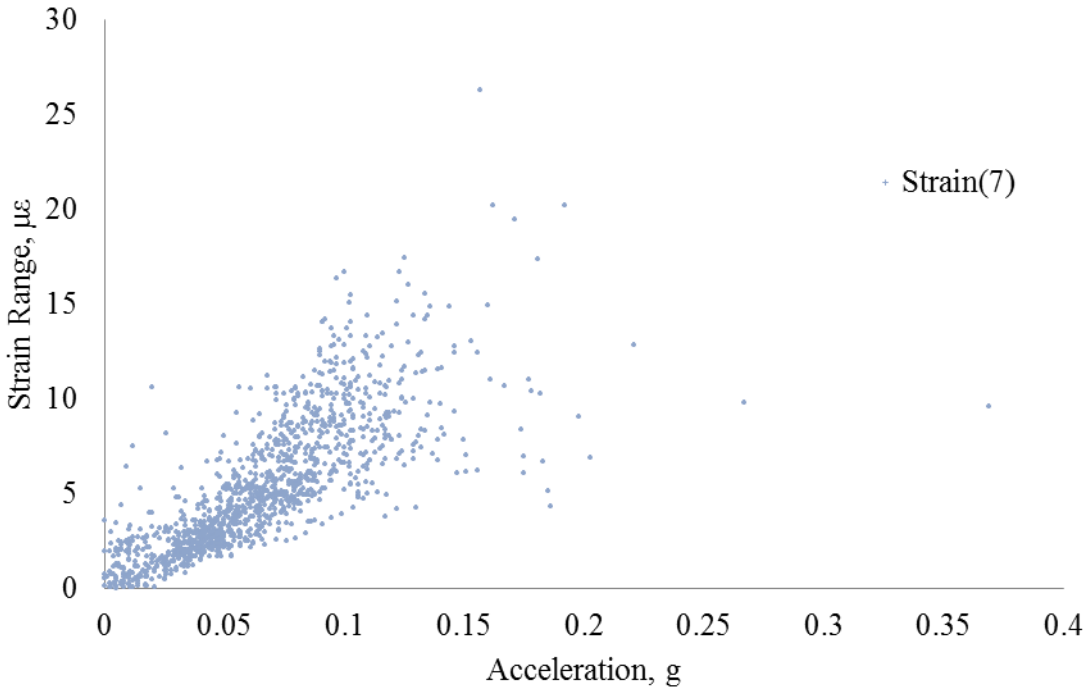


g) Strain gage 7

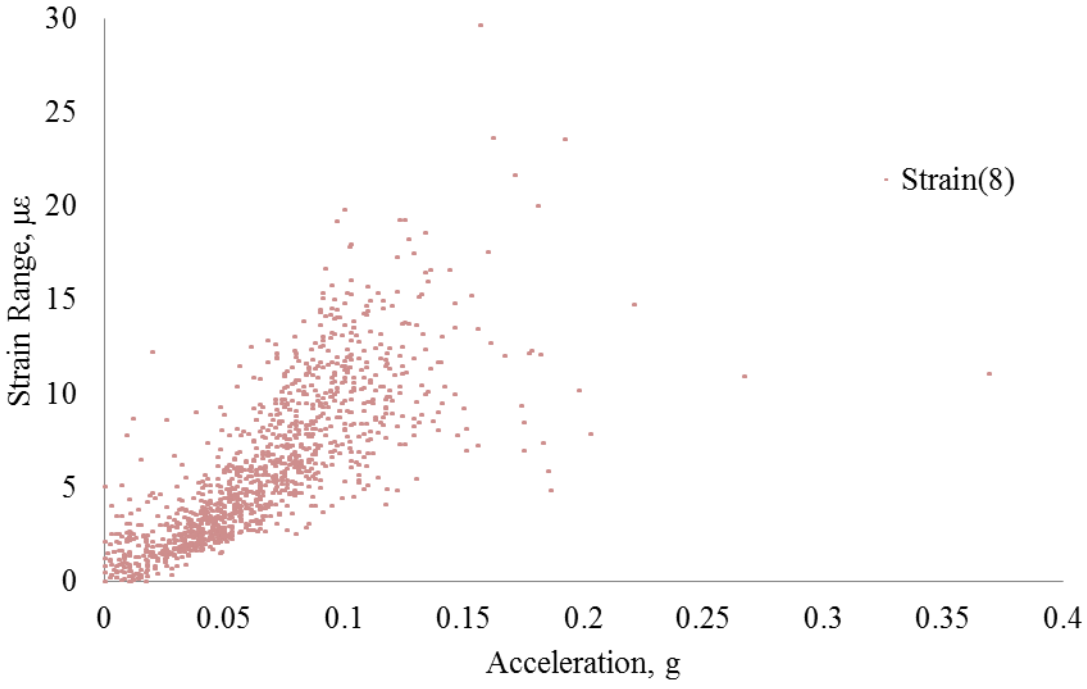


h) Strain gage 8

Fig. 66 Strain range vs. acceleration

Although truck-induced gusts cause structural vibration, the amplitude of the vibration is small. During the field monitoring, the maximum strain range from truck events was observed to be less

than 30 με (0.3 ksi). This indicates that truck-induced gusts do not excite the structure significantly and results in low strains and stresses.

### *6.2.3. Thermal effects*

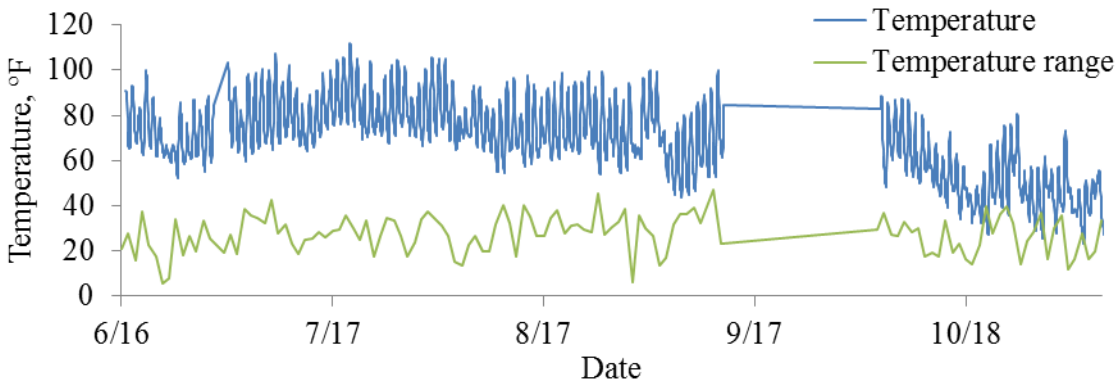


a) Temperature variation with time

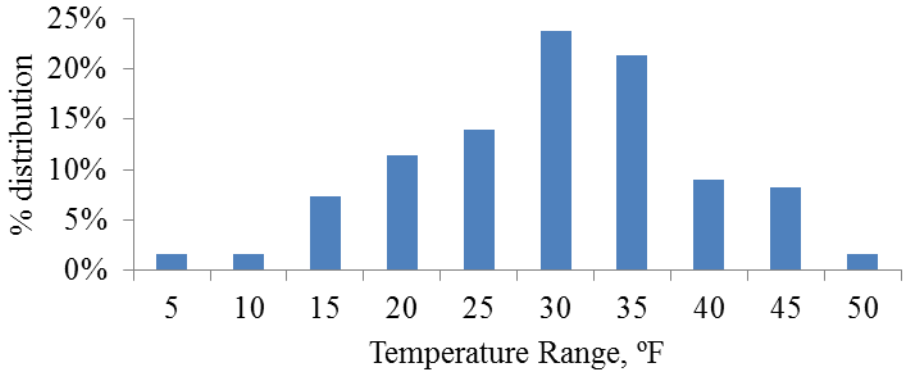


b) Temperature range histogram

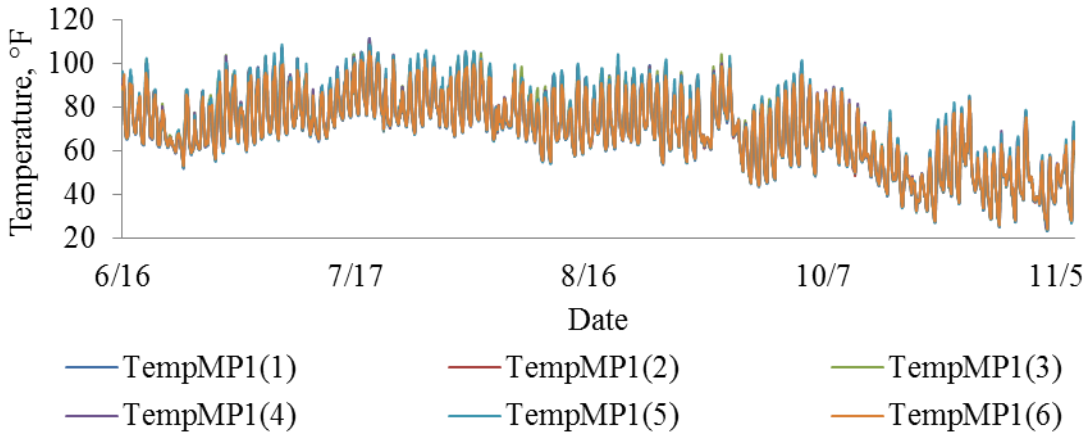


c) Temperature of six sensors

Fig. 67 Temperature records during field monitoring

Temperature and strain were measured by the vibrating-wire strain gages once per hour. The strain readings were converted to real strain (i.e., the strain resulting from restraint of

temperature induced expansion and contraction). The daily temperature ranges during the monitoring period varied from 4.3 to 48.7 °F. Figure 67 shows the temperature trend during the monitoring period. Data were not recorded for an unknown reason on June 30th and between September 12th and October 5th. A temperature range distribution is presented in Fig. 67b. Figure 67c shows that the temperature values at all six measured locations are very similar and indicates a generally uniform distribution. Figure 68 presents both strain and temperature showing that there is a strong relationship between them. As temperature increases, the strain increases.

The strain range in Fig. 69 shows a strong linear correlation with daily temperature range. A maximum real strain range (VW1 in the figure) was measured to be about 655 με (6.55 ksi) at a temperature range of 48.7 ºF.

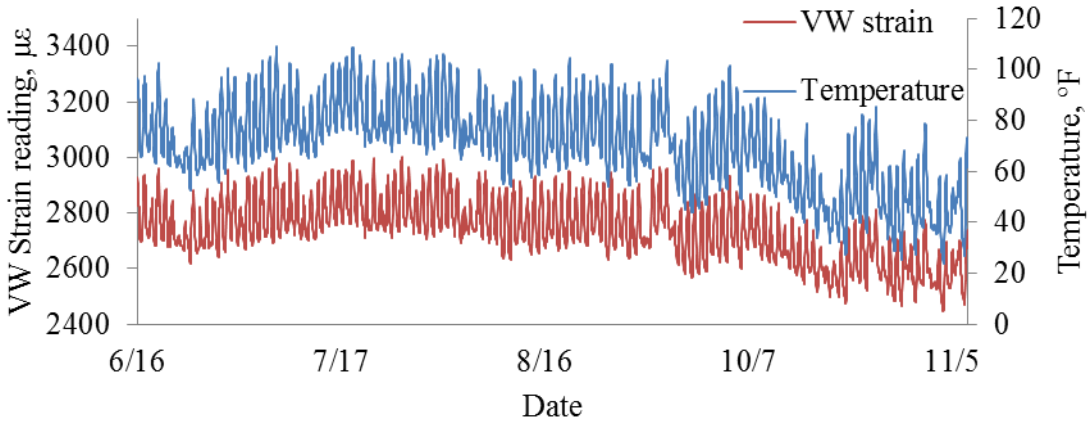


a) Temperature and VW strain fluctuation

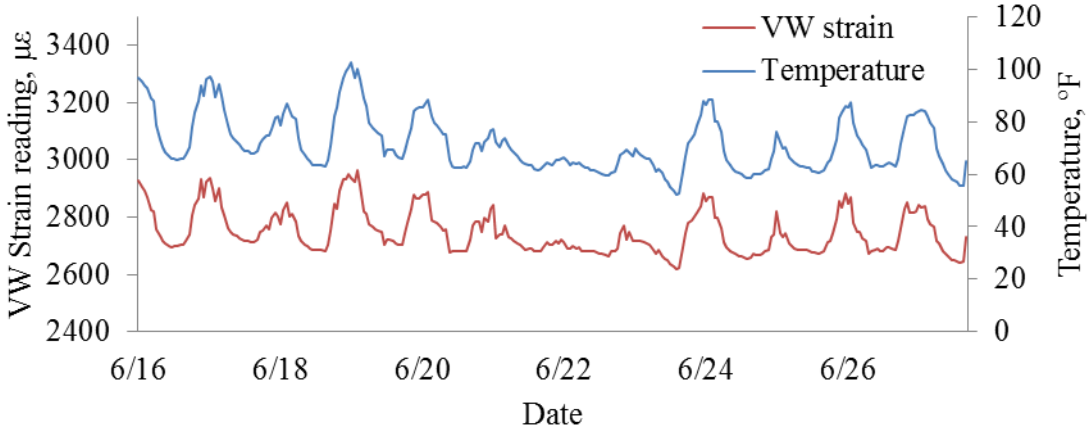


b) Detail display of the relation between temperature fluctuations to VW strain

Fig. 68 VW strain and temperature change during field monitoring

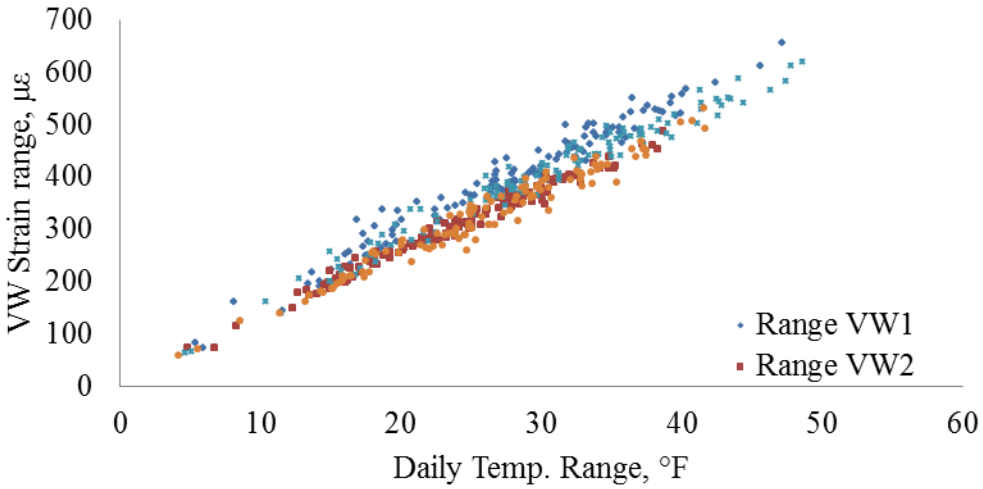


Fig. 69 Strain range during temperature change

### 6.3. Mathematical analysis of thermal effects on truss

It was observed that strain caused by restraining thermal expansion and contraction is much higher than that induced by wind gusts. A mathematical analysis was conducted to assess the thermal effects on the structure. The wind pressure is also analyzed in this section. In addition, stress results were evaluated to identify the members most impacted by thermal loading.

A basic mathematical analysis was performed to obtain thermal strain in the structure. For this analysis, the top support post was assumed to deflect in the horizontal direction due to the expansion of the truss structure. The deformed shape by thermal expansion is shown is Fig. 70. A thermal change 50 °F, which is close to the maximum range measured during the field monitoring, was applied to the structure.

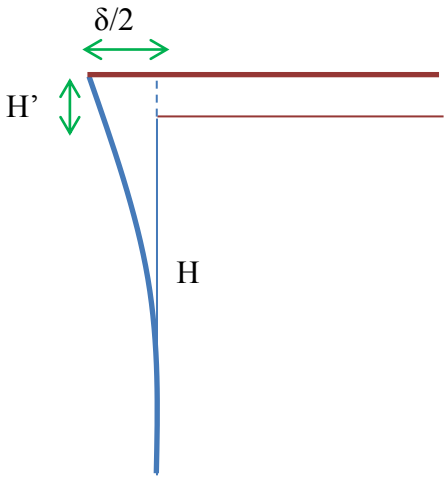


Fig. 70 Deformation of the support truss by thermal load

It is important to note that in the simple mathematical model (and all subsequent finite element analyses), the connection between the overhead truss to vertical support has been modeled as rigid. This modeling deviates from the Iowa DOT assumption that the upper chord connections

behave as tension only links. The horizontal deformation in the top truss generates axial force at both ends, which is defined as R. The total displacement in horizontal direction should consider the deformation by that due to restraint provided by the vertical end posts axial force and due to the temperature change. These two effects contribute to the total axial deformation as shown in equation 27:

$$\delta_T = L \times \alpha_T \times \Delta T - \frac{R \times L}{E_T \times A_T} \quad (27)$$

where, $\delta_T$ is the total elongation of truss, L is the length of truss, 70 ft, R is the axial force generated by the support post restraint, $E_T$ is the modulus of elasticity, $A_T$ is the cross section area of truss, $in^2$, and $\Delta T$ is daily temperature change.

The support posts are also influenced by the temperature range and the vertical elongation can be calculated using equation 27. Due to the symmetric geometry, the support posts at the other side would have same elongation.

$$H' = H \times \alpha_S \times \Delta T \quad (28)$$

where, H' is the elongated height of support after temperature change, H is the length of support, and $\alpha_S$ is the coefficient of thermal expansion.

The axial force caused by thermal expansion creates bending of the support post. The support deflection by the force can be obtained from equation 29:

$$|y| = \frac{R \times H'^3}{3 \times E_S \times I} \quad (29)$$

where, y is the bending displacement of the support posts, $E_S$ is the modulus of elasticity, and I is the moment of inertia.

Due to the symmetric condition, the displacement of support posts would be half of the total expansion of truss and determined by the following:

$$|y| = \frac{1}{2}\delta_T \quad (30)$$

Thus, the total strain of the truss is given in equation 31, which includes both thermal strain and axial normal strain:

$$\varepsilon = \frac{\delta_T}{L} = \alpha_T \times \Delta T - \frac{R}{E_T \times A_T} \quad (31)$$

Using equation 31, the total strain resulting from restraint of thermal expansion was estimated to be 654 με (6.54 ksi) in the chord members. This basic approach was compared with the field data and finite element modeling results as shown in next subsection.

### 6.4. Finite element modeling

It is difficult to predict the behavior of the welded joints since the geometry of the structure is complex. Thus, Finite Element (FE) modeling was used to analyze the behavior of the truss under thermal and wind loads. Two types of models were generated. In these models the truss structure was modeled using both beam and 3D solid models. The results from field monitoring and mathematical analysis were then compared with the numerical modeling. A truss structure tested at Purdue University, which had a different geometry than the one investigated as part of the long-term field monitoring study, was also analyzed.

### *6.4.1. Beam analysis*

Modal analysis and thermal analysis of the structures were performed using beam modeling. The vibration frequencies for the truss structure were obtained and detailed global response information was also obtained for thermal load condition.

The geometry of the structure used in the modeling was developed based upon the original design plans. Beam elements were created from point to point, therefore the interference between diagonals at junctions were ignored. The bottom plate of the support post was considered to be fixed. A mass element was coupled at mid span of the truss (weight of 4,116 lbs.) to simulate the weight of the DMS. Figure 71 shows the beam model.

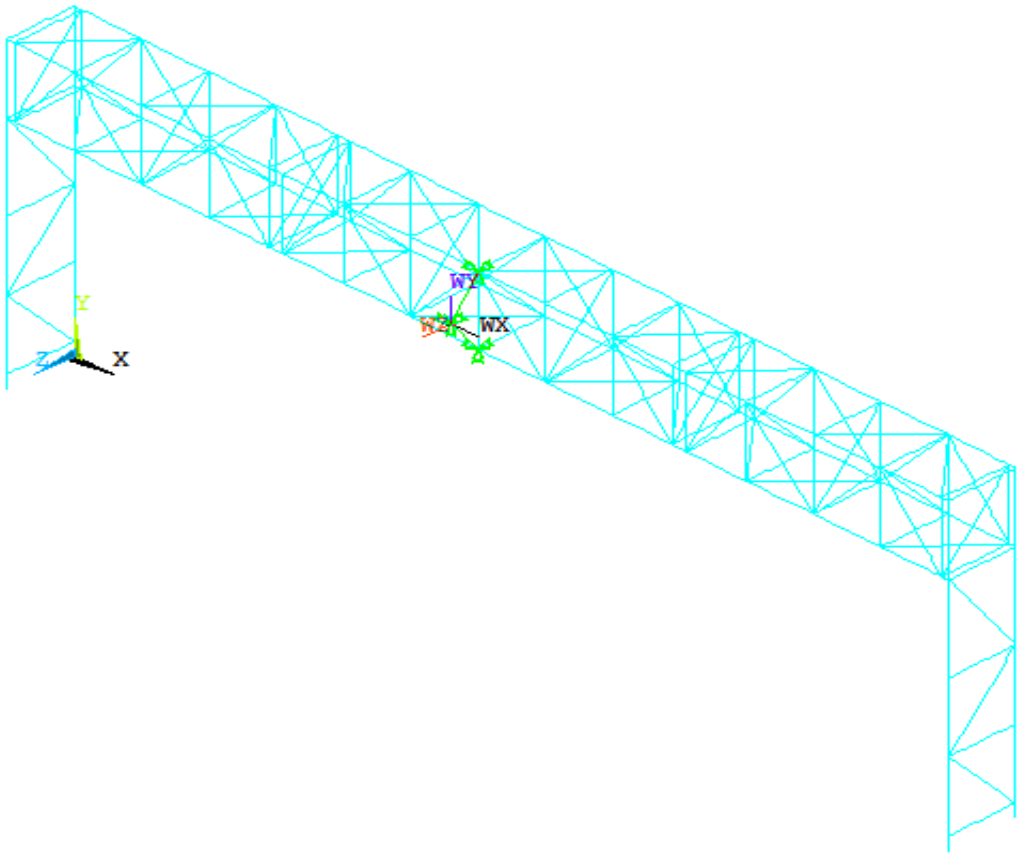


Fig. 71 Beam model in ANSYS

A modal analysis determines the vibration characteristics (natural frequencies and the corresponding mode shapes) of a structure. Figure 72 presents the natural frequencies in each mode obtained from modal analysis, where $f_{TR}$=2.7 Hz, $f_L$=4.0 Hz, $f_V$=5.2 Hz, and $f_T$=15.3 Hz (Table 19).

Table 19 compares the first four natural frequencies derived from analytical modeling and field data. As shown in the table, the natural frequencies from field test are in agreement with the results from modal analysis.

Table 19 Modal frequency and difference

| Mode | FEA, Hz | FFT, Hz | Difference, % |
|---|---|---|---|
| Transverse | 2.7 | - | - |
| Longitudinal | 4.0 | 4.0 | 0.3 |
| Vertical | 5.2 | 4.8 | 8.5 |
| Torsional | 15.3 | 14.9 | 2.8 |

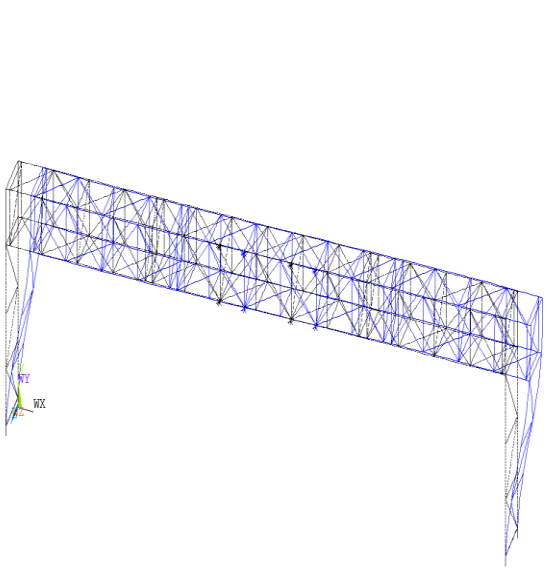

a) Transverse mode: 2.7 Hz

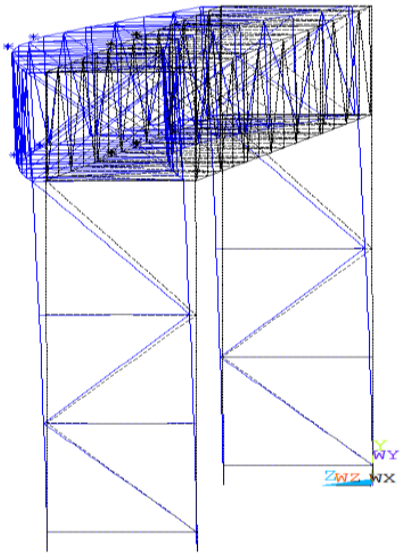

b) Longitudinal mode: 4.0 Hz

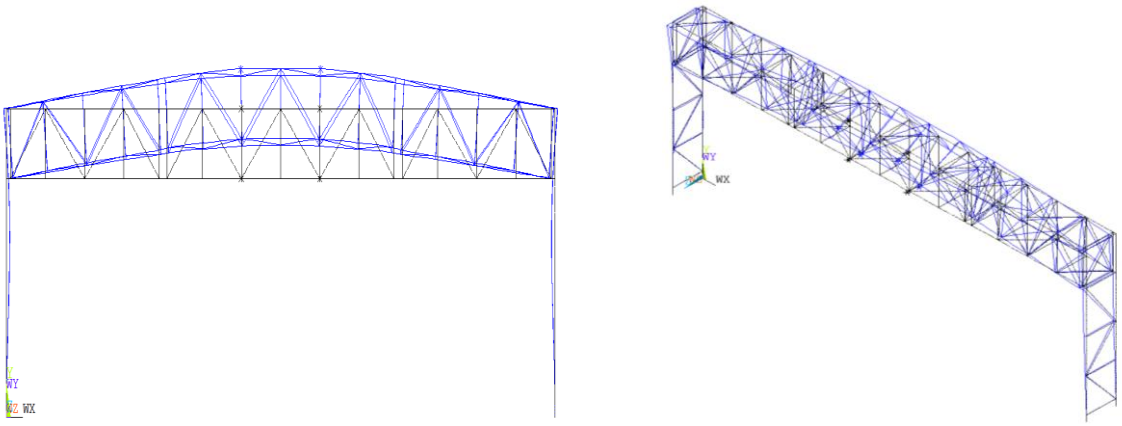

c) Vertical mode: 5.2 Hz d) Torsional mode: 15.3 Hz

Fig. 72 First four natural frequencies in various modes

A change in temperature of 50 °F, which is close to the maximum daily temperature range measured during the field monitoring, was applied to the overall structure in the beam model to study the response of the structure under thermal load. Figure 73 shows the resulting displaced shape.

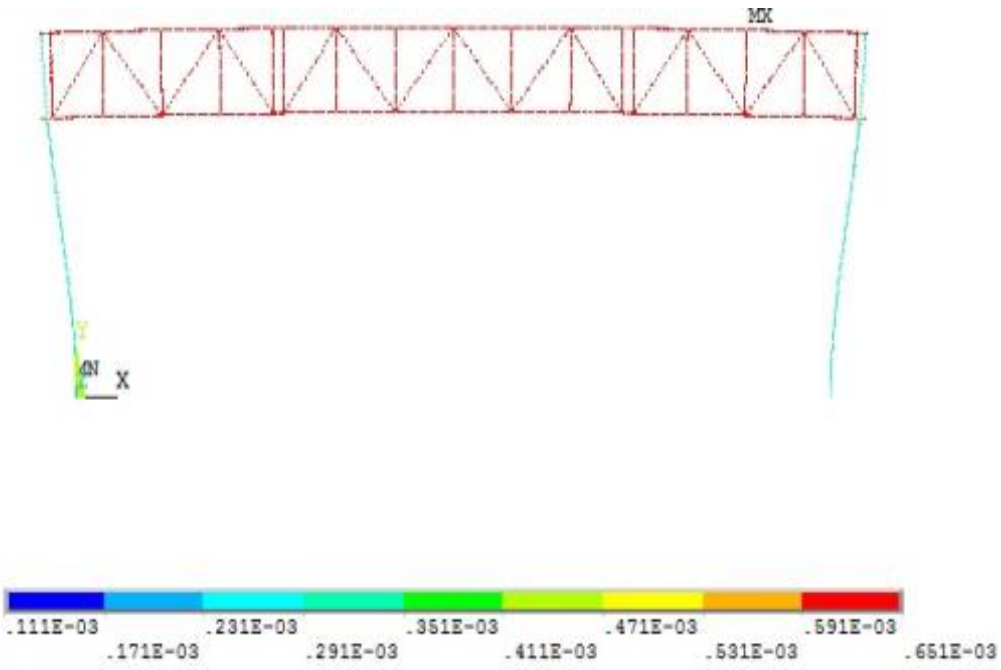


Fig. 73 Axial strain (με) due to thermal load

### *6.4.2. 3D solid analysis*

A 3D solid model was created to evaluate the detailed stress distribution in the structure. To obtain accurate stress-strain information and minimize computer data processing time, a balance of mesh size and element numbers is critical in modeling.

The geometry used in the solid modeling was generated to be as close as possible to the detail of the structure. Figure 74 shows the highly discretized model.

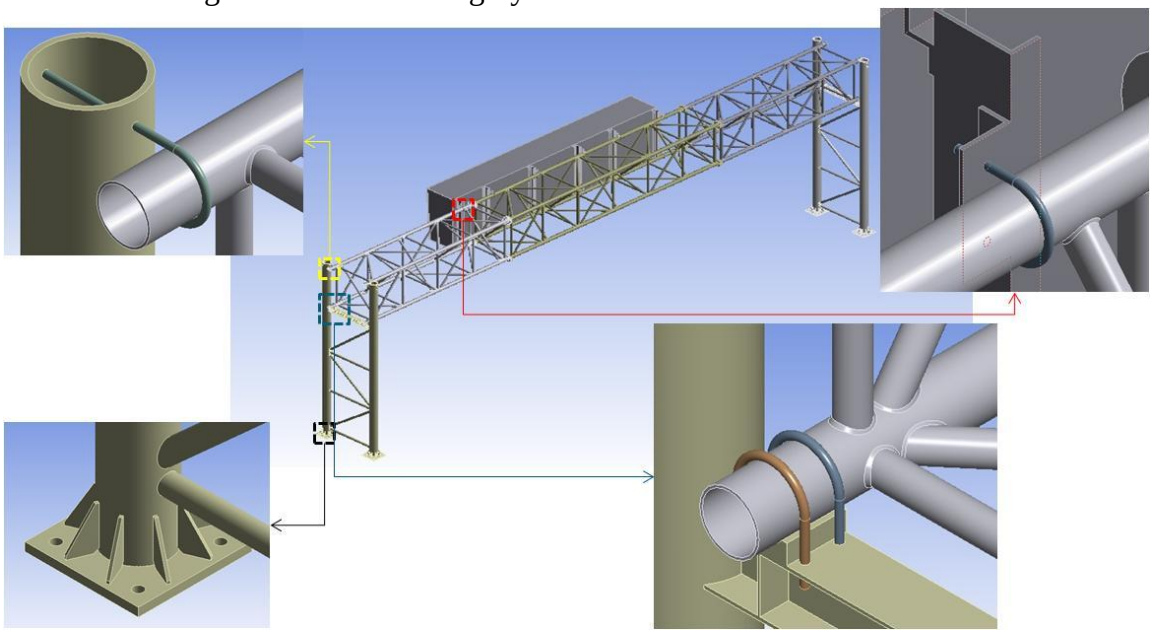

Fig. 74 Geometry of the Truss structure

A dimensional comparison between the lab structure that Purdue University tested and the one used for field monitoring in the present study is shown in Table 20. The main difference is the size of truss members.

Table 20 Comparison of structures' geometry

| | Field Monitoring Structure | Lab Structure |
|---|---|---|
| Post height | 27 ft | 26.5 ft |
| Post chord member | 10.75 in. dia. × 0.322 in. | 10 in. dia. × 0.375 in. |
| Post web member | 3.5 in. dia. × 0.216 in. | 2.75 in. dia. × 0.25 in. |
| Truss chord member | 6 in. dia. × 0.25 in. | 5 in. dia. × 0.322 in. |
| Truss web member ⊥ chord (inner) | 3 in. dia. × 0.25 in. | 1.75 in. dia. × 0.25 in. |
| Truss web member ⊥ chord (end) | 3 in. dia. × 0.25 in. | 2.5 in. dia. × 0.25 in. |
| Truss horizontal diagonal | 3 in. dia. × 0.25 in. | 2.75 in. dia. × 0.25 in. |
| Truss vertical diagonal | 3 in. dia. × 0.25 in. | 2.5 in. dia. × 0.25 in. |
| Truss internal diagonal | 3 in. dia. × 0.25 in. | 2 in. dia. × 0.25 in. |

Computer processing time is strongly related to the mesh density used in the modeling. Mesh density and mesh type also influence the accuracy of the results. A too fine mesh consumes extreme amounts of memory during data processing and leads to excessive calculation time while too coarse of a mesh might result in inaccurate results. A mixed mesh density is beneficial

because a finer mesh is used in the area where higher stresses occur and a coarser mesh can be used at insignificant areas. Figure 75 shows the mesh of the entire structure and provides a good example of how a fine mesh was used in critical regions where higher stress was expected.

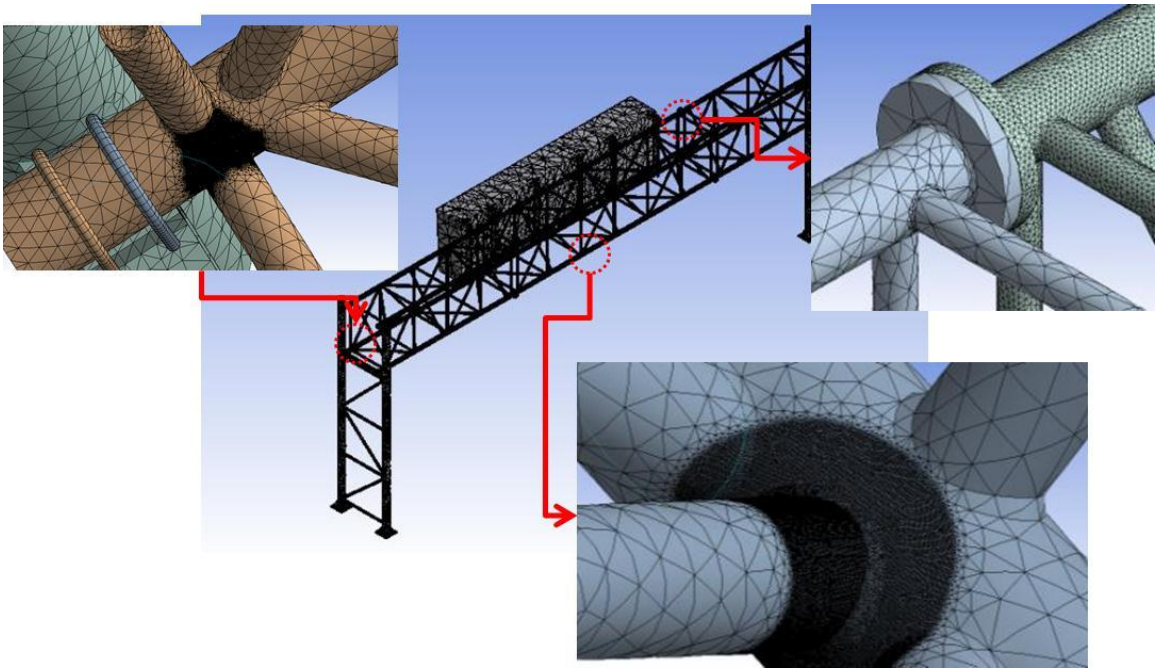

Fig. 75 Mesh of the structure

The suggested mesh size for fatigue analysis is 1 mm (Schoenborn, 2006). In this study, the structure has span of 70 ft and height of 27 ft, which is extremely large compared to suggested mesh size. Sub-modeling (see Fig. 76) is a useful technique in this case to fulfill the mesh size requirement and overall skewness target.

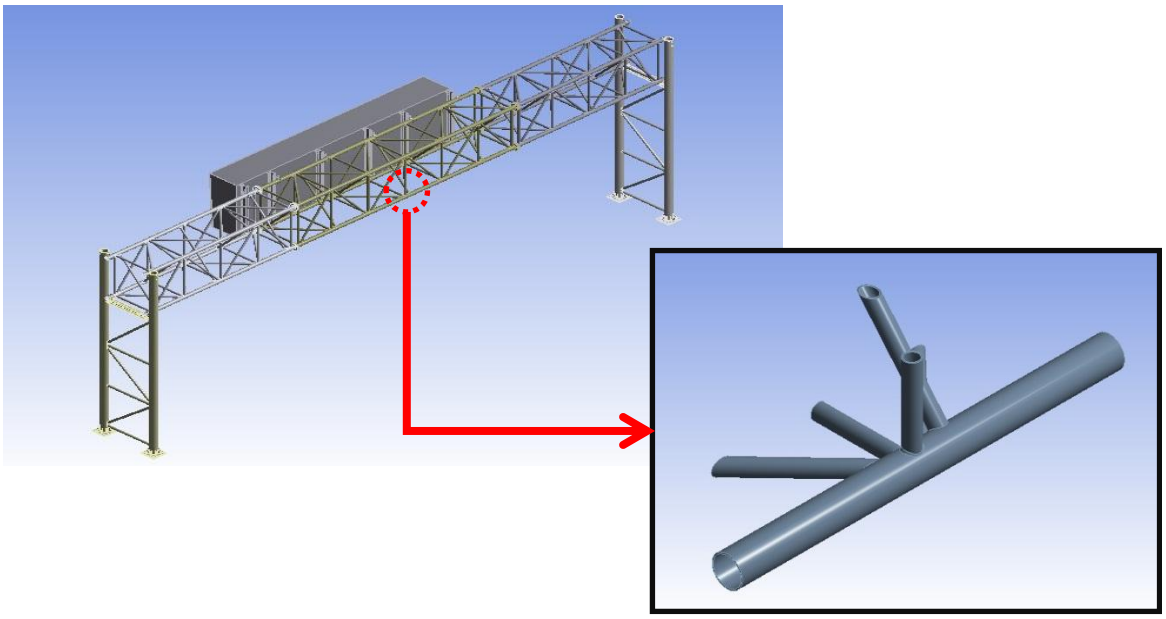

Fig. 76 Sub-model from the global structure

The analytical thermal strain and normal strain are shown in Figs. 77 and 78. Thermal strain is only related to the temperature load and the thermal expansion coefficient, and it is consistent in the truss and support post as shown in Fig. 77.

The strain values from field monitoring, beam model and 3D solid model are compared in Table 21. Note that none of the analytical modeling addressed the issue of members being in the sun and/or shade. Rather, it has been assumed that the members are responding to changes in ambient air temperature only. The values from finite element modeling are measured near strain gages. Vibrating-wire strain gages 3 and 4 were found to have malfunctioned; therefore they are not used in the table. The strain values from modeling are close to the field data as shown in Table 21.

Table 21 Strain (με) comparison among field data, beam model and solid model

| Number of VW sensor | Field value | Mathematical | | ANSYS APDL | | ANSYS Workbench | |
|---|---|---|---|---|---|---|---|
| | | Value | Difference | Value | Difference | Value | Difference |
| 1 | 684.7 | 654 | -4.48% | 677.1 | -1.11% | 665.5 | -2.80% |
| 2 | 609 | 654 | 7.39% | 618 | 1.48% | 622.6 | 2.23% |
| 3 | - | 654 | - | 616.9 | - | 624.3 | - |
| 4 | - | 654 | - | 677.6 | - | 658 | - |
| 5 | 636.6 | 654 | 2.73% | 642 | 0.85% | 656 | 3.05% |
| 6 | 608.4 | 654 | 7.50% | 637.8 | 4.83% | 650 | 6.84% |

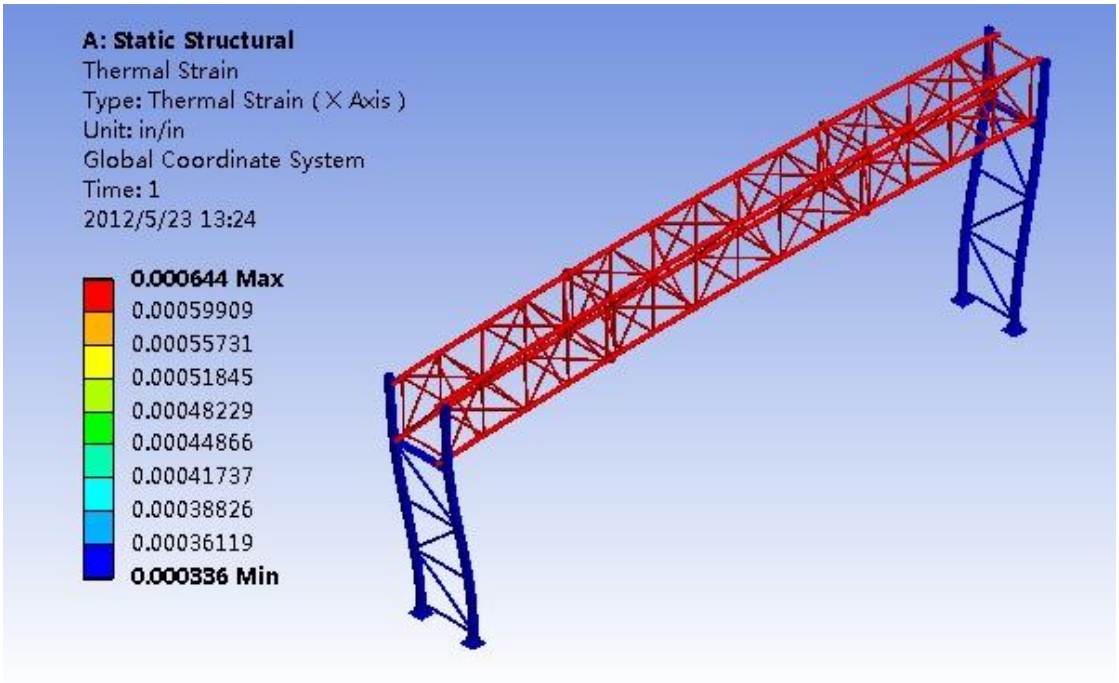


Fig. 77 Thermal strain (ε) in solid model

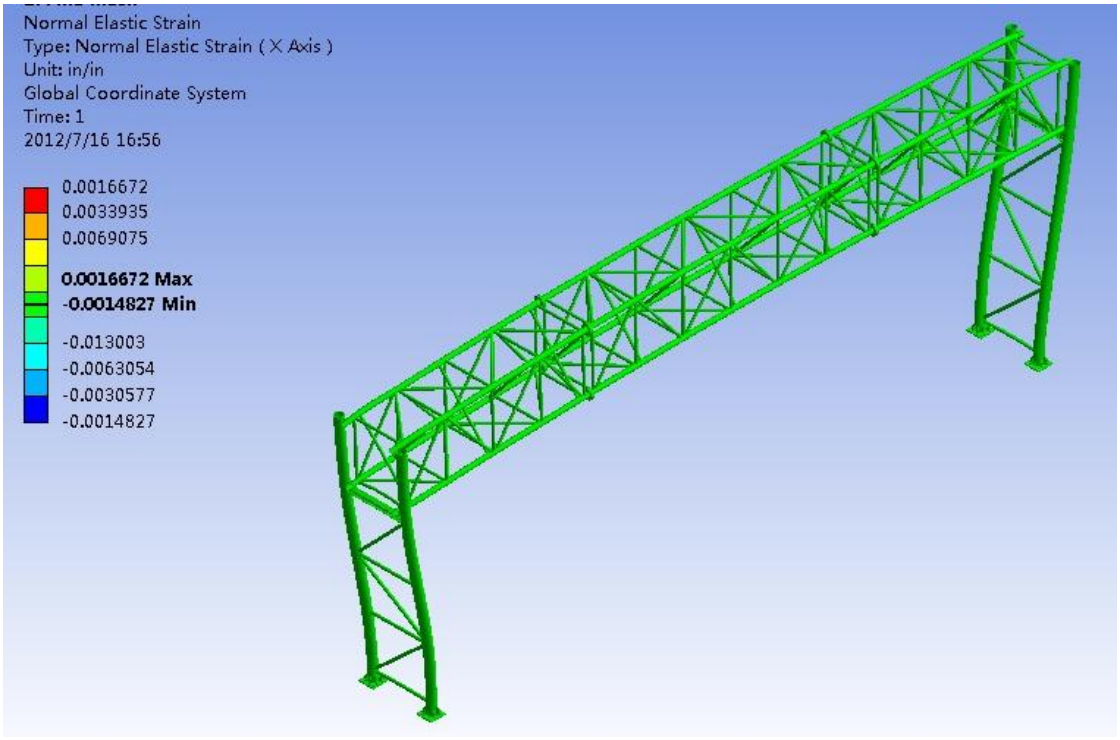


Fig. 78 Normal strain (ε) in solid model

### *6.4.3. Extreme thermal conditions on field-monitoring structure*

During field monitoring, the maximum and minimum temperatures were measured to be 111.7 ºF and 23.3 ºF, respectively and wind speed reached 32.93 mph at a maximum. The maximum and minimum temperatures in Ames, Iowa for the last 10 years prior to 2011 were 100 ºF and -31 ºF, respectively according to Weather Underground (2012.)

For these types of extreme thermal conditions, finite element analysis was used and Fig. 79 shows part of the truss with numbers of the welded joints. As before, the extreme thermal condition case was evaluated without consideration of direct sun/shading impacts. Rather, it was assumed that the truss responded to ambient thermal changes. Table 22 lists the maximum equivalent stress with corresponding joint numbers for the extreme thermal condition observed on the structure during the field monitoring campaign. The maximum stress was found to be 13.4 ksi at the horizontal web member at the end of the truss when an extreme condition of -31 ºF (Δ102.6 ºF) was applied based on a reference temperature of 71.6 ºF. The modeling results were derived from coarse mesh and the results from coarse mesh were used to find out the most critical regions where high stress occurs. Based on the stress results from coarse mesh, a submodel with finer mesh was developed to obtain more accurate stress results. The submodel was created focusing on the welded joints where the highest stresses occurred (see Fig. 80) The stress reaches 20.8 ksi at -31 ºF (Δ102.6 ºF) with a reference temperature of 71.6 ºF. The stress is higher than the yield stress of 20 ksi at welded joints defined in the AASHTO standards.

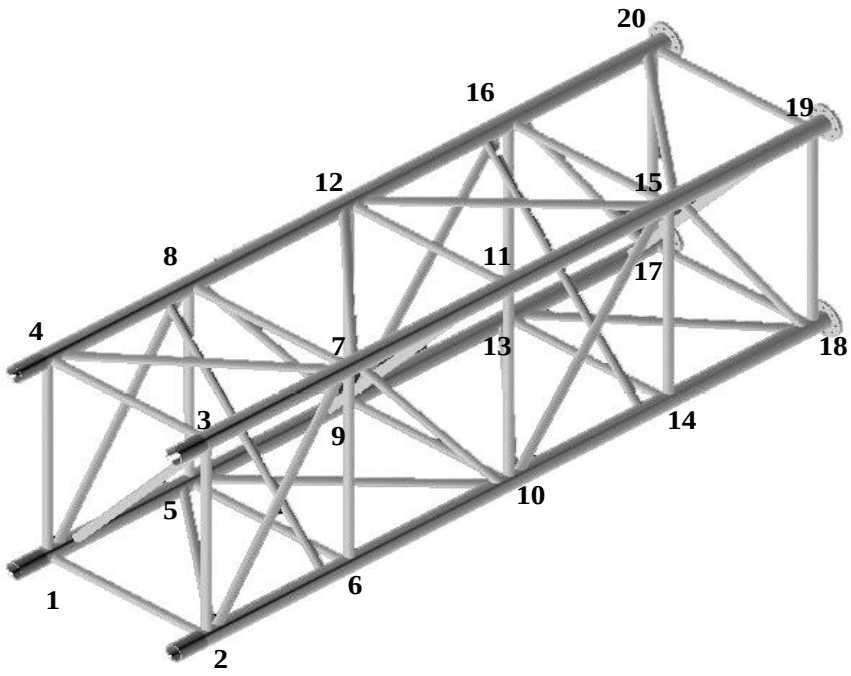


Fig. 79 Numbers of the welded joints

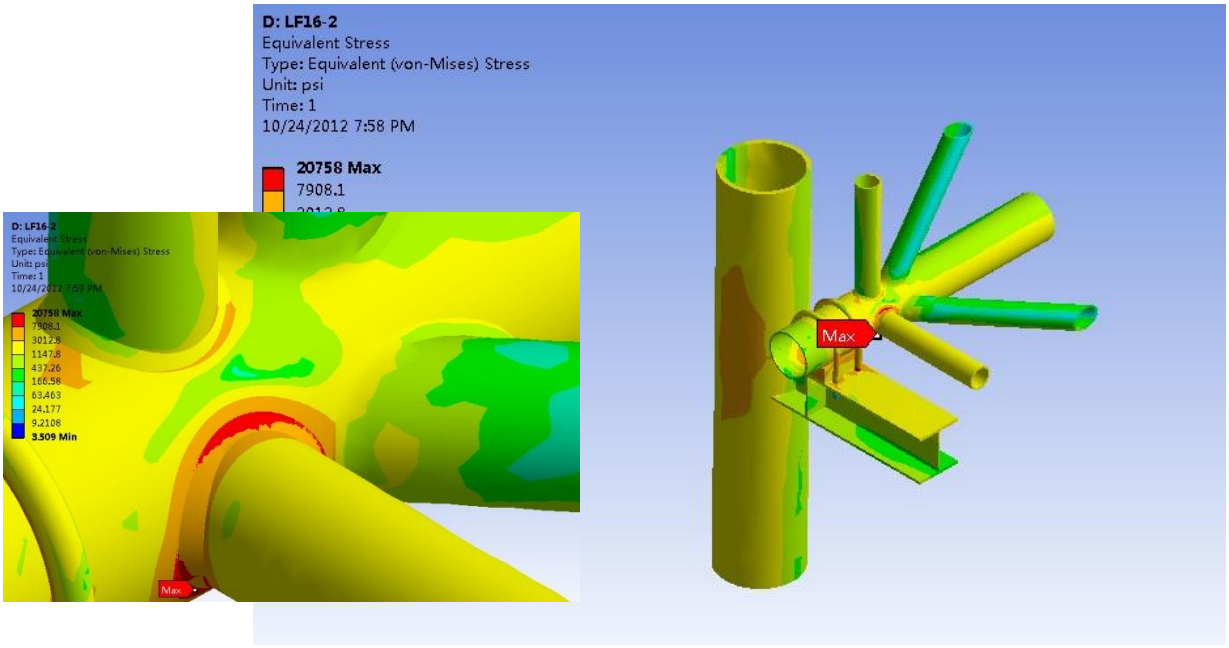


Fig. 80 The maximum stress area and detail view in submodel

Table 22 Maximum stress values of coarse mesh with coordination in drawing

| No. | X, in. | Y, in. | Z, in. | Stress (psi) |
|---|---|---|---|---|
| 1 | 11.94 | 244.05 | 835.84 | 13,444 |
| 2 | 68.29 | 243.85 | 836.16 | 12,718 |
| 3 | 72.36 | 316.58 | 835.09 | 4,877.5 |
| 4 | 8.56 | 315.37 | 834.38 | 4,720.6 |
| 5 | 11.43 | 248.35 | 780.73 | 1,497.6 |
| 6 | 67.04 | 246.49 | 782.06 | 1,971.4 |
| 7 | 69.53 | 315.04 | 782.15 | 1,112.8 |
| 8 | 13.00 | 318.00 | 777.82 | 1,431.8 |
| 9 | 13.00 | 246.00 | 717.82 | 2,091.2 |
| 10 | 70.00 | 249.00 | 717.84 | 1,378.1 |
| 11 | 67.04 | 318.47 | 717.76 | 1,072.8 |
| 12 | 7.08 | 318.69 | 720.02 | 717.62 |
| 13 | 7.69 | 244.09 | 647.49 | 1,219 |
| 14 | 67.04 | 245.51 | 657.77 | 2,191.3 |
| 15 | 70.00 | 315.00 | 657.98 | 1,164.9 |
| 16 | 12.96 | 317.53 | 662.24 | 1,317.3 |
| 17 | 12.96 | 245.51 | 607.98 | 2,002.9 |
| 18 | 70.56 | 243.05 | 614.71 | 1,227.7 |
| 19 | 67.04 | 318.49 | 607.98 | 754.48 |
| 20 | 9.45 | 320.69 | 614.68 | 1,377 |

Fabrication error was also considered in modeling. Misalignment of the diagonal members would be the primary one since internal diagonal members on the chord are typically welded manually as the last stage of the structure assembly. In case the member was shorter or longer, it would be slightly adjusted to fit in the structure. Two types of misalignments were simulated as shown in Fig. 81: the misalignment of the diagonal member and the misalignment of the vertically inclined member at the end of truss. Maximum stresses by possible misalignment for a temperature range of 50°F are listed in Table 23.

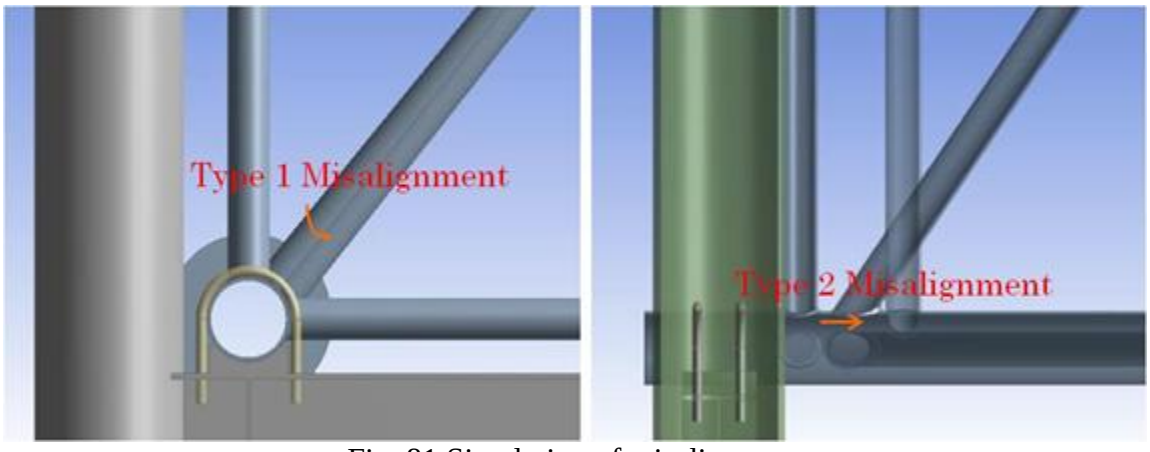

Fig. 81 Simulation of misalignment

In addition, two different type of welding shapes were considered including a chamfer shape and a blend shape. The sizes of the shape were also varied as listed in Table 23. Figure 82 shows the shape of the resulting welds.

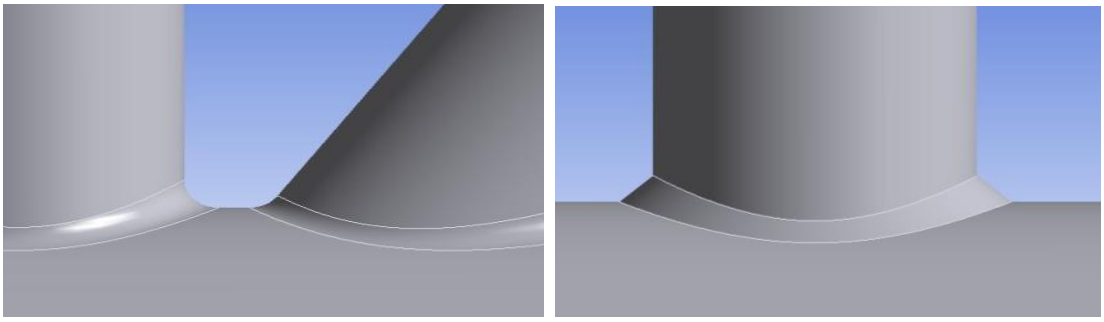

a) Chamfer b) Blend

Fig. 82 Type of welding

The results from these simulations are shown in Table 23. All results were obtained in 0.6 inch mesh size and for a temperature range of 50°F.

Table 23 Maximum stress from simulations

| Other Simulation at Δ50ºF | Max Stress (psi) | Difference | CPU time (s) |
|---|---|---|---|
| 0.3125 in Chamfer | 9,055.9 | 0.00% | 15,057 |
| 0.4 in Chamfer | 9,182.7 | 1.40% | 15,109 |
| 0.2 in Chamfer | 9,293.8 | 2.63% | 15,304 |
| 0.3125 in Blend | 9,285.9 | 2.54% | 14,676 |
| 0.4 in Blend | 9,033.5 | -0.25% | 15,036 |
| 0.4 in type 1 misalignment, 0.3125 in Chamfer | 9,064.8 | 0.10% | 14,992 |
| 1 in type 1 misalignment, 0.3125 in Chamfer | 9,026.3 | -0.33% | 15,185 |
| 0.5 in type 2 misalignment, 0.3125 in Chamfer | 9,060.0 | 0.05% | 14,762 |
| 1 in type 2 misalignment, 0.3125 in Chamfer | 9,214.6 | 1.75% | 14,769 |
| 0.4*0.3 in Chamfer | 9,084.5 | 0.32% | 15,110 |
| 0.3*0.4 in Chamfer | 9,097.1 | 0.45% | 14,723 |

According to the inspection conducted by Purdue University (Bowen Laboratory, 2011), it was found that a diagonal member was not merging well with chord members and a gap of approximately 0.0051 in was estimated. A simulation of the gap was performed as shown in Fig. 83. The stress at the welded area in diagonal members was obtained in both solutions, with and without gravity. 4.4 ksi and 8.6 ksi of maximum stress were found in the situations without and with gravity, respectively as shown in Fig. 84.

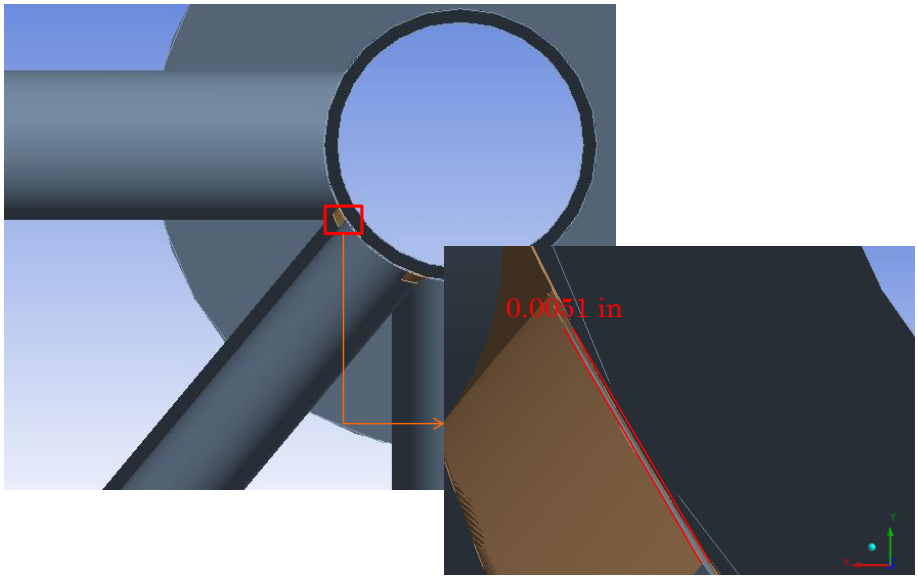


Fig. 83 Gap simulation

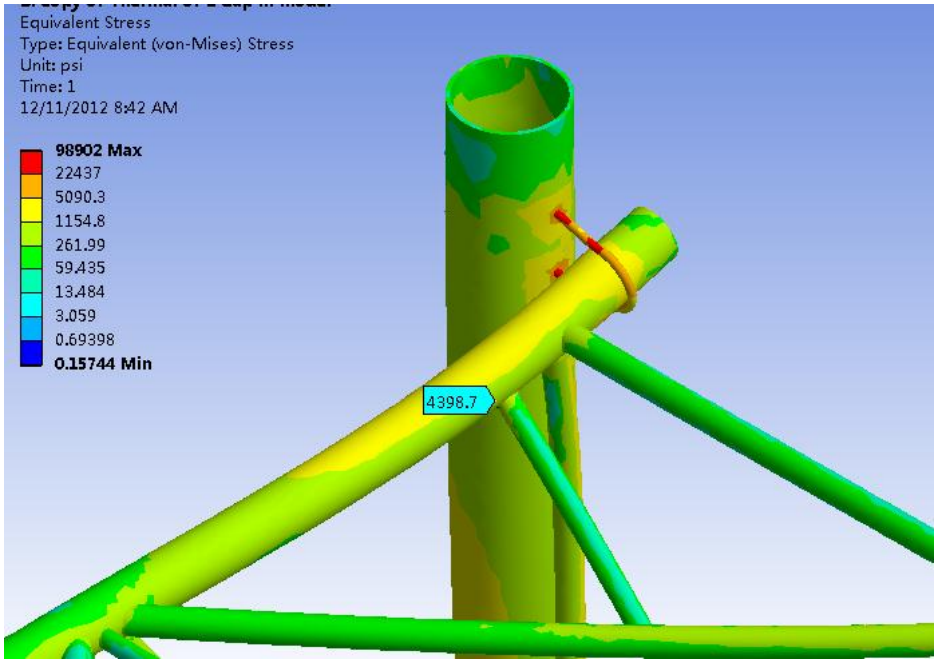


a) Without gravity

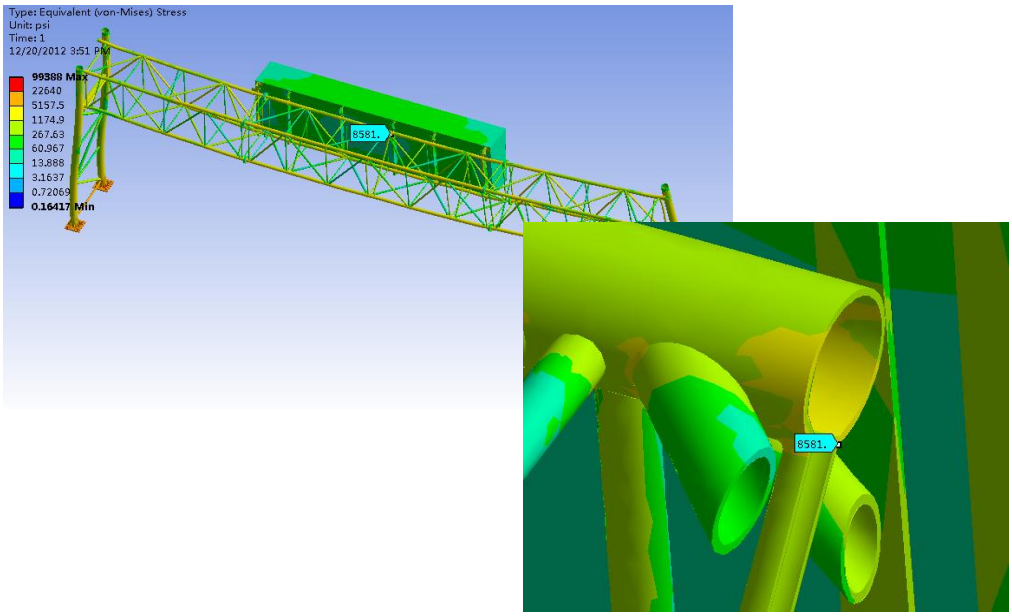


b) With gravity

Fig. 84 Maximum stress on diagonal welding

### *6.4.4. Extreme thermal conditions on the lab structure*

The same extreme thermal conditions were applied to the lab structure. In the thermal loads of -31 ºF (Δ 102.6 ºF), the maximum stress was found to be 26.4 ksi at the same location identified in the Ames truss (see Fig. 85). The stress is higher than the one for the field structure because the diameters of the truss members in lab the structure are smaller than the one in the field structure.

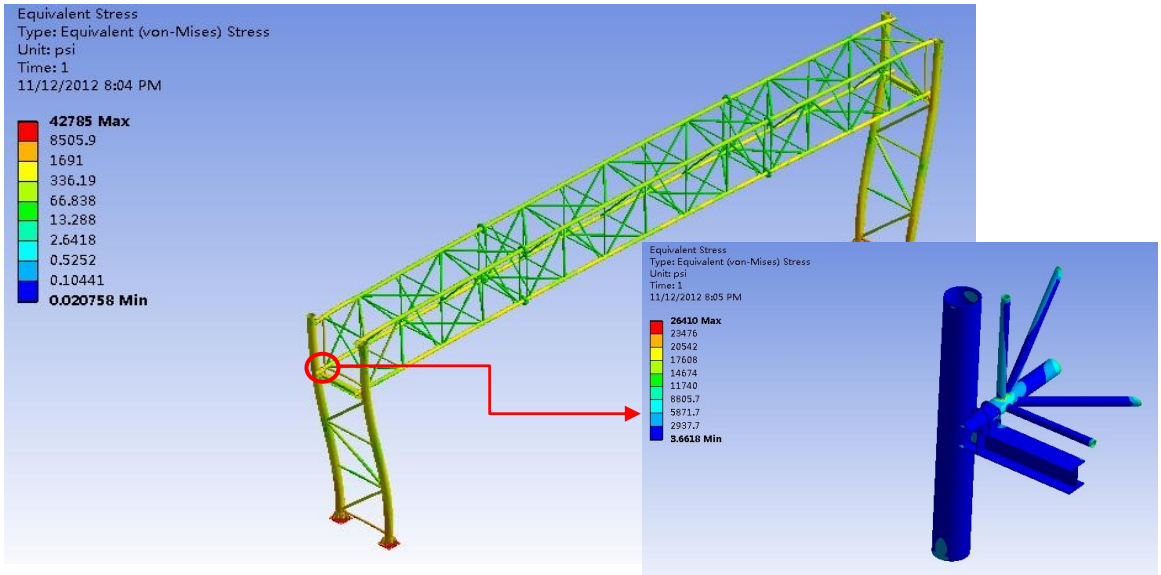


Fig. 85 Extreme thermal load on lab structure

### 6.5. Fatigue analysis of field-monitoring structure

To further understand the long term thermal effect on structural life, a fatigue analysis was also performed for the Ames truss. Fatigue is the progressive and localized structural damage due to cyclic loading. The stress amplitude has a strong relation with the fatigue life, known as S-N curve. The fatigue life of a structure can be estimated based on the stress amplitude along with appropriate S-N curves.

A typical relationship commonly used for fatigue life estimation is expressed in equation 32:

$$N_f = C_f S_R^{-1/m} \tag{32}$$

where, $N_f$ is the number of cycles to failure, $C_f$ and m are constants dependent on the material and weld detail, and $S_R$ is constant amplitude stress range.

$C_f$ and m of the specified S-N curves for fatigue categories A to ET can be obtained from the LRFD Bridge Code (AASHTO, 2004). The corresponding constant amplitude fatigue limit (CAFL) can be found in the Standard Specification for Structural Supports for Highway Sign, Luminaires and Traffic Signals (AASHTO, 2010). $C_f$ and m for category ET can also be obtained from Huckelbridge and Metzger (Huckelbridge and Metzger, 2007) with analytical curves, where Cf = 1.17E+07 (cycles/ ksi1/m) and m = 0.304. An S-N curve is then plotted based on the information from above table (see Fig. 86).

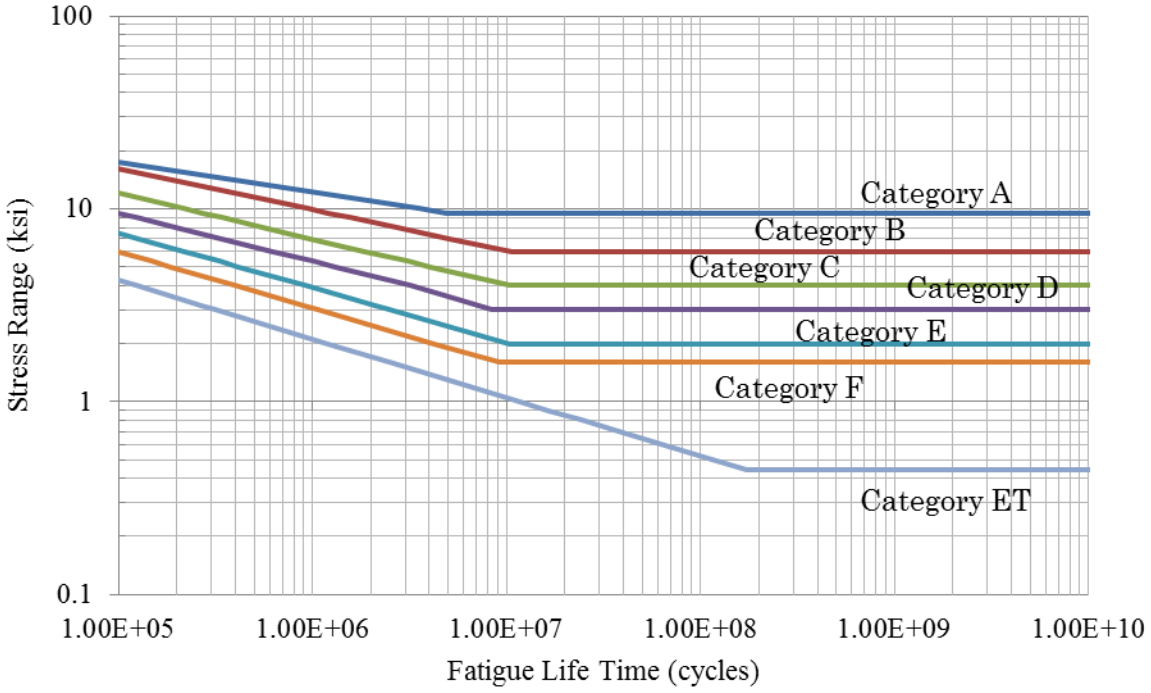


Fig. 86 Extrapolated S-N Curve for Fatigue Categories for Aluminum

For metallic materials, an increasing mean stress value induces decreasing fatigue resistance (Bannantine et al., 1990). The specified stress ranges in the codified S-N curves assume a Zero Mean Stress. However, in practical conditions, the mean stress is not always zero. In this study, due to the influence of the heavy weight of the DMS, the truss structure holds an initial stress due to the self-weight. As a result an adjusted stress level is needed. The stress range values are obtained from the 3D solid model, and the adjusted stress level according to Goodman relation, Gerber relation, and modified Goodman relation are listed in Table 24. Soderberg relation was chosen to adjust the stress range for a non-zero mean stress since it is the most conservative.

Table 24 Zero-mean stress from common relations

| Joint No. | 1 | 2 | 3 | 4 | 5 | 6 | 7 | 8 | 9 | 10 | 11 | 12 | 13 | 14 | 15 | 16 | 17 | 18 | 19 | 20 |
|---|---|---|---|---|---|---|---|---|---|---|---|---|---|---|---|---|---|---|---|---|
| Mean Stress (ksi) | 2.2 | 2.0 | 0.1 | 2.9 | 1.3 | 0.5 | 2.6 | 7.2 | 2.3 | 1.0 | 0.7 | 0.7 | 0.6 | 0.9 | 2.2 | 2.1 | 2.9 | 2.0 | 1.4 | 2.4 |
| Stress Δ50°F (ksi) | 10.1 | 9.6 | 3.7 | 3.6 | 1.1 | 1.5 | 0.8 | 1.1 | 1.6 | 1.0 | 0.8 | 0.5 | 0.9 | 1.6 | 0.9 | 1.0 | 1.5 | 0.9 | 0.6 | 1.0 |
| Goodman | 11.1 | 10.4 | 3.7 | 4.0 | 1.2 | 1.5 | 0.9 | 1.5 | 1.7 | 1.1 | 0.8 | 0.6 | 0.9 | 1.7 | 1.0 | 1.1 | 1.7 | 1.0 | 0.6 | 1.1 |
| Gerber | 10.2 | 9.6 | 3.7 | 3.6 | 1.1 | 1.5 | 0.8 | 1.2 | 1.6 | 1.0 | 0.8 | 0.5 | 0.9 | 1.7 | 0.9 | 1.0 | 1.5 | 0.9 | 0.6 | 1.0 |
| Soderberg | 11.3 | 10.6 | 3.7 | 4.1 | 1.2 | 1.5 | 1.0 | 1.7 | 1.8 | 1.1 | 0.8 | 0.6 | 0.9 | 1.7 | 1.0 | 1.1 | 1.8 | 1.0 | 0.6 | 1.2 |

Stress value obtained from 3D submodeling was used for the fatigue analysis. A linear correlation was found for the stress value and temperature range. Table 25 lists the results from 3D modeling, and Fig. 87a shows the trend of the stress versus temperature range, where solid symbols represent the results from modeling while "X"s represent the extrapolated values. Figure 87b represents the percentage of temperature range with an interval of 5 ºF. A complete stress range with an interval of 5 ºF is shown in Table 26.

Table 25 Stress range in complete temperature range spectrum

| Temperature °F | 10 | 20 | 30 | 40 | 50 | 102.6 |
|---|---|---|---|---|---|---|
| Stress (ksi) | 2.02 | 4.05 | 6.07 | 8.09 | 10.12 | 20.76 |

Miner's rule, as a useful approximation for fatigue life estimation, is employed in this study (Stephens and Fuchs, 2001):

$$\sum_{i=1}^{k} \frac{n_i}{N_i} = C \tag{33}$$

where, k is number of different stress magnitudes in a spectrum, $N_i$ is the number of cycles to failure of a constant stress range, and $n_i$ is the contribution in the constant stress range.

For design purposes, C is assumed to be 1. The equation can be transformed to obtain the structure fatigue life:

$$N_f = \frac{1}{\sum_{i=1}^{k} \frac{P_i}{N_i}} \tag{34}$$

where, $N_f$ is the estimated structure fatigue life, k is number of different stress magnitudes in a spectrum, $N_i$ is the number of cycles to failure of a constant stress range, and $p_i$ is the percentage of the certain stress in spectrum.

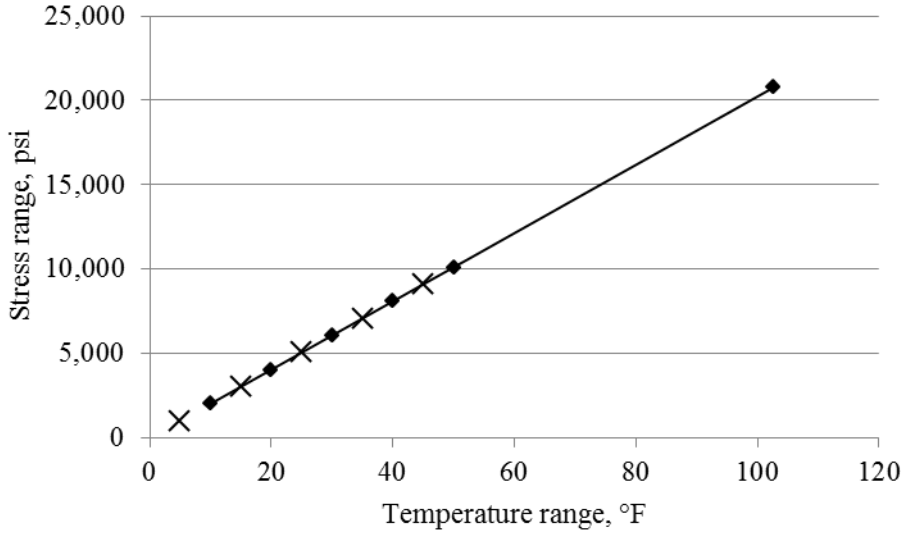


a) Analytical curve of stress range to temperature range

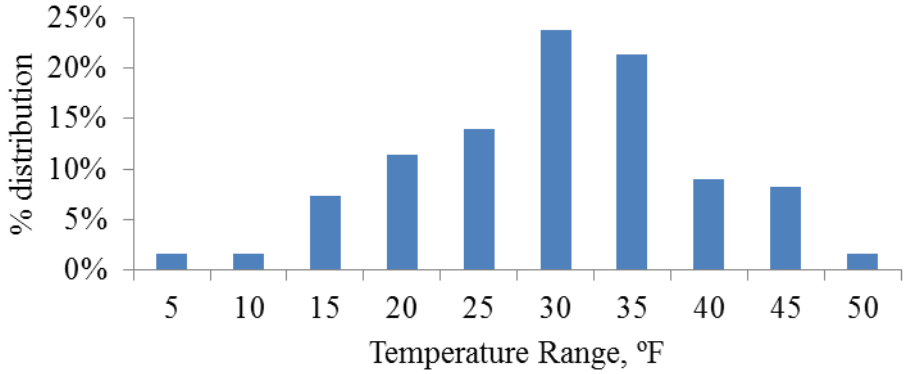


b) Temperature range histogram

Fig.87 Temperature range used for fatigue analysis

The estimated fatigue life based on thermal load and self-weight is shown in Table 27. The fatigue life was estimated to be 44 years. Other loads such as wind loads or truck-induced gust will also contribute to the actual fatigue life. Therefore the overall fatigue life would likely to be less than 44 years.

The following conclusions can be drawn based on the long-term monitoring data and the FE modeling:

- For the overhead truss structure used in field monitoring, the strain range caused by truck induced gust was less than 30 με while (0.3 ksi) the daily temperature range of Δ50ºF induced strain of approximately 650 με (6.5 ksi).

- A stress range up to 10.1 ksi was observed for temperature range of Δ50 ºF. The highest stress on the truss occurred at the horizontal member at end of the truss and at the tube-to-tube welded area.

- Weather Underground reports a lowest temperature at the Ames location of-31 ºF (Δ 102.6 ºF) for the last 10 years. The maximum stress was found to be 20.8 ksi in the horizontal member at the end of the truss with an extreme thermal condition resulting from a temperature change of 102.6 ºF. This is higher than the yield stress of Aluminum T-6061 welding material (20 ksi) defined by AASHTO standards.

- Fatigue life is estimated to be 44 years with only thermal load cycles and self-weight.

- The lab structure that Purdue University evaluated was also simulated. With an extreme thermal load of -31 ºF (Δ 102.6 ºF), the maximum stress is found to be 26.4 ksi at the horizontal member at the end of truss.

- There was no high stress on diagonal members while the most of failures occurred at the web diagonal welding joints according to the inspection report by Iowa DOT.

- Although inconclusive here, it is believed that fabrication may play an important role in the development of fatigue cracks. However, given the variety of different fabrication styles and potential fabrication errors, there are likely multiple causes for the development of cracks.

Table 26 Stress range in Δ 5°F interval

| Joints No. | Stress, ski | | | | | | | | | |
|---|---|---|---|---|---|---|---|---|---|---|
| | 50°F | 45°F | 40°F | 35°F | 30°F | 25°F | 20°F | 15°F | 10°F | 5°F |
| 1 | 11.34 | 10.21 | 9.07 | 7.94 | 6.8 | 5.67 | 4.54 | 3.4 | 2.27 | 1.13 |
| 2 | 10.6 | 9.54 | 8.48 | 7.42 | 6.36 | 5.3 | 4.24 | 3.18 | 2.12 | 1.06 |
| 3 | 3.69 | 3.32 | 2.95 | 2.58 | 2.21 | 1.84 | 1.47 | 1.11 | 0.74 | 0.37 |
| 4 | 4.15 | 3.73 | 3.32 | 2.9 | 2.49 | 2.07 | 1.66 | 1.24 | 0.83 | 0.41 |
| 5 | 1.21 | 1.09 | 0.97 | 0.84 | 0.72 | 0.6 | 0.48 | 0.36 | 0.24 | 0.12 |
| 6 | 1.52 | 1.37 | 1.22 | 1.06 | 0.91 | 0.76 | 0.61 | 0.46 | 0.3 | 0.15 |
| 7 | 0.96 | 0.86 | 0.77 | 0.67 | 0.58 | 0.48 | 0.38 | 0.29 | 0.19 | 0.1 |
| 8 | 1.68 | 1.51 | 1.34 | 1.18 | 1.01 | 0.84 | 0.67 | 0.5 | 0.34 | 0.17 |
| 9 | 1.78 | 1.6 | 1.42 | 1.24 | 1.07 | 0.89 | 0.71 | 0.53 | 0.36 | 0.18 |
| 10 | 1.09 | 0.98 | 0.87 | 0.76 | 0.66 | 0.55 | 0.44 | 0.33 | 0.22 | 0.11 |
| 11 | 0.83 | 0.75 | 0.67 | 0.58 | 0.5 | 0.42 | 0.33 | 0.25 | 0.17 | 0.08 |
| 12 | 0.56 | 0.5 | 0.45 | 0.39 | 0.34 | 0.28 | 0.22 | 0.17 | 0.11 | 0.06 |
| 13 | 0.95 | 0.85 | 0.76 | 0.66 | 0.57 | 0.47 | 0.38 | 0.28 | 0.19 | 0.09 |
| 14 | 1.73 | 1.55 | 1.38 | 1.21 | 1.04 | 0.86 | 0.69 | 0.52 | 0.35 | 0.17 |
| 15 | 0.98 | 0.89 | 0.79 | 0.69 | 0.59 | 0.49 | 0.39 | 0.3 | 0.2 | 0.1 |
| 16 | 1.11 | 1 | 0.89 | 0.78 | 0.67 | 0.55 | 0.44 | 0.33 | 0.22 | 0.11 |
| 17 | 1.76 | 1.59 | 1.41 | 1.23 | 1.06 | 0.88 | 0.71 | 0.53 | 0.35 | 0.18 |
| 18 | 1.02 | 0.92 | 0.82 | 0.72 | 0.61 | 0.51 | 0.41 | 0.31 | 0.2 | 0.1 |
| 19 | 0.61 | 0.55 | 0.49 | 0.43 | 0.37 | 0.31 | 0.24 | 0.18 | 0.12 | 0.06 |
| 20 | 1.17 | 1.06 | 0.94 | 0.82 | 0.7 | 0.59 | 0.47 | 0.35 | 0.23 | 0.12 |

Table 27 Fatigue cycle and life analysis of numbered welding joints

| Joints No. | Fatigue Cycles | | | | | | | | | | Fatigue life | |
|---|---|---|---|---|---|---|---|---|---|---|---|---|
| | 50°F | 45°F | 40°F | 35°F | 30°F | 25°F | 20°F | 15°F | 10°F | 5°F | Total Cycles | Years |
| 1 | 3.97E+03 | 5.62E+03 | 8.27E+03 | 1.28E+04 | 2.13E+04 | 3.88E+04 | 8.09E+04 | 2.08E+05 | 7.91E+05 | 7.73E+06 | 1.59E+04 | 44 |
| 2 | 4.95E+03 | 7.01E+03 | 1.03E+04 | 1.60E+04 | 2.66E+04 | 4.84E+04 | 1.01E+05 | 2.60E+05 | 9.87E+05 | 9.65E+06 | 1.99E+04 | 54 |
| 3 | 1.60E+05 | 2.26E+05 | 3.33E+05 | 5.17E+05 | 8.59E+05 | 1.56E+06 | 3.26E+06 | 8.40E+06 | 3.19E+07 | | 6.42E+05 | 1,759 |
| 4 | 1.09E+05 | 1.54E+05 | 2.26E+05 | 3.51E+05 | 5.83E+05 | 1.06E+06 | 2.21E+06 | 5.70E+06 | 2.16E+07 | | 4.36E+05 | 1,195 |
| 5 | 6.31E+06 | 8.92E+06 | 1.31E+07 | 2.04E+07 | 3.39E+07 | 6.17E+07 | 1.29E+08 | | | | 2.55E+07 | 69,780 |
| 6 | 2.94E+06 | 4.16E+06 | 6.13E+06 | 9.51E+06 | 1.58E+07 | 2.88E+07 | 5.99E+07 | 1.54E+08 | | | 1.18E+07 | 32,356 |
| 7 | 1.33E+07 | 1.89E+07 | 2.78E+07 | 4.31E+07 | 7.16E+07 | 1.30E+08 | | | | | 5.51E+07 | 151,024 |
| 8 | 2.12E+06 | 3.00E+06 | 4.42E+06 | 6.85E+06 | 1.14E+07 | 2.07E+07 | 4.32E+07 | 1.11E+08 | | | 8.51E+06 | 23,317 |
| 9 | 1.77E+06 | 2.50E+06 | 3.68E+06 | 5.72E+06 | 9.49E+06 | 1.73E+07 | 3.60E+07 | 9.28E+07 | | | 7.10E+06 | 19,450 |
| 10 | 8.76E+06 | 1.24E+07 | 1.82E+07 | 2.83E+07 | 4.70E+07 | 8.56E+07 | | | | | 3.62E+07 | 99,091 |
| 11 | 2.12E+07 | 3.00E+07 | 4.42E+07 | 6.85E+07 | 1.14E+08 | | | | | | 9.30E+07 | 254,825 |
| 12 | 7.86E+07 | 1.11E+08 | 1.64E+08 | | | | | | | | 6.68E+08 | 1,830,651 |
| 13 | 1.40E+07 | 1.98E+07 | 2.92E+07 | 4.52E+07 | 7.51E+07 | 1.37E+08 | | | | | 5.78E+07 | 158,340 |
| 14 | 1.94E+06 | 2.74E+06 | 4.04E+06 | 6.27E+06 | 1.04E+07 | 1.90E+07 | 3.95E+07 | 1.02E+08 | | | 7.79E+06 | 21,344 |
| 15 | 1.23E+07 | 1.75E+07 | 2.57E+07 | 3.99E+07 | 6.63E+07 | 1.21E+08 | | | | | 5.10E+07 | 139,731 |
| 16 | 8.33E+06 | 1.18E+07 | 1.74E+07 | 2.69E+07 | 4.47E+07 | 8.15E+07 | 1.70E+08 | | | | 3.36E+07 | 92,142 |
| 17 | 1.81E+06 | 2.56E+06 | 3.77E+06 | 5.85E+06 | 9.71E+06 | 1.77E+07 | 3.69E+07 | 9.50E+07 | | | 7.26E+06 | 19,900 |
| 18 | 1.08E+07 | 1.53E+07 | 2.26E+07 | 3.50E+07 | 5.82E+07 | 1.06E+08 | | | | | 4.48E+07 | 122,631 |
| 19 | 5.91E+07 | 8.36E+07 | 1.23E+08 | | | | | | | | 5.03E+08 | 1,377,073 |
| 20 | 6.89E+06 | 9.74E+06 | 1.44E+07 | 2.23E+07 | 3.70E+07 | 6.73E+07 | 1.40E+08 | | | | 2.78E+07 | 76,179 |

# 7. Conclusions and recommendations for future work

Large Dynamic Message Signs (DMS) have been increasingly used on freeways, expressways, and major arterials to better manage the traffic flow by providing accurate and timely information to car/truck drivers and motorists. Overhead truss support structures are typically employed to support those DMS cabinets allowing the DMS cabinets to provide wider display to further lanes. Two manufacturing processes are primarily utilized on truss structures - welding and bolting. Recently, cracks at welding toes were reported for the structures employed in some states. The present study tried to identify the main cause of the development of cracks over time.

In order to predict the behavior of a highway overhead truss structure, detailed understanding of the loads and the response of the structure are necessary. Wind and temperature are the main loads that affect the structures during their lifetimes. It is well known that a large temperature range may generate unexpected high (thermal) stresses on the structures, especially where stress concentration occurs due to geometric discontinuities. Several National Cooperative Highway Research Program (NCHRP) studies have been focused on fatigue failure of truss structures but few truss structures were tested to understand the thermal response. This is a main contribution of the present study.

The influences of wind loads due to the mean wind and due to the passage of a truck underneath the DMS cabinet and of cyclic (daily) temperature variation on the truss structure were examined in this study. Initially, it was thought that the frequent passage of the trucks underneath the DMS cabinet can induce relatively large unsteady cyclic loads that can produce fatigue. Both the short-term monitoring data and the CFD simulations showed that these forces induced by truck-induced gust are relatively small and that it is very unlikely this effect generates cracks at the welding toes of the truss supporting the DMS cabinet. The temperature induced strains measured at the trusses that were monitored far exceeded any strains resulting from wind. Moreover, a detailed CFD analysis of the airflow around the DMS and the truss allowed us to estimate the wind loads on the DMS cabinet and the wind load on the individual members of the truss under various relevant conditions (with and without a truck under the DMS cabinet, with and without a high speed wind, with or without the truss supporting the DMS cabinet, etc.).

Two other possible sources are the daily temperature variation and the unsteady component of the wind load at high wind conditions induced by the shedding of vortices in the wake of the DMS cabinet. In this study we concentrated on the first source. The American Association of State Highway and Transportation Officials (AASHTO) Specification defines the limit loads in dead load, wind load, ice load, and fatigue design for natural wind gust and truck-induced gust. Thermal influence is not discussed in the specification, either in limit load or fatigue design. Although the frequency of the thermal load is low, when temperature range is large the stress range would be significant to the structure, especially near welding areas where stress concentration may occur. Since stress amplitude and range are the primary parameters for brittle fracture and fatigue life

estimation, respectively, it is necessary to analyze the thermal effect in the truss structures as well.

Data collected as part of a long-term field monitoring of an overhead aluminum truss structure in Iowa was used to investigate the effect of temperature variation on the truss. Finite element models were developed to estimate the strain and stress magnitudes, which were then compared with the field monitoring data. Although the frequency of the thermal load is low, results showed that when temperature range is large the stress range would be significant to the structure, especially near welding areas where stress concentration may occur. Moreover stress amplitude and range are the primary parameters for brittle fracture and fatigue life estimation. Fatigue life of the support structures (around 44 years for the truss investigated as part of the long-term monitoring study) was estimated based on AASHTO specifications and on results obtained from FE modeling of the truss structure. The main conclusion of the study is that thermal induced fatigue damage of the truss structures supporting DMS cabinets is the main cause for the cracks observed to develop at such structures.

Another probable cause for fatigue damage not investigated in this study are the cyclic oscillations of the total wind load associated with the vortex shedding behind the DMS cabinet at high wind conditions. These oscillations develop even under steady wind conditions. A resonance condition, causing large amplitude relatively steady vibrations of the support trusses can occur if the frequency of shedding coincides with a natural vibration frequency of the DMS cabinet. We think further investigations of these two effects are needed to fully comprehend the main reasons why cracks develop over time in trusses supporting DMS cabinets. Although inconclusive here, it is believed that fabrication may play an important role in the development of fatigue cracks. However, given the variety of different fabrication styles and potential fabrication errors, there are likely multiple causes for the development of cracks.

## References


Alberta Infrastructure and Transportation. 2006. *Highway Guide and Information Sign Manual*, Edmonton Alabama.

American Association of State Highway and Transportation Officials. 2004. *AASHTO LFDR Bridge Design Specifications*. Washington, DC.

American Association of State Highway and Transportation Officials. 2010. *Standard Specifications for Structural Supports for Highway Signs, Luminaires and Traffic Signals, 5th Ed*. Washington, DC.

ANSYS User's manual, Volumes I, II, and III, Version 10, Swanson Analysis Systems, Inc., Houston, PA, 2005.

ANSYS Inc 2007. *Help System, Element Type Guide,* ANSYS, Inc.

ANSYS Inc. 2012. Retrieved July 2012, from *http://www.ansys.com/Products/Workflow+Technology/ANSYS+Workbench+Platform/Features*

ANSYS theory manual, Version 10, Swanson Analysis Systems, Inc., Houston, PA, 2005

Bannantine, J.A., Comer, J.J., Handrock, J.L. 1990. *Fundamentals of Metal Fatigue Analysis*. New Jersey: Prentice Hall.

Beer, F.P., Johnston, E.R., DeWolf, J.T., Mazurek, D.F. 2009. *Mechanics of Materials, 5th Ed*. New York: McGraw Hill Higher Education.

Bhatti, M.A. Advanced Topics in Finite Element Analysis of Structures: with Mathematica and MATLAB Computations, John Wiley, New York 2006

Bhatti, M.A. Fundamental Finite Element Analysis and Applications: with Mathematica and MATLAB Computations, John Wiley, New York. 2005

Bowen Laboratory. 2011. *Load Testing and Evaluation of Aluminum Sign Trusses in the State of Iowa - Final Report*, West Lafayette, Indiana: Purdue University.

Brakke B. 2007. *Action Plan for DMS Trusses*. : Iowa DOT.

Chang, B., Phares, B. M., Sarkar, P. P., and Wipf, T. J. 2009. Development of a Procedure for Fatigue Design of Slender Support Structures Subjected to Wind-induced Vibration. *Transportation Research Record: Journal of the Transportation Research Board*, No. 2131, TRB, National Research Council, Washington, D.C., pp. 23-33

Chang, B., Sarkar, P. P., and Phares, B. M. 2010. Time-Domain Model for Predicting Aerodynamic Loads on a Slender Support Structure for Fatigue Design. *The ASCE Journal of Engineering Mechanics*, Vol. 136, No. 6, pp. 736-746

Clark, R. and Dowell, E. H. 2004. *A Modern Course in Aeroelasticity*, Norwell, Massachusetts: Kluwer Academic Publishers.

Constantinescu, S.G., Bhatti, M.A., and Tokyay, T. (2007), "Improved method for determining wind loads on highway sign and traffic signal structures" Final Report TR-559, Iowa Highway Research Board, Iowa DOT, IA

Dexter, J.R. and Ricker, J.M. 2002. *NCHRP Report 469 – Fatigue-Resistant Design of Cantilevered Signal, Sign, and Light Supports*. Washington, D.C.: Transportation Research Board.

Fouad, H.F.; Davidson, S.J.; Delatte, N.; Calvert, E.; Chen, S.; Nunez, E. and Abdalla, R. 2003. *NCHRP Report 494 – Structural Supports for Highway Signs, Luminaries, and Traffic Signals*. Washington, D.C.: Transportation Research Board.

Geokon Inc. 2009. *Instruction Manual Model VK-4100/4150 – Vibrating Wire Strain Gages*. Lebanon, New Hampshire: Geokon Inc.

Guire, R.M 2006. *Introduction to Materials Science & Engineering*. Evanston, Illinois: Northwestern University Press.

Huckelbridge, A. and Metzger, A. 2007. *Investigation of the Dayton IR 75 Sign Truss Failure of 9/11/06*, Cleveland, Ohio: Case Western Reserve University Department of Civil Engineering.

Kacin, J., Rizzo, P., and Tajari, M. 2010. *Fatigue analysis of overhead sign support structure*, Engineering Structures 32, pp.1659-1670.

Lee, H.H. 2011. *Finite Element Simulations with ANSYS Workbench 13*. Mission Kansas: Schroff Development Corporation.

Mclean, T.W., Park, J.S., Stallings, J.M. 2004. *Fatigue Evaluation of Two Variable Message Sign Structures*. Montgomery, Alabama: The Alabama Department of Transportation.

National Renewable Energy Laboratory. 2012. *http://www.nrel.gov/gis/cfm/data/GIS_Data_Technology_Specific/United_States/Wind/High_Resolution/Iowa_50m_wind.zip*

Schoenborn, K.D. 2006. *Fatigue Analysis of a Welding Assembly Using ANSYS Workbench Environment*. Germany: ANSYS Service @ CADFEM GmbH.

Stam, A., Richman, N., Pool, C., Rios, C., Anderson, T., and Frank, K. 2011. *Fatigue Life of Steel Base Plate to Pole Connections for Traffic Structures*, Report No.: FHWA/TX-11/9-1526-1. University of Texas at Austin: Austin, Texas

Stephens, R.I.; Fuchs, H.O. 2001. Metal Fatigue in Engineering (Second edition ed.). John Wiley & Sons, Inc.. p. 69.

WeatherUnderground 2012. Retrieved July 2012, from http://www.wunderground.com/history/airport/KAMW/2002/1/1/CustomHistory.html?dayend=31&monthend=12&yearend=2011&req_city=NA&req_state=NA&req_statename=N